

Contents

I Particle Physics	1
1 Tests of Lepton-Flavor Conservation at PSI	2
1.1 $\mu \rightarrow e$ conversion in muonic atoms: the SINDRUM II project (PSI proposal R-87-03)	2
1.1.1 Search for $\mu \rightarrow e$ conversion on gold (1997 data)	3
1.1.2 Search for $\mu \rightarrow e$ conversion on lead (1998 data)	4
2 Rare kaon decays	6
3 Meson Spectroscopy at LEAR with the Crystal Barrel	10
3.1 Annihilation in flight into three neutral pseudoscalars	10
3.2 Annihilation at rest into $\pi^0\pi^0\omega$ and $\pi^0\eta\omega$	12
4 Particle Physics at LHC/CMS	15
4.1 Pixel Detector	15
4.1.1 Silicon Microstrip Telescope	15
4.1.2 Pixels	15
5 Production and Spectroscopy of Antihydrogen	20
5.1 Silicon microstrip detector	21
5.2 Test of CsI crystals	22
6 Measurement of the Neutrino Magnetic Moment at the Bugey Nuclear Reactor	24
7 Particle Physics at DESY/HERA	28
7.1 Electron proton collisions at 300 GeV center of mass energy	28
7.2 Summary of activities	29
7.3 Results from recent analyses	30
7.3.1 High momentum transfer data	30
7.3.2 Heavy quark production	32
7.4 Microstrip gas chambers	37
7.4.1 The GEM-MSGC detector for HERA-B	37
7.4.2 Substrate production and quality control at IMT	38
7.4.3 MSGC tests at PSI	39
7.4.4 Status of the HERA-B experiment	40
8 Neutrino Masses and Mixing	45
8.1 Calibration	45
8.2 Results for ^{63}Ni	46
8.3 Results for ^{35}S	46
8.4 Conclusion	47
9 Measurement of the gravitational constant G	48
9.1 The principle of the experiment	48
9.2 Measurements with mercury	48
9.3 Improvements of the experiment	49

II Condensed Matter Physics	52
10 NMR/NQR Spectroscopy	53
10.1 Colloquium on <i>MAGNETIC RESONANCE IN HIGH-T_c SUPERCONDUCTORS</i>	53
10.2 High-temperature superconductors	53
10.2.1 Isotope effect of the spin gap	53
10.2.2 Spin and charge dynamics in the Cu–O chains of $\text{YBa}_2\text{Cu}_4\text{O}_8$	54
10.2.3 Magnetic properties of Cu–O chains in $\text{YBa}_2\text{Cu}_3\text{O}_7$ and $\text{YBa}_2\text{Cu}_4\text{O}_8$	54
10.2.4 Interplane electronic spin polarization transfer in the superconducting state of $\text{Y}_2\text{Ba}_4\text{Cu}_7\text{O}_{15}$	55
10.2.5 Cluster formation of chain oxygen vacancies in $\text{YBa}_2\text{Cu}_3\text{O}_{7-\delta}$ as the origin of the fishtail anomaly	57
10.3 Antiferromagnetic parent compounds	58
10.3.1 Sublattice magnetization in the antiferromagnetic parent compounds	58
10.3.2 The paramagnetic phase of $\text{YBa}_2\text{Cu}_3\text{O}_6$	60
10.4 Superionic glasses	61
10.4.1 Relaxation of the stationary phosphorus nucleus	61
10.4.2 Magic angle spinning	61
10.4.3 ^{31}P – ^{19}F spin–echo double resonance (SEDOR)	62
10.5 High–pressure NMR in $\text{Ca}_{0.85}\text{Sr}_{0.15}\text{CuO}_2$	63
11 Magnetic Properties of Superconductors	66
11.1 Introduction	66
11.2 Investigating vortex matter at central facilities	67
11.3 Penetration depth measurements in $\text{YBa}_2\text{Cu}_4\text{O}_8$ family superconductors	70
11.4 Investigating vortex matter by torque magnetometry	71
11.4.1 Enhancement of the vortex-lattice relaxation by means of an external ac magnetic field	71
11.4.2 First-order vortex-lattice melting transition in $\text{YBa}_2\text{Cu}_3\text{O}_{7-\delta}$ near the critical temperature detected by magnetic torque	73
11.5 Detection of small thermal effects in basic and applied condensed matter physics	73
11.6 Studies of oxygen isotope effects	75
11.6.1 Oxygen isotope effects in the manganites	75
11.6.2 Oxygen isotope effects in $\text{La}_{2-x}\text{Sr}_x\text{CuO}_4$	77
11.6.3 EPR study of oxygen isotope effect in $\text{La}_{2-x}\text{Sr}_x\text{CuO}_4$	77
12 Surface Physics	80
12.1 X-ray photoelectron diffraction in the backscattering geometry	81
12.2 Hexagonal boron nitride films on Ni(111)	81
12.3 Time-resolved medium-energy electron diffraction	83
12.4 Near-node photoelectron holography	84
12.5 Photoemission from oriented orbitals	86
12.6 Photoemission Fermi edge as a thermometer	87
12.7 Underdoping of Bi-cuprates by ultraviolet radiation	87
12.8 Evolution of the Fermi surface in a transition metal film	88
12.9 Surface states on vicinal Cu(111) surfaces	89
12.10 Velocity-selective optical pumping due to back reflection of resonant laser light in a thin sodium vapor cell	91

13 Spontaneous Ordering in AlGaAs	94
14 Computer Assisted Physics	96
14.1 Computational Physics	96
14.2 Electronic structure calculations of high-temperature superconductors	96
14.3 Quantum Monte-Carlo simulations of the antiferromagnetic Heisenberg model	98
14.4 Electroencephalograms in epilepsy: analysis and seizure prediction within the framework of Lyapunov theory	99
14.5 Nonlinear wave phenomena in porous media	101
15 Electronic	103
15.1 Current Detection Amplifiers for Plasma Traps	103
16 Publications	104
16.1 Research group of Prof. C. Amsler	104
16.2 Research group of Prof. Brinkmann	105
16.3 Research group of Prof. R. Engfer	109
16.4 Research group of Prof. H. Keller	110
16.5 Research group of Prof. W. Kündig	116
16.6 Research group of Prof. P. F. Meier	117
16.7 Research group of Prof. J. Osterwalder	119
16.8 Research group of Prof. P. Truöl	122

Part I

Particle Physics

The various groups of the *Physik-Institut* in the fields of particle physics are using for their experiments external accelerators at the large international research institutions PSI (Villingen), CERN (Genf), DESY (Hamburg) and Brookhaven. Further activities in the field of particle physics which are connected to questions of astroparticle physics and cosmology do not require accelerators or they are carried out at a nuclear reactor.

Most of these experiments are motivated in a broader sense by the fact that the present, highly successful standard model of particle physics cannot be understood as the ultimate truth for several, often cited reasons: There are too many free parameters, the origin of the masses and the nature of the neutrinos is not known, no symmetry is known which leads to the conservation of the lepton number separately for the three generations, the strong force is not yet unified with the electroweak force, the quantization of the gravitational force is unsolved, the question of the existence of other forces is still open.

A test of the standard model can be done by either a search for new particles or states of matter at medium and high energies, or complementary by a search with high precision at low energies for forbidden lepton number violating processes, a search for the magnetic moment of the neutrino at a reactor power station or by the spectroscopy of Antimatter in the Antihydrogen-Atom.

Mainly on the basis of this motivation Part I of the annual report presents the following experiments:

- Tests of lepton-flavor conservation at PSI
- Rare kaon decays
- Meson spectroscopy at LEAR with the Crystal Barrel
- Particle physics at LHC/CMS
- Production and Spectroscopy of Antihydrogen
- Measurement of the Neutrino Magnetic Moment at the Bugey Nuclear Reactor
- Particle physics at DESY/HERA
- Neutrino masses and mixing
- Measurement of the gravitational constant G

1 Tests of Lepton-Flavor Conservation at PSI

R. Engfer, E.A. Hermes, T. Kozlowski, G. Kurz,
F. Riepenhausen, A. van der Schaaf and P. Wintz

in collaboration with III. Phys. Institut der RWTH Aachen and PSI Villigen.

Various anomalies in the fluxes of solar [1], atmospheric [2] and beam dump neutrinos [3] give strong evidence that neutrino states mix, which is incompatible with the neutrino mass degeneracy assumed in the Standard Model. Consequently, charged-current weak interactions do not conserve generation number, neither in the quark nor in the lepton sector.

Many extensions of the Standard Model allow also neutral interactions between the generations. Flavor-changing neutral currents (FCNC) among leptons would yield an unambiguous signal for new physics. See [4, 5, 6] for some reviews. Theoretical study of physics beyond the Standard Model presently concentrates on supersymmetry and grand-unification. Supersymmetric models which do not conserve R-parity, i.e. those allowing transitions between the known particles and their super-partners, automatically lead to processes that do not conserve lepton and/or baryon number. Stringent constraints on various products of R-parity violating couplings have been derived from the observed upper limits on $\mu^- \rightarrow e^-$ conversion [7]. As discussed first by Hall, Kostelecky and Raby [8] flavor-violation may be introduced in grand-unified theories by loop corrections above the unification scale. Later it was realized that the flavor-violation observed in the large top-Yukawa coupling leads to measurable rates for LFC-violating processes [9], in particular for the decay $\mu \rightarrow e\gamma$, even in standard SUSY SU(5).

1.1 $\mu \rightarrow e$ conversion in muonic atoms: the SINDRUM II project (PSI proposal R-87-03)

With some three years delay, the PMC magnet reached its design field of 1.5 T early in August 1998. The PMC magnet is a 8.5 m long super-conducting solenoid which couples the new $\pi E5$ beamline to the SINDRUM II spectrometer. Ever since then stable operation at a field strength around 1.1 T could be maintained. As a result we are in the position now to increase the beam intensity by one order of magnitude and push the sensitivity for conversion on titanium into the region of a few times 10^{-14} , i.e. the goal set in the proposal. This breakthrough was achieved by improving the geometry at the far end of the PMC, where it enters the SINDRUM II spectrometer, and by lowering the temperature of the radiation shields from 70 K to 10 K. The price which had to be paid was a separation of the two magnets by 20 cm and some modifications in the SINDRUM II mirror plate and photomultiplier lightguides which took place in the beginning of 1999.

Towards the end of 1998 extensive beam studies have been performed and during three weeks data were taken on lead. The main problem that we were faced with was the heavy load of beam electrons on the spectrometer. The $\pi E5$ beam line transports about $3 \times 10^9 \text{ s}^{-1}$ electrons, independent of the selected beam momentum. At momenta above $\approx 70 \text{ MeV}/c$ these electrons would completely saturate the SINDRUM detector systems. Fortunately, by moderating the beam at the $\pi E5$ exit and by proper selection of the resulting muon momentum in the PMC entrance collimator a significant reduction of the electron contamination can be achieved.

In 1999, after some further beam optimisation, we intend to finish the lead measurements before switching to a titanium target. It is our aim to reach a single-event sensitivity around 2×10^{-14} for titanium.

1.1.1 Search for $\mu \rightarrow e$ conversion on gold (1997 data)

In 1997 the PMC field could not yet be raised above 0.3 T and thus only a relatively low beam momentum could be selected. Data were taken on a heavy target, using a 26 MeV/c cloud-muon beam. Thanks to the low beam momentum resulting in a narrow range distribution a target with a total weight of only 18 g could be used. For reasons of mechanical stability we choose gold rather than lead. The low-momentum beam offers a number of advantages, to be balanced against the relatively low stop rate of $6 \times 10^5 \text{ s}^{-1}$: negligible backgrounds induced by pions, muon decay in flight and scattered beam electrons and, as a result of the low target mass, a superb 0.7 MeV/c momentum resolution at the conversion energy.

Figure 1.1 shows preliminary results of the data analysis. The measured momentum distribution is nicely reproduced, both in shape and in number of events, by a simulation of muon decay in orbit. No events are seen in the signal region for μe conversion. At present we are still evaluating the sensitivity obtained, but the resulting upper limit will certainly improve on the best previous result on a heavy target [10].

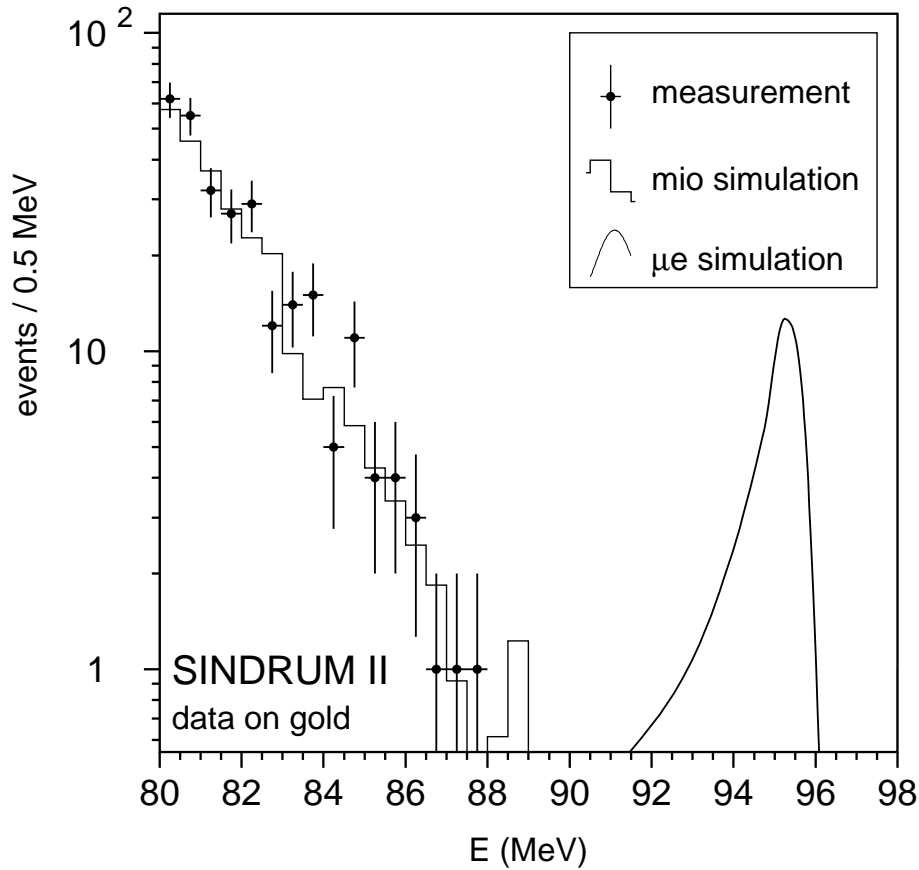


Figure 1.1: Endpoint region of the energy distribution of electrons emitted from muonic gold atoms. The measured distribution can be attributed completely to muon decay in orbit (mio). The precise normalisation is still under study.

1.1.2 Search for $\mu \rightarrow e$ conversion on lead (1998 data)

The new beamline allowed us to reach our former sensitivity for conversion on lead in less than a day so a dramatic improvement in sensitivity is anticipated. Most sources of background are enhanced compared to the case of titanium and can thus be studied more efficiently. In particular the decay-in-flight background is much more serious since the conversion energy is lowered by the binding energy of about 10 MeV.

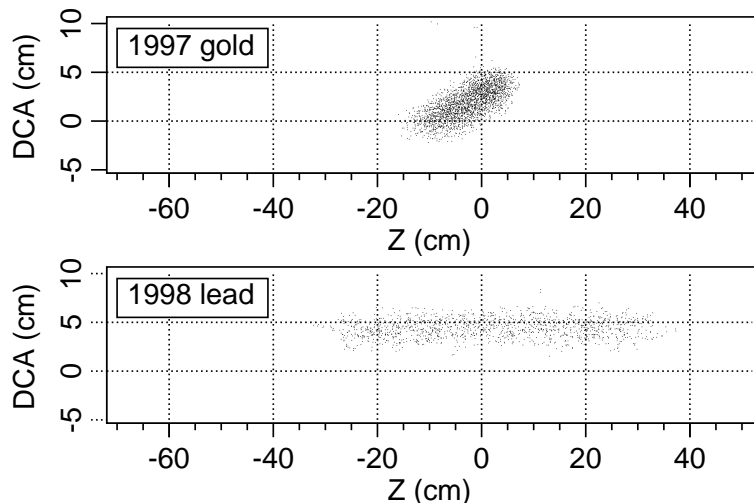


Figure 1.2: Spatial distribution of the point of closest approach to the spectrometer axis of the reconstructed trajectories for the two measuring periods. Clearly visible are the conical and tube shapes of the two targets.

Since the beam particles passing the narrow collimator at the PMC entrance periodically return to the beam axis a long narrow tube was used as a target (see Fig 1.2), resulting in a well-defined threshold on the transverse momentum selected by the spectrometer. For the first time a second-level readout trigger was installed which uses the late drift-chamber signals. At present the reduction compared to level 1 is a factor 20. Thanks to the improved trigger selectivity (the fraction of fully reconstructed muon-induced events in the on-line data-analysis increased to more than 10% of the recorded events) the readout deadtime could be kept below 15%. These data are still being analyzed as well. We should know soon whether in particular the pion background is under control which may affect the beam settings for the major six months beam period scheduled for 1999.

Spatial distribution of the point of closest approach to the spectrometer axis of the re-

constructed trajectories for the two measuring periods. Clearly visible are the conical and tube shapes of the two targets.

References

- [1] K. Nakamura, in: C. Caso *et al.* (Particle Data Group), *Eur. Phys. J. C* **3**, 1 (1998), p. 327.
- [2] Super-Kamiokande, Y. Fukuda *et al.*, *Phys. Rev. Lett.* **81**, 1562 (1998).
- [3] LSND Collaboration, C. Athanassopoulos *et al.*, *Phys. Rev. Lett.* **81**, 1774 (1998).
- [4] J.D. Vergados, *Phys. Rep.* **133**, 1 (1986).
- [5] A. van der Schaaf, in *Progress in Particle and Nuclear Physics*, edited by A. Faessler (Pergamon, Oxford, 1993), Vol. 31, p. 1.
- [6] P. Depommier and C. Leroy, *Rep. Prog. Phys.* **58**, 61 (1995).
- [7] K. Huitu, J. Maalampi, M. Raidal, and A. Santamaria, *Phys. Lett. B* **430** 355 (1998).
- [8] L.J. Hall, V.A. Kostelecky and S. Raby, *Nucl. Phys.* **B267** 415 (1986).
- [9] R. Barbieri and L.J. Hall, *Phys. Lett. B* **338** 212 (1994); R. Barbieri, L.J. Hall and A. Strumia, *Nucl. Phys.* **B445** 219 (1995).
- [10] SINDRUM II Collaboration, W.Honecker *et al.*, *Phys. Rev. Lett.* **76**, 200 (1996).

2 Rare kaon decays

S. Pislak (until July 1997), P. Robmann and P. Truöl,
in collaboration with

J. Egger, W. D. Herold, H. Kaspar, and H. Weyer,
Paul-Scherrer-Institut, CH-5234 Villigen

Brookhaven National Laboratory, Upton, NY-11973, USA

University of New Mexico, Albuquerque, NM-87131, USA

University of Pittsburgh, Pittsburgh, PA-15260, USA

Yale University, Newhaven, CT-06511, USA

Institute for Nuclear Research, Academy of Sciences, 117 312 Moscow, Russia

Experiment E-865 at Brookhaven AGS

During our last 28 week long data taking run, which ended on the last day of 1998, we reached the primary goal of experiment E865. This experiment at the Brookhaven AGS was designed to reach a sensitivity limit for the lepton flavor non-conserving (LFNC) decay $K^+ \rightarrow \pi^+ \mu^+ e^-$ below a branching ratio level of 10^{-11} . Lepton flavor conservation is incorporated in the standard model of electroweak interaction, is experimentally well proven, but has no theoretical foundation within this model. The LFNC-decay mode searches are therefore driven by the curiosity to find out where the conservation ends, and by the hope, that there, where it ends, signals for non-standard model physics may appear.

Compared to the two prior data taking runs of 1995, which has been completely analysed, lead to two theses [1, 2] and a limit of 2×10^{-10} (95 % confidence), and of 1996, for which the analysis is nearly completed (4×10^{-11} expected [3]), a further factor of six in improvement seems possible. This estimate assumes, that no hitherto unknown sources of background are discovered during the analysis, which has only recently been started.

The 1998 run primarily benefitted from a longer accelerator spill (2.5 s instead of 1.2 s) and a microbunched beam (approximately 200 ps wide pulses appearing at 93 MHz repetition rate) which showed less spikes. This was important, because it reduced the trigger rate, which was dominated by accidental coincidences. We also implemented additional faster processors and buffers, which allowed us to accept 1600 events per spill with deadtimes around 10 % compared to previously only 600 events. Improved mirrors for the Čerenkov counters lead to higher efficiency and finally the on-line filter code was tailored further.

We will concentrate in this report on a result [4], which we are going to publish shortly, and which concerns the decay $K^+ \rightarrow \pi^+ e^+ e^-$. This rare decay (branching ratio $\sim 2.7 \times 10^{-7}$) involves a flavor changing neutral current (FCNC). Its rate was first calculated assuming the decay to occur through a short distance $s \rightarrow d\gamma$ transition [5]. Since then, however, it has been realized that the decay mechanism is dominated by long-distance effects. In chiral perturbation theory (CHPT), which successfully modeled many decay modes of the light mesons, predictions for the decay rate and invariant electron-positron mass (M_{ee}) distribution exist. Previous measurements [6, 7] were only marginally consistent with next to leading order predictions of this theory [8]. Our new measurements with significantly improved statistics and greater acceptance over the M_{ee} range, which were first reported at the Vancouver conference [9], require higher order contributions [10, 11]. Our data on $K^+ \rightarrow \pi^+ \mu^- \mu^+$, referred to last year explore the same physics. Assuming the dominance of one-photon exchange process, the difference between the two decays lies only in the available phase space.

The primary trigger for this data required three charged particles defined by signals in the hodoscopes before the analysing magnet and in front of the electromagnetic calorimeter, and the calorimeter itself. This trigger rate is dominated by accidentals, and $K^+ \rightarrow \pi^+ \pi^+ \pi^-$ decays. For $K^+ \rightarrow \pi^+ e^+ e^-$ decays, Čerenkov signals were required on each side of

the detector in addition. This trigger was then dominated by events originating from the decay chain $K^+ \rightarrow \pi^+\pi^0$; $\pi^0 \rightarrow e^+e^-\gamma$ (K_{π^2Dal}), where the typical e^+e^- invariant mass was low. Taking advantage of the fact that the low mass e^+e^- pair were not separated vertically in the non-bending plane, a “high mass” trigger was configured by requiring a vertical separation of calorimeter hits associated with the Čerenkov counter response.

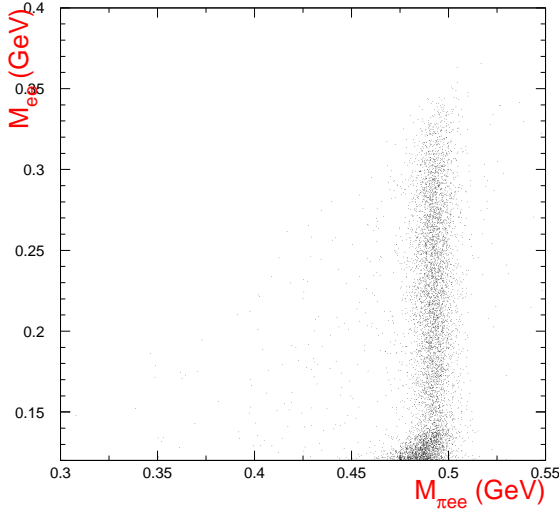


Figure 2.1: e^+e^- invariant mass versus $\pi^+e^+e^-$ invariant mass for $K^+ \rightarrow \pi^+e^+e^-$ candidates.

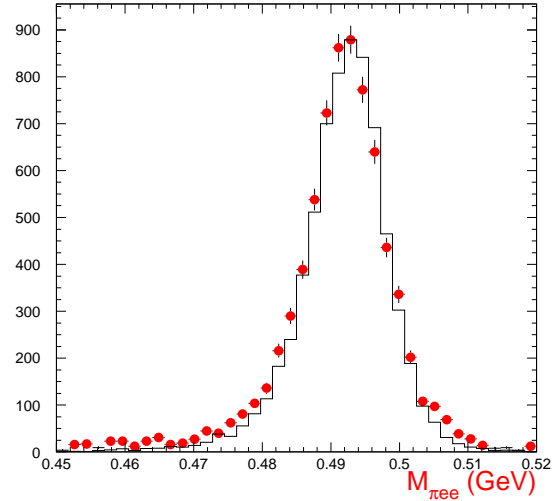


Figure 2.2: $\pi^+e^+e^-$ invariant mass for $K^+ \rightarrow \pi^+e^+e^-$ candidates with $M_{ee} > 150$ MeV (histogram: Monte Carlo simulation).

The $K^+ \rightarrow \pi^+e^+e^-$ data were taken in 1995 and 1996, running typically at 7×10^{12} protons/pulse for about 25 weeks. Events were selected which contained unambiguous identification of a positive pion, and the lepton pair, whose trajectories were consistent with having come from a common vertex located within the 5 m long evacuated decay volume. The reconstructed kaon was required to have come from the target upstream of the beam magnets.

Figure 2.1 displays the M_{ee} versus the invariant mass of the three final state particles, $M_{\pi ee}$, for the $K^+ \rightarrow \pi^+e^+e^-$ candidates. The cluster of events below 130 MeV are the background from K_{π^2Dal} , where the $M_{\pi ee}$ is just below M_K because of a missing soft photon. Figure 2.2 shows $M_{\pi ee}$ for events with $M_{ee} > 0.15$ GeV. About 10,000 events are selected after all the cuts. The background is insignificant.

Assuming a pure vector interaction the decay distribution for $\pi^+e^+e^-$ can be described by

$$\frac{d\Gamma(q^2, \cos\theta)}{dq^2 d\cos\theta} = \frac{G^2 \alpha^2 M_K^3}{16\pi} \rho^{3/2}\left(1, \frac{q^2}{M_K^2}, \frac{m_\pi^2}{M_K^2}\right) \left(1 - \frac{4m_e^2}{q^2}\right)^{1/2} \left[1 - \left(1 - \frac{2m_e^2}{q^2}\right) \cos^2\theta\right] |f(q^2)|^2,$$

where $\rho(a, b, c) = a^2 + b^2 + c^2 - 2(ab + bc + ac)$, G is a constant and θ the angle between the positron and pion momentum vectors in the e^+e^- center of mass frame. The form factor $f(q^2)$ is a dimensionless function of $q^2 = M_{ee}^2$. The data shown in Figure 2.3 are consistent with this assumption.

The branching ratio and the decay spectrum for the K_{π^2Dal} decay are known. We normalize our $K^+ \rightarrow \pi^+e^+e^-$ data to this decay, which has the advantage, that almost all efficiency factors cancel (e. g. those for the Čerenkov counters). The relative acceptances and their

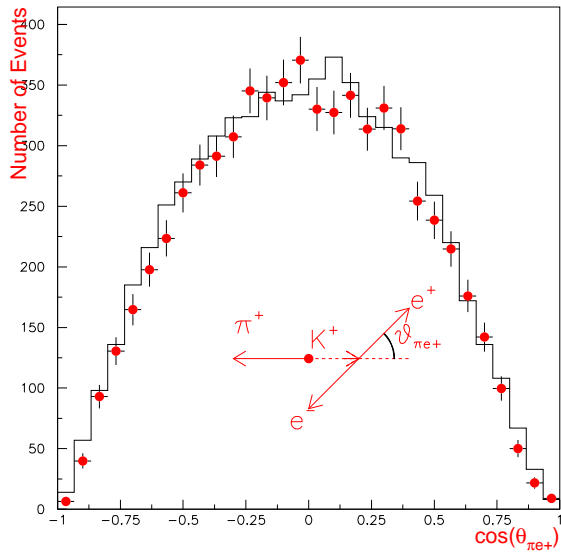


Figure 2.3: Angular distribution ($\cos\theta$) of $K^+ \rightarrow \pi^+ e^+ e^-$ events in comparison with Monte Carlo simulation with pure vector interaction.

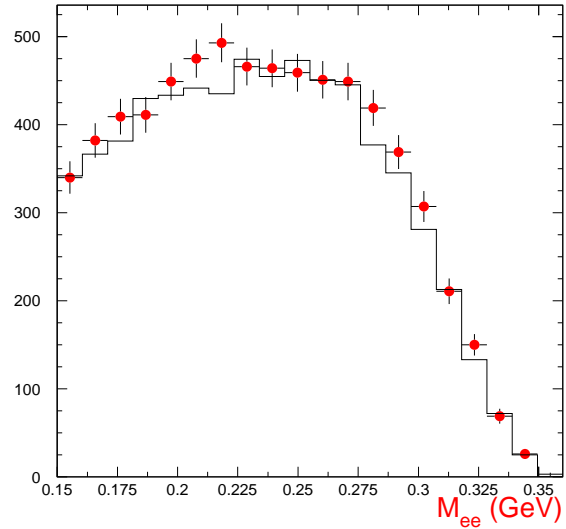


Figure 2.4: Invariant mass (M_{ee}) distribution for accepted $K^+ \rightarrow \pi^+ e^+ e^-$ events in comparison with Monte Carlo simulation with $\lambda = 0.2$.

mass and angular dependence are taken from a Monte Carlo simulation, which represents the data well, as e. g. demonstrated in Figure 2.2.

The form factor $f(q^2)$ can be determined by fitting the normalized M_{ee} spectrum. Several parametrisations are possible. Vector meson dominance suggests a parametrisation analogous to the semi-leptonic decay $K^+ \rightarrow \pi^0 e^+ \nu_e$

$$f(q^2) = f_+ \left(1 + \lambda \frac{q^2}{M_\pi^2} \right),$$

while chiral perturbation theory (CHPT) [8] leads to

$$f(q^2) = -(\phi_K(q^2) + \phi_\pi(q^2) + w_+).$$

ϕ_K and ϕ_π are analytic functions of q^2 , and w_+ is a parameter to be determined from the data. The results are summarized in Table 2.1.

Ansatz	Parameters	Branching ratio	χ^2/n_{df}
Model independent	$\lambda = 0.175 \pm 0.010$	$(2.68 \pm 0.03) \cdot 10^{-7}$	29/19
CHPT $\mathcal{O}(p^4)$ [8]	$w_+ = 0.574 \pm 0.011$	$(2.83 \pm 0.03) \cdot 10^{-7}$	16/19
CHPT [11]	$a_+ = 0.56 \pm 0.01, b_+ = 0.65 \pm 0.04$	$(2.77 \pm 0.03) \cdot 10^{-7}$	17/19

Table 2.1: Parameters extracted from the form factor fits to the ee mass spectrum (preliminary values and statistical errors only [4]).

CHPT up to $\mathcal{O}(p^4)$ also predicts a correlation between the branching ratio and the value of w_+ , which is shown in Figure 2.5. Though the M_{ee} spectrum is fit very well, the corresponding branching ratio does not match the predicted curve. The previous data [6, 7] already indicated a similar trend. We therefore conclude that CHPT of $\mathcal{O}(p^4)$ is insufficient to describe the $K^+ \rightarrow \pi^+ e^+ e^-$ data.

While in CHPT up to order $\mathcal{O}(p^4)$ almost all the mass dependence is given by a pion loop term [8], later refinements [10, 11] point to additional terms. These are cast somewhat arbitrarily e. g. in the form $a_+ + b_+ M_{ee}^2/M_K^2$ [11]. The corresponding fit shows a good χ^2 and remedies the problem with the branching ratio, but certainly does not lead to a deeper understanding of the details of the decay mechanism yet.

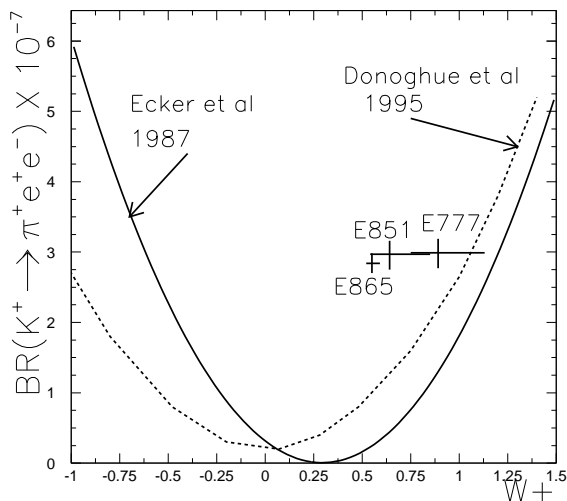


Figure 2.5: Comparison of the experimental data on the branching ratio and w_+ to theoretical predictions: solid curve [8], dashed curve [10]; previous measurements [6, 7].

References

- [1] *Experiment E865 at BNL: a search for the decay $K^+ \rightarrow \pi^+\mu^+e^-$* , S. Pislak, Thesis, University of Zürich (1997).
- [2] *A search for the decay $K^+ \rightarrow \pi^+\mu^+e^-$* , D. Bergman, Thesis, Yale University, New Haven (1997).
- [3] H. Do, Thesis, Yale University, New Haven, in preparation.
- [4] *A high-precision study of the rare decay of a charged kaon into a charged pion and an electron-positron pair*, S. Eilerts, University of New Mexico, Albuquerque (1998).
- [5] M. K. Gaillard, and B. W. Lee, Phys. Rev. **D10** (1974), 897.
- [6] C. J. Alliegro et al., Phys. Rev. Lett. **68** (1991), 278.
- [7] *A study of the decay $K^+ \rightarrow \pi^+e^+e^-$ and a measurement of the decay $\pi^0 \rightarrow e^+e^-$* , A. L. Deshpande, Thesis, Yale University, New Haven (1995).
- [8] G. Ecker, A. Pich and E. de Rafael, Nucl. Phys. **B291** (1987), 692.
- [9] *Study of $K^+ \rightarrow \pi^+e^+e^-$ and $K^+ \rightarrow \pi^+\mu^+\mu^-$ decays in E865 at the AGS*, H. Ma et al., Proc. Int. Conf. on High Energy Physics 98, Vancouver (July 1998).
- [10] J. Donoghue, and F. Gabbiani, Phys. Rev **D51** (1995), 2187.
- [11] G. D. Ambrosio et al., JHEP **8** (1998), 4.

3 Meson Spectroscopy at LEAR with the Crystal Barrel

C. Amsler, P. Giarritta, M. Heinzemann, F. Ould-Saada, C. Regenfus and S. Spanier

In collaboration with: Academy of Science (Budapest); Universities of Bochum, Bonn, Hamburg, Karlsruhe, Mainz, München, Paris VI; CERN; Carnegie Mellon University (Pittsburgh); CRN (Strasbourg); QMWC (London); RAL; UC (Berkeley).

The Crystal Barrel experiment started data taking in late 1989 and was completed in autumn 1996 with the closure of LEAR. In 1998/99 we continued the data analysis. Details on the results achieved in the previous years can be found in a recent review [1].

Last year we reported the discovery of a meson $\hat{\rho}(1405)$ decaying to $\eta\pi$ with quantum numbers $J^{PC} = 1^{-+}$. This state was observed in the $\eta\pi$ P-wave in $\bar{p}n$ annihilation into $\pi^-\pi^0\eta$, using a liquid deuterium target [2]. Quantum number conservation implies that a meson with such quantum numbers does not couple to $q\bar{q}$ and is therefore exotic, e.g. made of two quarks and two antiquarks, or of $q\bar{q}$ pair with an excited gluon. Supportive evidence for this state has now been obtained from $\bar{p}p$ annihilations into $\pi^0\pi^0\eta$, using hydrogen gas at 12 atm [3]. Its mass (1360 ± 25 MeV) and width (220 ± 90 MeV) are compatible with our previous findings [2]. The properties of the E/ι meson decaying to $\eta\pi\pi$ that we studied earlier in the annihilation channel $\pi^+\pi^-\pi^0\pi^0\eta$ [4] were confirmed by analyzing the channel $2\pi^+2\pi^-\eta$ [5]. There is now evidence that the E/ι region contains two overlapping pseudoscalar mesons, one around 1410 MeV, decaying to $\eta\pi\pi$ and $K\bar{K}\pi$ via the intermediate state $a_0(980)\pi$, and one around 1470 MeV, decaying to $K^*\bar{K}$ [6]. The latter is probably the $s\bar{s}$ member of the radially excited pseudoscalar nonet while the former could be exotic. We will report in more details below on the annihilation channels $\pi^0\pi^0\omega$ and $\pi^0\eta\omega$ at rest analyzed by the Zürich group.

This year most of the analysis efforts concentrated on the large samples collected with antiprotons in flight at various antiproton momenta between 600 and 1940 MeV/c. In particular we have searched for the $f_2(2220)$, a 2^{++} glueball candidate reported in radiative J/ψ decay [6], by varying the beam momenta in small steps and looking for a peak in the cross section for $\bar{p}p \rightarrow \eta\eta$ and $\pi^0\pi^0$. No signal was observed [7]. We have also reported the first evidence for a new $q\bar{q}$ meson with a mass of 1660 MeV, the first radial excitation of the $a_2(1320) \rightarrow \eta\pi$ meson, observed in the annihilation channel $\pi^0\eta\eta$ with 1940 MeV/c incident antiprotons [8].

3.1 Annihilation in flight into three neutral pseudoscalars

Identifying the $s\bar{s}$ meson of the ground state scalar meson nonet is one of the most important issues in light quark spectroscopy which bear on the interpretation of the $f_0(1500)$ meson as the ground state scalar glueball [9]. This state is predicted in the 1700 MeV mass region where a meson, $f_J(1710)$ with controversial spin J (0 or 2), has been observed in previous experiments. This state cannot be produced in $\bar{p}p$ annihilation at rest as it lies too close to the $\bar{p}p$ threshold. On the other hand, the analysis of annihilation data in flight is complicated by the large number of contributing partial waves which increases rapidly with antiproton momentum. The Zürich group is therefore analyzing data at 900 MeV/c incident momentum, corresponding to a center of mass energy of 2050 MeV. We are searching for new scalar and tensor mesons [10] in the annihilation channels $3\pi^0$, $\pi^0\pi^0\eta$ and $\pi^0\eta\eta$ that led to our discovery of $f_0(1500)$ and $a_0(1450)$, but with stopped antiprotons [11]. These channels were reconstructed by selecting 0-prong events with six detected photons.

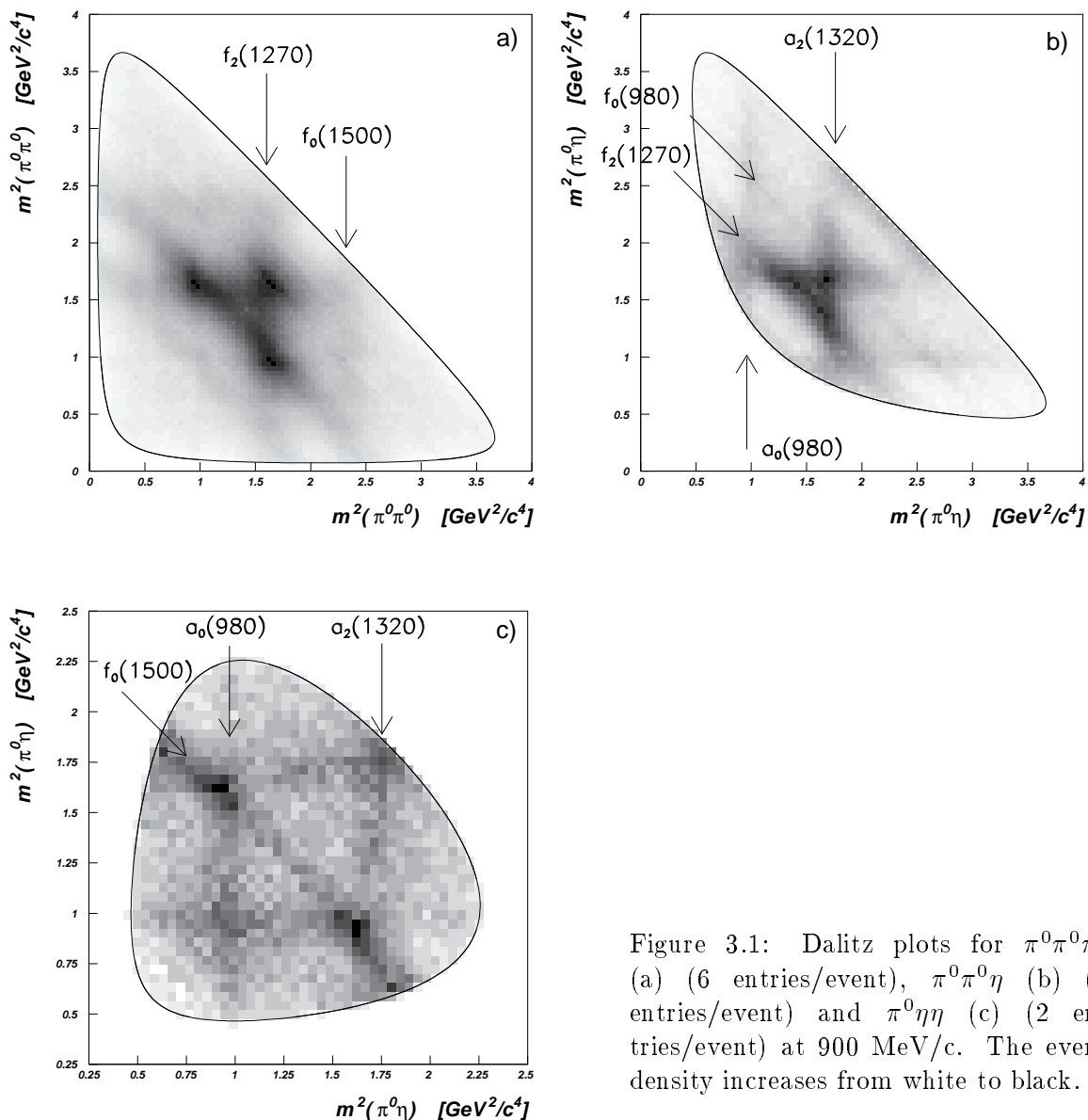


Figure 3.1: Dalitz plots for $\pi^0\pi^0\pi^0$ (a) (6 entries/event), $\pi^0\pi^0\eta$ (b) (2 entries/event) and $\pi^0\eta\eta$ (c) (2 entries/event) at 900 MeV/c. The event density increases from white to black.

With stopping antiprotons the coordinate of the annihilation vertex along the beam axis was distributed within a few 100 μm of the target center due to the low momentum (200 MeV/c) and the excellent momentum resolution of the incident beam. It was therefore assumed to lie at the center of the detector for all events. For annihilation in flight, however, the vertex distribution was spread uniformly along the full length (4 cm) of the hydrogen target. Since for neutral events the vertex coordinates could not be observed directly, we had first to develop a kinematic fitting algorithm using the mass constraints of the decaying π^0 and/or η as well as energy and momentum conservation [10].

The energy calibration of the CsI barrel was performed by adjusting the measured photon energies to match the π^0 mass, assuming that the average vertex position (target center) coincided with the detector center. However, in preliminary analyses of in-flight data the total energy deposited by the photons was 3% smaller than expected from the LEAR \bar{p} momentum. This was recently traced to the erroneous calibration procedure, as events with charged tracks indicated a substantial mismatch between the target and detector centers.

This displacement occurred during the modifications in the target geometry required for runs in flight. The calibration parameters had therefore to be recalculated and the in-flight data reprocessed entirely.

The data at 900 MeV/c were collected by vetoing charged particles from the microvertex detector and by the inner layers of the drift chamber. From the sample of 17 million annihilations into 0-prong one obtains about 3 million annihilations into 6γ . The minimum cluster energy for γ -detection was set to 20 MeV. The kinematic fit leads to about 5×10^5 $3\pi^0$, 1.5×10^5 $\pi^0\pi^0\eta$ and 2×10^4 $\pi^0\eta\eta$ events. The sizes of these samples are comparable to those obtained earlier at rest. The corresponding Dalitz plots are shown in fig. 3.1. Apart from the well known mesons one observes a clear signal from $f_0(1500)$ in $3\pi^0$ and $\pi^0\eta\eta$. There is no striking signal from any narrow state like $f_J(1710) \rightarrow \eta\eta$ or $\pi^0\pi^0$ in the 1700 MeV region. These are not necessarily bad news, however, since a pure $s\bar{s}$ state cannot be produced in $\bar{p}p$ annihilation, assuming no strange quarks in the proton. The absence of a spin zero $f_J(1710)$ in our data would argue against this state having a substantial admixture of glue or other quark flavours than strangeness in its wave function. A detailed partial wave analysis is in progress [10].

3.2 Annihilation at rest into $\pi^0\pi^0\omega$ and $\pi^0\eta\omega$

These channels are being studied in the 7γ final state where $\omega \rightarrow \pi^0\gamma$ and $\pi^0(\eta) \rightarrow \gamma\gamma$ [12]. They have been studied earlier by Crystal Barrel [13, 14], albeit with much lower statistics. The channel $\pi^0\pi^0\omega$ is interesting to search for scalar mesons decaying into $\pi^0\pi^0$ and for vector mesons decaying into $\omega\pi^0$, the channel $\pi^0\eta\omega$ to look for axial vectors decaying into $\omega\eta$.

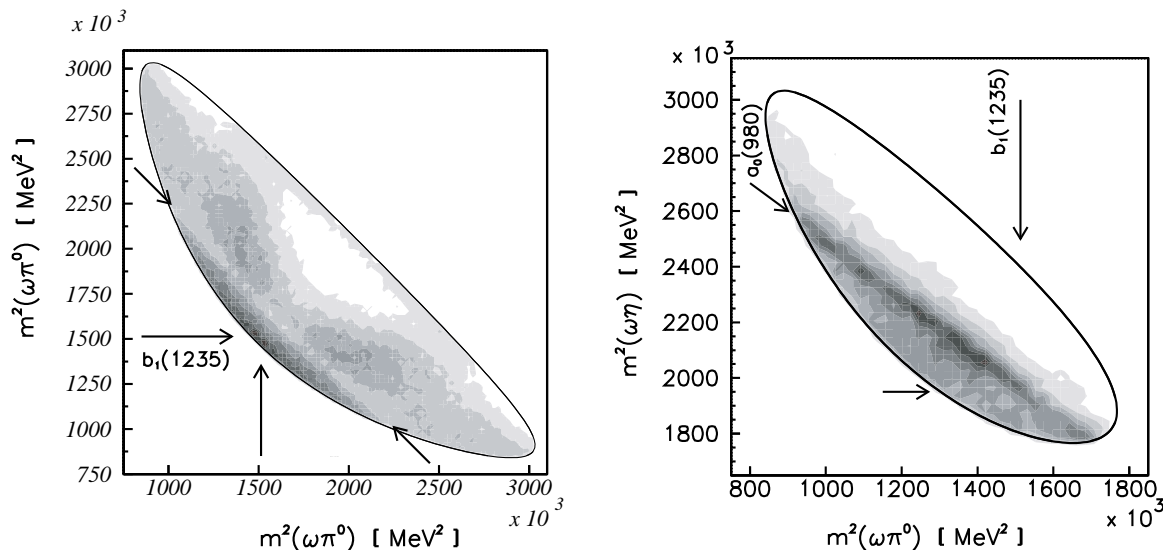


Figure 3.2: Left: Dalitz plot for $\pi^0\pi^0\omega$ at rest (136'023 events, two entries per event). The diagonal arrows mark the valley due to $f_0(980)$ in the $\pi\pi$ invariant mass spectrum. Right: Dalitz plot for $\pi^0\eta\omega$ (34'064 events). The horizontal arrow shows the region where a new state is required by the fit (see next figure).

In this final analysis we selected from our full sample of 2×10^7 0-prong events in liquid hydrogen at rest about 1.6 million events with 7γ . The events were then submitted to a kinematic fit to the hypotheses $\pi^0\pi^0\omega$ and $\pi^0\eta\omega$ (8 constraints fits). The acceptances were studied by Monte Carlo simulation. The reconstruction efficiency was 12.4 %, respectively 20.6 %. The annihilation frequencies were determined to be $(2.8 \pm 0.3 \pm 0.4)\%$ and $(1.1 \pm$

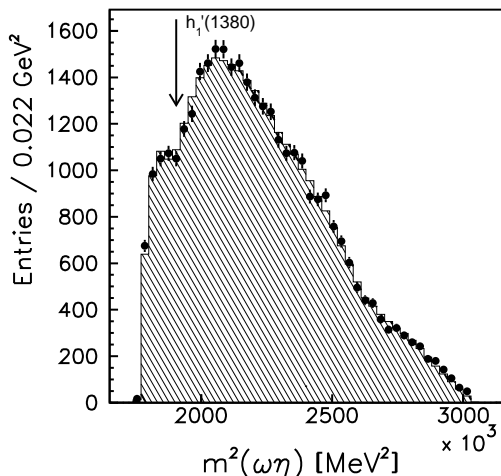


Figure 3.3: $\eta\omega$ mass distribution. The hatched histogram is the fit result including $h'_1(1380)$.

0.1 ± 0.3)% of all annihilations, respectively, where the first error is statistical and the second is systematical.

The Dalitz plots are shown in fig. 3.2. The $\pi^0\pi^0\omega$ Dalitzplot is dominated by the production of $b_1(1235) \rightarrow \omega\pi$, by the $\pi\pi$ S-wave and by the tail of the $f_2(1270) \rightarrow \pi\pi$ (accumulation of events at the lower edge). A background of about 9% is due to the $4\pi^0$ final state with one missing (undetected) photon. In contrast to our earlier work [13] we are now also fitting the angular distribution (θ and ϕ) of the decay photon in the rest frame of the $\omega \rightarrow \pi^0\gamma$, in addition to the $\omega\pi^0$ invariant masses. Substantial improvements were also made in the spin analysis procedure [12]. The diagonal valley around 1000 MeV in fig. 3.2 is due to $f_0(980) \rightarrow \pi\pi$. This dip which could not be described satisfactorily before is now fully understood using our K-matrix formalism.

The $\pi^0\eta\omega$ Dalitz plot is dominated by the production of $b_1(1235)$ and $a_0(980) \rightarrow \eta\pi$. In contrast to our earlier work [14] the $a_0(980)$ is now described by a K-matrix taking into account the unobserved $K\bar{K}$ decay mode which leads to an asymmetric mass distribution. The new feature is the observation of an enhancement in the $\omega\eta$ distribution just above threshold (fig. 3.2). This peak is consistent with a 1^{+-} isoscalar meson at 1380 MeV, decaying to $\omega\eta$. The $s\bar{s}$ partner of the $h_1(1170)$ is not well established. A signal, $h'_1(1380)$, was reported in K^-p interactions [15] and also by Crystal Barrel [16], however in the $K^*\bar{K}$ decay mode. A detailed partial wave analysis is in progress [12].

References

- [1] C. Amsler, Rev. Mod. Phys. **70** (1998) 1293
- [2] A. Abele *et al.* (Crystal Barrel Collaboration), Phys. Lett. **B 423** (1998) 175
- [3] A. Abele *et al.* (Crystal Barrel Collaboration), Phys. Lett. **B 446** (1999) 349
- [4] C. Amsler *et al.* (Crystal Barrel Collaboration), Phys. Lett. **B 358** (1995) 389
- [5] J.S. Suh (Crystal Barrel Collaboration), Workshop on Hadron Spectroscopy, Frascati (1999)
- [6] C. Caso *et al.* (Particle Data Group), Eur. Phys. Journal **3** (1998) 1
- [7] J. Kisiel (Crystal Barrel Collaboration), Workshop on Hadron Spectroscopy, Frascati (1999).

- [8] A. Abele *et al.* (Crystal Barrel Collaboration), Eur. Phys. Journal (in print)
- [9] C. Amsler C. and F.E. Close, Phys. Rev. **D 53** (1996) 295
- [10] M. Heinzemann, PhD Thesis, Universität Zürich (in preparation)
- [11] C. Amsler *et al.* (Crystal Barrel Collaboration), Phys. Lett. **B 355** (1995) 425
- [12] P. Giarritta, PhD Thesis, Universität Zürich (in preparation); Proc. LEAP'98 Conf., Villasiumius, Sardinia (1998)
- [13] C. Amsler et al. (Crystal Barrel Collaboration), Phys. Lett. **B 311** (1993) 362
- [14] C. Amsler et al. (Crystal Barrel Collaboration), Phys. Lett. **B 327** (1994) 425
- [15] D. Aston et al., Phys. Lett. **B 201** (1988) 573
- [16] A. Abele et al. (Crystal Barrel Collaboration), Phys. Lett. **B 415** (1997) 280

4 Particle Physics at LHC/CMS

4.1 Pixel Detector

C. Amsler, M. Glättli, R. Kaufmann, F. Ould-Saada, H. Pruys, P. Riedler, C. Regenfus, S. Spanier and S. Steiner

In collaboration with: ETH-Zürich, Paul Scherrer Institut (PSI), Universität Basel and the CMS Collaboration.

4.1.1 Silicon Microstrip Telescope

To study the performance of pixels foreseen for the CMS microvertex detector we have built in our mechanical workshop a precision beam defining telescope (fig. 4.1.1). This device was described in details in last year's annual report. It is made of 4 modules, each containing two $32 \times 32 \text{ mm}^2$ single-sided microstrip silicon wafers manufactured by SINTEF (Oslo), one providing the x -coordinates and the other the y -coordinates. A microstrip detector contains 1280 strips with a pitch of $25 \mu\text{m}$. Every second strip is connected to the readout electronics and the charge collected by the floating strips induces a charge on the readout strips by capacitive coupling. The readout is triggered by upstream and downstream scintillation counters. The signals from the 640 active strips are amplified and stored in VA2 Viking chips (shaping time $2.3 \mu\text{s}$). The analog charge is then read out sequentially and stored in Flash ADC's (CAEN VME V550). The data acquisition is controlled by a PC running Labview. The total length of the telescope is 59 cm. The space between the two upstream and the two downstream modules (35 cm) is used e.g. for the pixel detector prototype mounted on a rotating support.

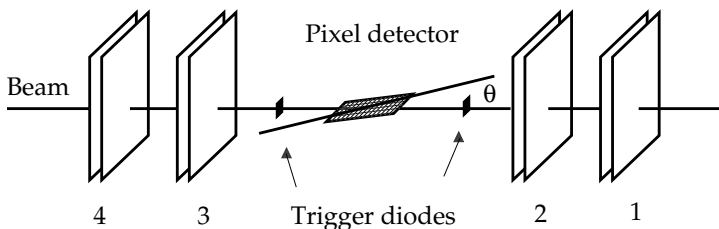


Figure 4.1: Sketch of the microstrip telescope.

The telescope was exposed to a 100 GeV muon beam at the SPS. A signal to noise ratio of 130 for minimum ionizing particles was achieved. The hit coordinates were determined accurately by measuring the energy deposits shared between adjacent strips. The precise alignment was achieved by software with a large number of passing muons. Preliminary results for the resolution were already reported in last year's annual report. Each readout plane provides the x or y coordinates of a traversing particle with a resolution of $\sigma = 1.8 \mu\text{m}$. The coordinates of a track hitting the test device in the center of the telescope can be determined with a precision of $\sigma \simeq 1 \mu\text{m}$ [1].

4.1.2 Pixels

The final design of the CMS pixel detector was submitted to CERN in 1998 [2]. The barrel detector is made of three cylindrical layers, 53 cm long with radii of 4, 7 and 11 cm, the first layer being used only during initial low luminosity runs. The support structures are made of tubes providing cooling to -10° with C_6F_{14} , connected with carbon fibre blades and supported at both ends by carbon fibre rings.

Each layer is made of two half-cylinders to allow insertion into the CMS detector. Figure 4.1.2 shows a full size prototype of one of the supporting half cylinders which was built in our mechanical workshop. The prototype uses titanium tubes and a ceramic substrate. The former will be replaced by aluminium and the latter will be replaced by carbon fibres to minimize multiple scattering. A cooling manifold is available at each end within the carbon fibre end flanges.

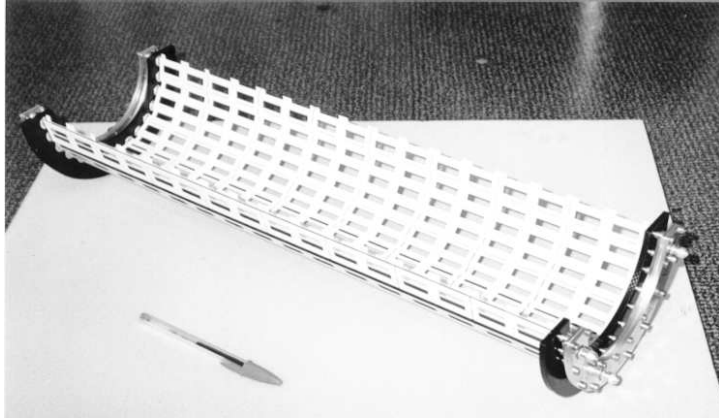


Figure 4.2: Full scale prototype of the mechanical support structure for one of the CMS pixel detectors.

A pixel unit cell contains 53×52 pixels. The dimensions of the (square) pixels have been increased from $125 \mu\text{m}$ in the original proposal to $150 \mu\text{m}$. Two rows of 8 cells build a module and a row of 8 modules builds a facet of length 53 cm and width 1.75 cm. The total number of pixels to be read out is about 3×10^7 . The bulk material is n -type and the pixel implants are n^+ .

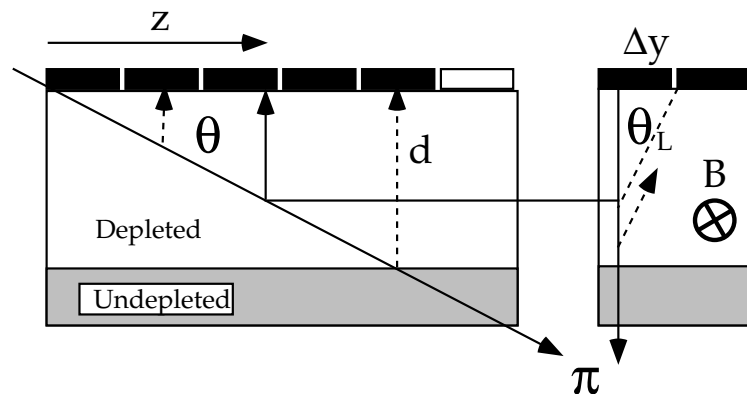


Figure 4.3: a) Measurement of the depletion depth with particles traversing the detector at a known grazing angle θ . The first and last row of fired pixels determine the depletion thickness d ; (b) In the presence of a longitudinal magnetic field the charge migrates towards the adjacent column under the angle θ_L .

In the high rate environment of LHC, type inversion will occur, the bulk material then acting as p -type. These radiation defects will slowly reduce the depletion thickness for a given bias voltage. We therefore measured in spring 1998 at CERN [1] the depletion depth for the two prototype pixel detectors that were manufactured earlier by CSEM in Neuchâtel, one of which had been irradiated at PSI with 6×10^{14} pions/cm². This flux corresponds to

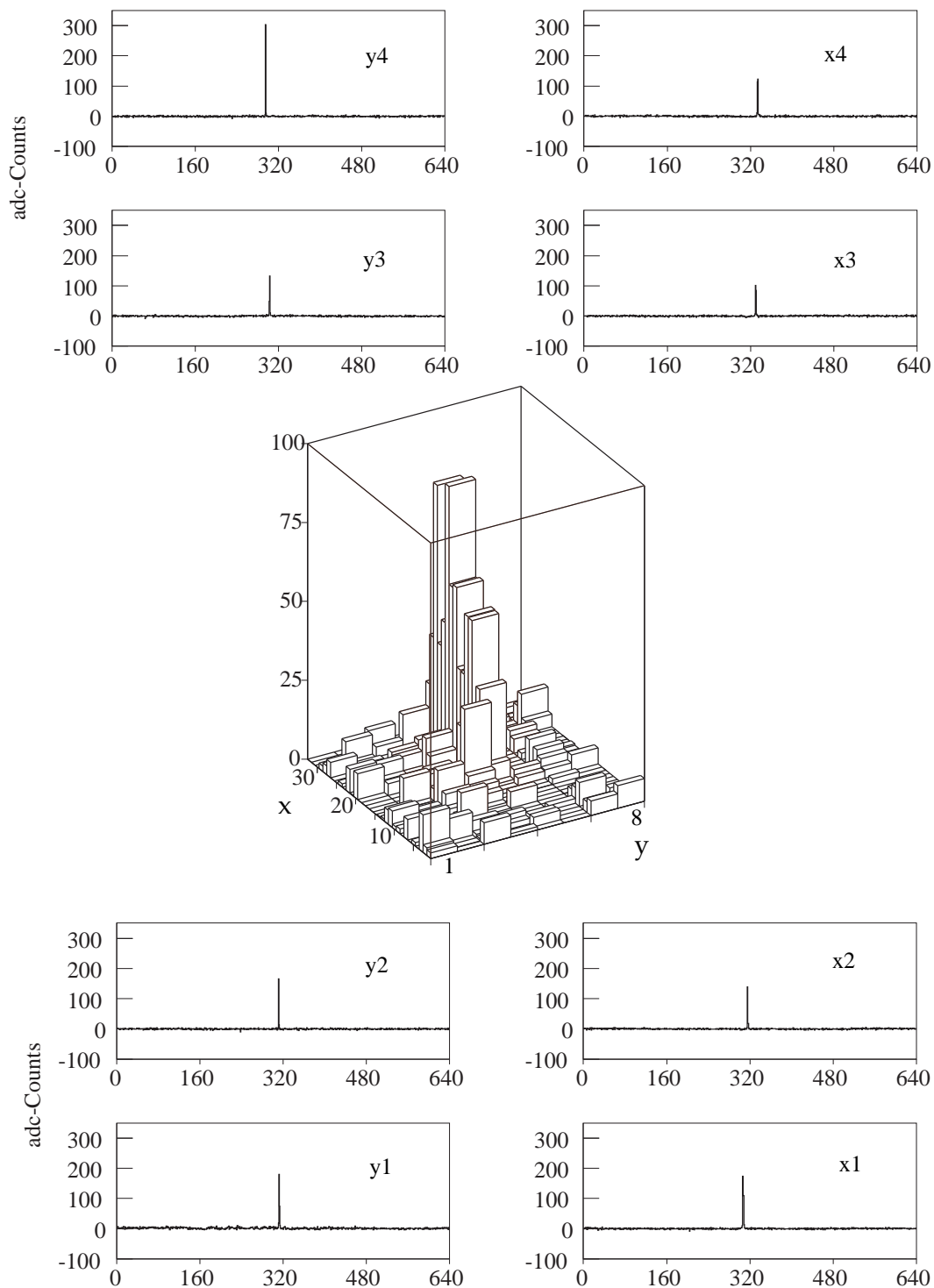


Figure 4.4: Typical pion track detected by the eight microstrip detectors in coincidence with the pixel device. The figure shows the distributions of charge deposits as a function of position after pedestal subtraction.

the operation of the pixel device at the radius of 7 cm during 6 years at the maximum LHC luminosity. The irradiation was performed in late 1996 and the detector was subsequently stored at a temperature of 3°C. To minimize multiple scattering effects the measurements were made at the SPS in a 225 GeV π^+ beam. The detectors had 8 columns and 32 rows of silicon pixels each covering a surface of $125 \times 125 \mu\text{m}^2$ (thickness 285 μm), leading to an active area of $1 \times 4 \text{mm}^2$. The pixel detector was positioned horizontally at the center of the microstrip telescope, so that pions would traverse the detector at a grazing angle $\theta = 8^\circ$ (see fig. 4.1.1). The depletion thickness could be measured by counting the number of hit pixels along the beam direction (fig. 4.3a). The apparatus was immersed in a longitudinal magnetic field provided by two Helmholtz coils to also measure the Lorentz angle, as will be explained below.

The readout electronics was triggered by two $2 \times 2 \text{mm}^2$ silicon diodes placed immediately upstream and downstream of the pixel detector. For the pixel readout we used the same Flash ADC system as for the telescope. The precise orientation of the pixel detector (e.g. the angle θ) was determined with the telescope using straight tracks and comparing the predicted entrance coordinates with the measured ones. Figure 4.4 shows a typical track detected by the eight silicon layers of the telescope and the corresponding energy deposits in the fifth column of the pixel detector. The average signal over noise ratio (~ 130) for the silicon strips is much larger than for the pixels (~ 5) due to the much longer integration time.

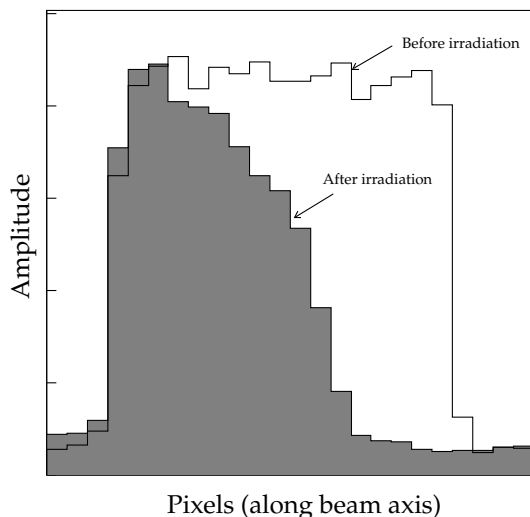


Figure 4.5: Amplitude distribution along the beam axis as a function of pixel row. The grey histogram shows the reduction in depletion depth due to radiation damages.

Figure 4.1.2 shows the amplitude distribution (without magnetic field) along the beam direction before and after irradiation. The typical “road” length of 18 pixels before irradiation corresponds to a depletion depth of 285 μm (achieved with a bias voltage of -144 V), in accord with the physical thickness of the detector. For the irradiated detector the significantly shorter road length indicates a depletion thickness of about $164 \pm 17 \mu\text{m}$ (bias voltage of -300 V), 18 months after irradiation. A similar measurement performed at PSI immediately after irradiation led to a depletion length of about 150 μm . The smooth decrease of the collected charge along the road is due to trapping of the charge carriers by defects, an effect that is proportional to the total drift length.

The angle θ being small we assume the electric and magnetic fields to be orthogonal. Due to deflection in the magnetic field the charge carriers do not move along the electric field lines but drift at an angle θ_L , the Lorentz angle, towards the adjacent column (fig. 4.3b). The charge deposit is therefore shared among (mostly two) adjacent pixels. Figure 4.1.2 shows the pixel roads for the two detectors in a longitudinal magnetic field of $\pm 3 \text{T}$. One observes

the increasing charge collection with road length - hence depth - by the adjacent left or right columns, depending on the sign of the magnetic field.

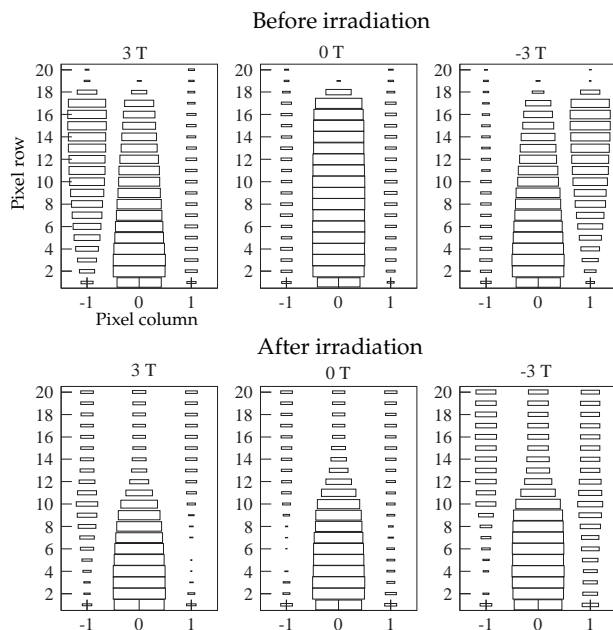


Figure 4.6: Energy deposits in a longitudinal magnetic field of 0 and ± 3 T. The pions enter the pixel detectors in the central column at the bottom of the figures. The size of the box is proportional to the charge deposited in each pixel. The distance between the (square) pixels is $125 \mu\text{m}$.

The Lorentz angle was measured by finding the coordinate z of the pixel row for which the charge collected between the main and adjacent pixels are equal (see fig. 4.3b). This corresponds to charge reaching the readout surface between two pixels. The coordinate Δy of the impinging track was determined by the telescope and θ_L could be calculated from the relation $\tan\theta_L = \Delta y/z \tan\theta$. We found a Lorentz angle of $(13.1 \pm 1.1)^\circ$ at 2 T before irradiation and $(12.3 \pm 2.7)^\circ$ after irradiation, which does not indicate a strong dose dependent effect. These figures are also in agreement with an earlier measurement from our group [3].

In conclusion, the depletion thickness and the Lorentz angle for irradiated detectors will be sufficiently large to permit charge sharing among adjacent pixels in the 4 T field of the CMS detector. In 1999 we will proceed with beam tests of a novel pixel sensor designed by the Zurich group. So far the pixel signals were fed to the preamplifiers through readout strips, while in the final CMS device the pixels will be connected to the chips through indium bumps [2]. The first indium bump bonded pixels will be exposed to our test beam facility this year.

References

- [1] M. Glättli, Diplomarbeit, Universität Zürich (1998)
- [2] Technical Design Report of the CMS Tracker, CERN/LHCC 98-6 (1998)
- [3] R. Kaufmann, Diplomarbeit, Universität Zürich (1997)

5 Production and Spectroscopy of Antihydrogen

C. Amsler, E.A. Hermes, P. Niederberger, H. Pruyss, C. Regenfus, P. Riedler and J. Rochet

In collaboration with: CERN, LANL (Los Alamos), Pennsylvania State University, Universities of Aarhus, Brescia, California (San Diego), Genoa, Napoli, Pavia, Pisa, Rome, Stockholm, Tokyo; University College (London), University Escola Tecnica Federal do Ceara (Brazil) (ATHENA Collaboration).

The goal of the ATHENA (AnTiHydrogEN Apparatus [1]) experiment is to produce antihydrogen atoms at low energies, to capture them in a magnetic trap and to compare by 2 photon laser excitation the $1S - 2S$ energy difference of antihydrogen with the one for hydrogen, in view of testing CPT invariance at the level of about 1 part in 10^{15} .

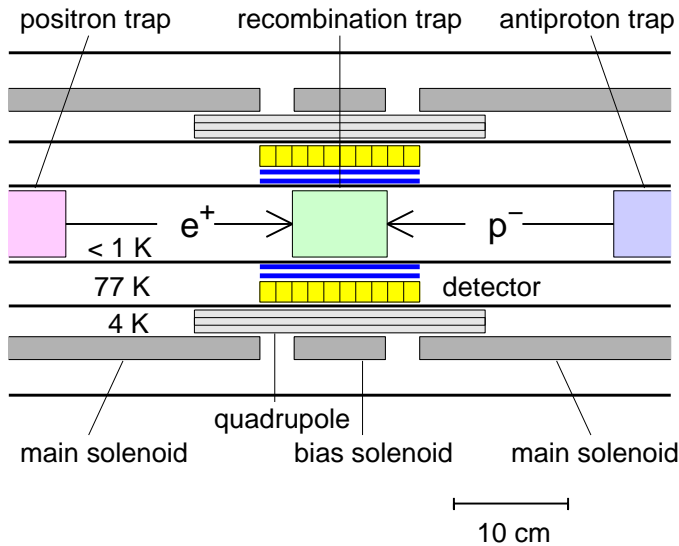


Figure 5.1: *Central part of the ATHENA superconducting solenoid with the recombination trap and the annihilation detector. Parts of the positron trap and the antiproton trap are also shown.*

The apparatus consists of a superconducting solenoid (3 T) with a cold bore to house the antiproton trap, the positron storage trap, and the \bar{H} trap (fig. 5.1). Antiprotons will be extracted from the Antiproton Decelerator (AD) at CERN, captured in an electromagnetic field configuration known as a Penning trap, and cooled to sub-eV temperatures by electron cooling. Large number of positrons from a ^{22}Na source will be accumulated in a similar field configuration.

One of the major challenges will be bringing the antiprotons and positrons in close contact for a time sufficiently long to allow the antihydrogen formation process to take place. To combine positrons with the antiprotons a nested Penning trap, a series of coaxial cylindrical electrodes with alternating electric fields, will be used.

Once antiprotons and positrons have been recombined, the confinement by the electric forces ceases and the antihydrogen atoms would escape, hit the walls of the recombination trap and annihilate. To confine the produced antihydrogen atoms magnetic gradients interacting with their magnetic moment can be used. This requires superimposing a strong magnetic gradient field onto the constant field necessary for the Penning trap. A combination of quadrupole coils for radial confinement and solenoids for the axial confinement will be used.

In the first phase of the experiment we will study the formation rates of antihydrogen atoms and their capture in a magnetic gradient trap, by observing the annihilation of antihydrogen atoms impinging on the walls surrounding the antihydrogen trap with an appropriate detector. The unambiguous proof of antihydrogen formation will be obtained by detecting the antiproton annihilation products and measuring the annihilation vertex in time coincidence with the two back-to-back 511 keV photons from e^+e^- annihilation.

The Physics Institute of the University of Zürich is responsible for a major part of the antihydrogen annihilation detector (mechanical structure, Si microstrip detector, photodiodes and read out electronics).

5.1 Silicon microstrip detector

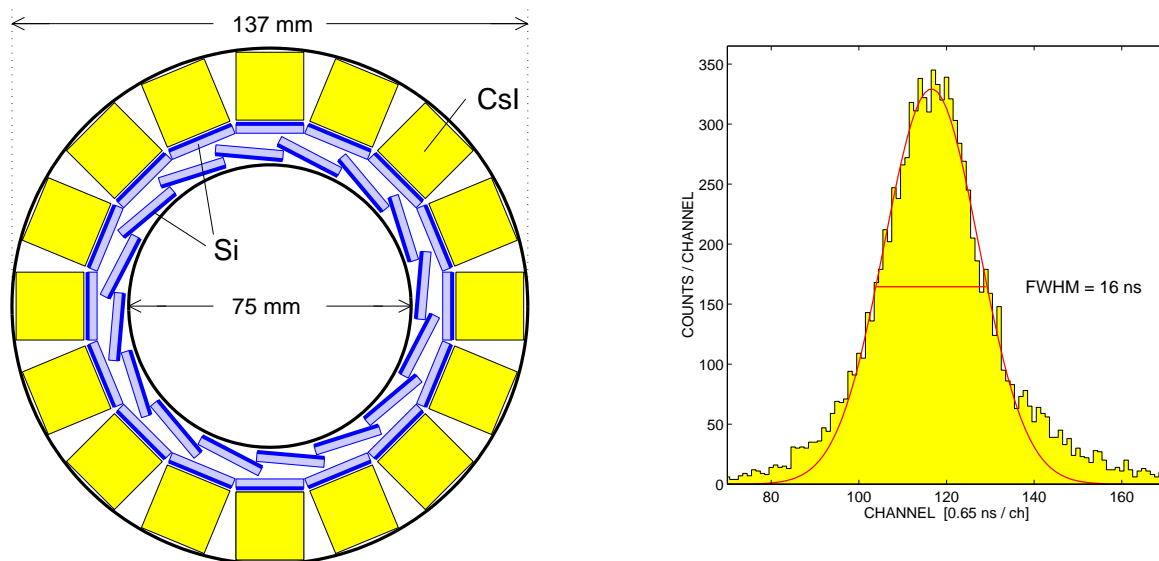


Figure 5.2: *Left: Front view of the ATHENA annihilation detector.*

Right: Time resolution of the Si microstrip detector obtained by measuring the time difference of minimum-ionizing particles passing through a fast plastic scintillator and the Si microstrip detector.

The Zurich group is responsible for the design, construction and readout of the microstrip vertex detector surrounding the antihydrogen trap which will signal the annihilation of stored antihydrogen. In 1998 we proposed a design which ensures a large angular coverage and therefore a high detection efficiency. The layout is shown in fig. 5.2. It consists of two cylindrical layers of 16 silicon microstrip modules, 76 and 96 mm in diameter, respectively. The 32 modules contain double sided AC coupled detectors of 160 mm length and 400 μm thickness, with a width of 19 mm. One surface (direction along the detector axis) will be read out through 128 pads and the other ($r\phi$) will be read out by 128 strips (pitch 150 μm). The total number of channels is 8192. These will be multiplexed into 32 analog outputs by 64 readout chips. A similar vertex detector has been built for the Crystal Barrel experiment [2].

We are currently investigating the performance of the detector and the readout chips at 77 K with encouraging results. Good energy and time resolutions are obtained (fig. 5.2).

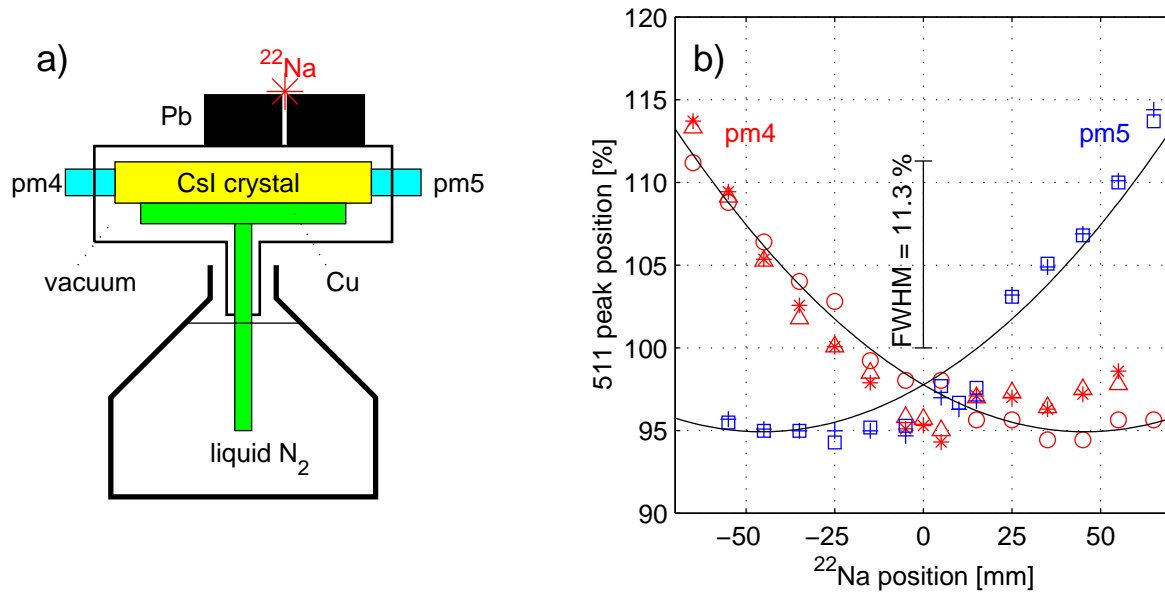


Figure 5.3: a) Sketch of the apparatus to measure the crystal response (light output and decay time) from 511 keV photons at cryogenic temperatures. Dimensions of crystal: $2.5 \times 2.5 \times 15.5$ cm³. b) Dependence of light output on the position of the ²²Na source (0: middle of crystal).

5.2 Test of CsI crystals

We also provide assistance in developing the crystal detector (main responsibility: University of Pavia) that will detect the annihilation of the positron. We are currently investigating the properties of pure CsI and CsI(Na) at different temperatures with positron sources. An earlier result from the Italian group indicated a substantial increase in light output for pure CsI with decreasing temperature. We have built a test bench at cryogenic temperatures to measure the light output as a function of position z along the crystal (fig. 5.3a) and have succeeded in detecting the 511 keV photons entering 15 cm long crystals at the opposite end to the readout. In the ATHENA experiment we planned to determine z by comparing the amplitudes of signals from both ends of the crystal. However, the energy resolution is not sufficient (fig. 5.3b). Therefore, we will subdivide the crystals along their lengths in 12 elements, each read out by four photodiodes.

The crystals will be manufactured by industry or by the University of Tbilisi. First results on test crystals show good energy resolution and an acceptable decay time at low temperatures (fig. 5.4).

These measurements were done using photomultipliers (Hamamatsu R1450). For the annihilation detector photodiodes have to be used. First crystal tests with photodiodes coupled to the same readout chip as for the Si strips show an acceptable signal to noise ratio (FWHM of 511 keV peak: 25 %).

The detector will be assembled in summer 1999 and first runs with antiprotons from the AD are scheduled in autumn.

References

- [1] ATHENA proposal, CERN SPSLC 96-47, <http://www.cern.ch/athena/>

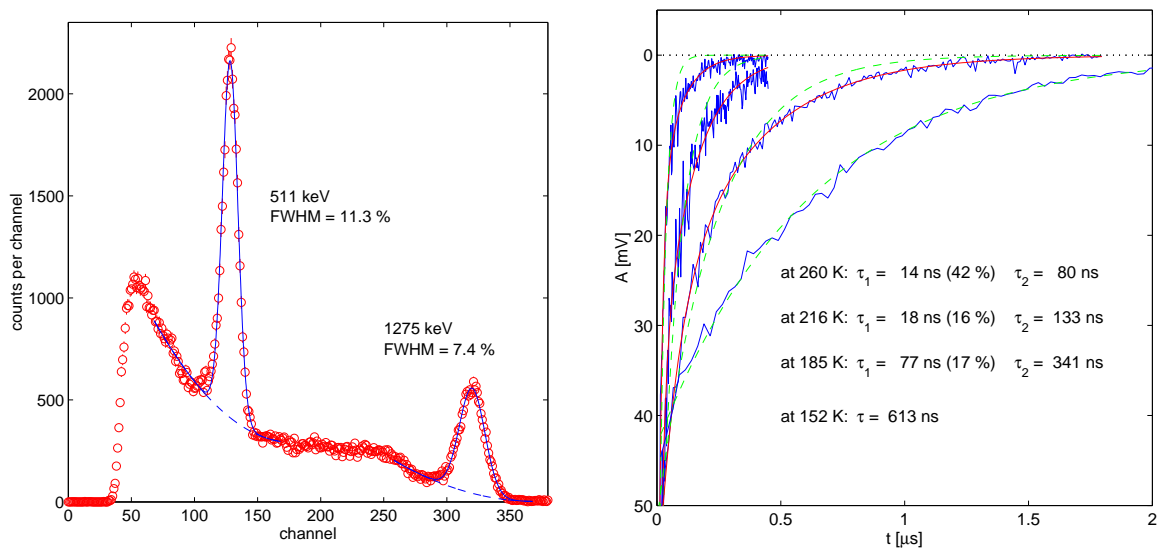


Figure 5.4: *Left: Energy resolution of a pure CsI crystal (University of Tbilisi) measured with a ^{22}Na source at 120 K. Right: Time response of the same crystal at different temperatures. At the three higher temperatures two time components are observed. At the lowest temperature the decay curve can be described by one exponential.*

[2] M. Doser et. al., NIM A412 (1998) 70

6 Measurement of the Neutrino Magnetic Moment at the Bugey Nuclear Reactor

C. Amsler, P. Giarritta, M. Heinzelmann, O. Link, and F. Ould-Saada

In collaboration with Institut des Sciences Nucléaires (Grenoble), Université de Neuchâtel,
 Università di Padova
 (MUNU Collaboration)

The MUNU experiment is currently taking data at the Bugey nuclear reactor near Lyon. The aim is to study $\bar{\nu}_e e^-$ scattering in order to test the standard model at low energies and to improve on the present laboratory upper limit for the magnetic moment of the electron antineutrino ($1.8 \times 10^{-10} \mu_B$) by an order of magnitude. A magnetic moment of the order of a few $10^{-11} \mu_B$ would lead to spin precession in the solar magnetic field [1] and could explain the deficit of solar neutrinos. In the standard model the neutrino may acquire a magnetic moment proportional to its mass. Masses of order $10 \text{ MeV}/c^2$ imply very small values $\mu_\nu \sim 10^{-18} \mu_B$. Much larger values would mean onset of new physics.

MUNU is a low background detector based on a time projection chamber (TPC) filled with CF_4 gas at 3 bar, 158 cm long and 90 cm in diameter. The TPC is surrounded by an anticompton shield (NE235 based liquid scintillator), 50 cm thick, to convert and veto γ -rays which scatter in the gas and generate low energy recoil electrons. The scintillation light is detected by 48 photomultipliers, 24 on each lid. The liquid scintillator tank is shielded by 15 cm of lead. Neutrons generated by muon capture in the lead are attenuated and absorbed by 8 cm thick CH_2 plates covered with B_4C sheets. Details on the apparatus can be found in ref. [2].

The cathode (negative high voltage) is at the opposite end of the readout plane. The anode wires are electrically connected to provide a total energy trigger signal. Two planes of 256 perpendicular strips (3.3 mm pitch) register induced signals and define the x, y coordinates. The z coordinate along the detector axis is obtained through the time evolution of the signal. The anode, strip and photomultiplier signals are sampled by a 25 MHz - flash ADC system. Both energy and direction of the recoil electron are measured. The background (isotropic and expected to be 4 events/day) can be measured during reactor operation by looking at events with electrons emitted into the backward hemisphere. Another advantage is the capability to reconstruct the incident neutrino energy. The threshold on the electron recoil energy is set around 300 keV, giving the experiment a good sensitivity to the magnetic moment of the $\bar{\nu}_e$.

The Zurich group, see previous reports for more details, is responsible for the TPC readout and for the data acquisition system which is fully operational in the experimental area.

We recall the main results obtained last year. The energy resolution was measured with 60 keV photons from an ^{241}Am source. It is found to be $\sigma = 25 \%$ at 60 keV, corresponding $\sigma \simeq 10 \%$ at 500 keV. A spatial resolution of $\sigma = 1.6 \text{ mm}$ has been achieved for the cathode strips by fitting muon tracks with straight lines. The mean attenuation length of drifting electrons at 3 bar was measured to be $22 \pm_{-6}^{+14} \text{ m}$ [2]. With a small prototype of the TPC and a ^{112}Sn radioactive source we measured the angular resolution of electrons [3]. We obtained an angular resolution of $\sigma_{\theta_{space}} = 13^\circ$ for 370 keV electrons, in agreement with simulation.

Since several triggers (neutrinos, radioactive sources, muons, etc) are being used, we have developed this year a general purpose trigger module (based on the LRS 2366 Universal Logic Unit, ULM) which allows to adjust remotely the coincidences and timing for every trigger. The system is working very well [4] and has been implemented into the data acquisition system, based on a FIC 8234 CPU running under the OS9 operating system. The anticompton

shield was filled with 10 t of scintillator. The time projection chamber (Anode and cathode) was calibrated with passing muons and a ^{54}Mn source [4]. The photomultipliers were also calibrated with monochromatic photons from a ^{54}Mn source.

Figure 6.1(left) shows the projections $x-z$ and $y-z$ of a photon induced electron track, and the time distribution of the anode pulse. The reconstructed $x-y$ projection is also shown (Fig.6.1(right)).

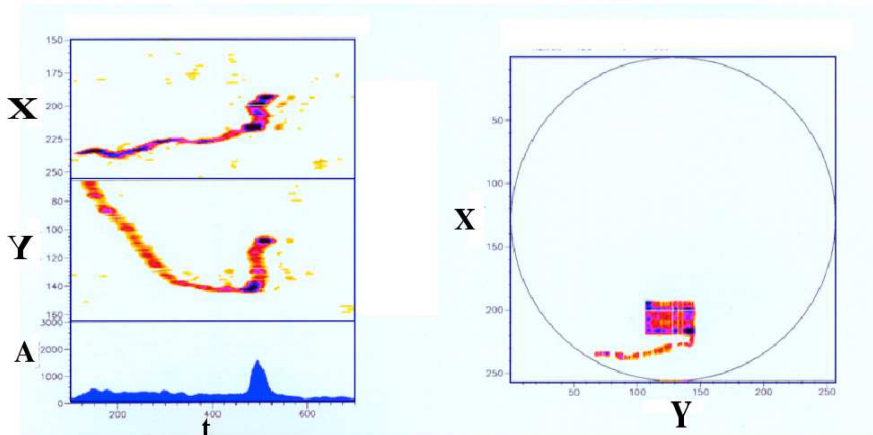


Figure 6.1: Left: $x-z$ and $y-z$ views of a photon induced electron track, and time distribution of the anode pulse. The dark area denotes large energy deposits at the end of the tracks. Right: Tentative reconstruction of the $x-y$ view.

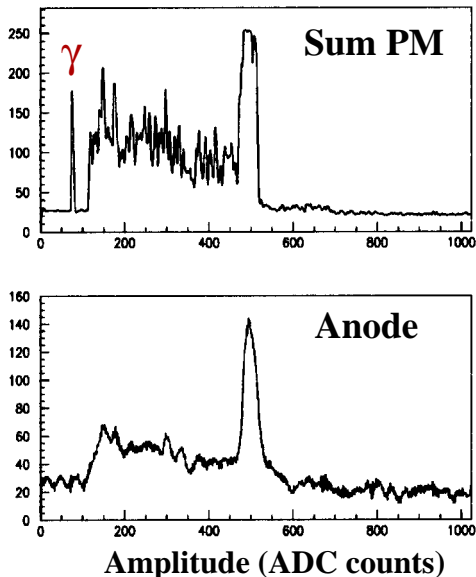


Figure 6.2: Amplitude distribution of the track shown in fig. 6.1. The anode signal (bottom) is also seen by the photomultipliers (top). The electron track is induced by a photon whose signal can be seen on left side of the photomultiplier pulse (top).

We have taken data and performed the calibration of the detector. In the last months we have made substantial progress in understanding the background, optimising the trigger and reducing the electronic noise.

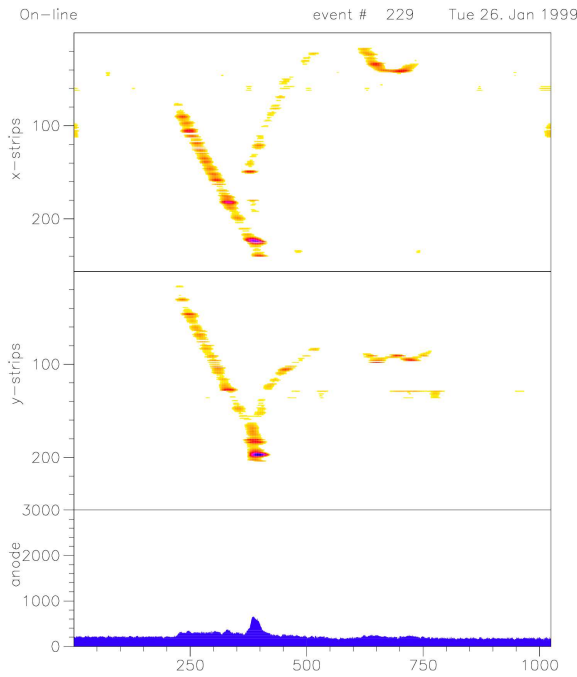


Figure 6.3: x - z and y - z views of a background event (muon capture), and time distribution of the anode pulse.

- Our trigger is made more complicated by the fact that CF_4 scintillates, so that the photomultipliers detect the light from the avalanche in the TPC (fig.6.2). However, neutrino induced pulses from the TPC can be distinguished from anticompton vetoes due to the long (max $40 \mu\text{m}$) drifttime unless neutrinos scatter close to the anode plane. Furthermore, in order to keep the anticompton information for further software reduction, the photomultipliers had to be read out in a separate FADC crate. This required more readout electronics than planned.
- The sensitivity of the experiment strongly depends on the level of background we can reach. Figure 6.3 shows a typical background event (muon capture) easily vetoed by the anticompton: The anticompton vetoes more than 99 % of the photon induced background. We have, however, observed 10 times more background than expected. We are now convinced that Radon, introduced in the gas by oxisorb filters, explains the high rates. Activity measurements confirmed that the oxisorbs we use contain quantities of Uranium much higher than foreseen. With a charcoal cold trap we noticed a steady decrease of background and could measure a lifetime of Radon of the order of 5.5 days. We are now in the process of replacing the big oxisorb by smaller low background ones.
- Electronic noise in the readout chain of the TPC has been drastically reduced. We are now confident that we can improve the signal to noise ratio by another factor of two, in which case zero suppression can be performed efficiently.

Cleaner data are being taken and work is progressing well.

Recently, interest in low energy neutrino - electron scattering has been boosted by the study of solar neutrinos. In order to explain the observed deficit in an independent way, it is necessary to measure the low energy neutrino spectrum with a good precision. A third generation solar neutrino experiment must fulfill two requirements: very good energy and

angular resolutions on one hand, and low background environment, on the other hand. A new solar neutrino experiment, SuperMUNU, is being discussed at the Gran Sasso laboratory [5]. The solar neutrino energy spectrum could be obtained with four 50 m^3 TPC's (4 meters diameter and 4 meters long) filled with CF_4 gas at 2 bar, and surrounded by 50 cm liquid scintillator. One would collect 700 events a year with an electron threshold of 100 keV. The angle of the electron (and hence the neutrino energy) is mandatory to resolve the pp and Be spectra. It will also be possible to see the pep neutrinos, provided the pressure is increased to ~ 5 bar.

References

- [1] F. Ould-Saada, UZH-PH 114/96, 45pp; and references therein
- [2] C. Amsler *et al.*, Nucl. Instrum. Methods **A 396** (1997) 115
- [3] S. Iseli, diploma thesis, University of Zurich (1996)
- [4] O. Link, diploma thesis, University of Zurich (1998)
- [5] MUNU internal note, january 1997.

7 Particle Physics at DESY/HERA

S. Egli, I. Foresti, S. Hengstmann, J. Kroseberg, D. Müller (until 12/98), P. Robmann, F. Sefkow,
 P. Truöl, S. von Dombrowski, T. Walter, and M. zur Nedden (until 12/98),
 in collaboration with
 R. Eichler, C. Grab, M. Hilgers, H.-C. Kästli, S. Lüders, D. Pitzl, A. Schöning,
 and Y. Tsipolitis, Institut für Teilchenphysik der ETH, Zürich,
 K. Gabathuler, J. Gassner, and R. Horisberger, Paul-Scherrer-Institut, Villigen,
 and 34 institutes outside Switzerland
 (**H1**-Collaboration)

7.1 Electron proton collisions at 300 GeV center of mass energy: overall status of the project

After the most successful year of HERA operation with positrons in 1997, the 1998 run started very late. The vacuum system of the electron ring had been rebuilt to accommodate running with electrons, and the vacuum pressure was rather high initially. Though the pressure improved continuously as expected, the lifetime of the beam was affected for most of 1998, as is evident from Table 7.1. The background conditions in the H1-detector worsened, too. Consequently the overall luminosity, the specific luminosity, the running efficiency did not reach the values of 1997. However, the energy of the proton ring was successfully raised from 800 GeV to 920 GeV, which lifts the available center of mass energy to 318 GeV. The cross section for the production of exotic objects with masses of about 200 GeV increases by a factor of two due to this energy change. Since the accelerators resumed operation in January 1999 already 9.7 pb^{-1} has been accumulated (25. 3. 1999). In March proton currents up to 90 mA and electron currents up to 30 mA lead to up to 15 HERA fills corresponding to 1.5 pb^{-1} per week. The data taking efficiency has also reached the higher level of 1997 again.

A final decision has not been taken, whether the remainder of 1999 after the short shut-down in May will be devoted to electron or positron running.

With last years modest increase of the total event sample, the physics analysis concentrated on finalising those analyses, where last year only preliminary results were available. The principal areas covered can be summarized as follows

- neutral and charged electroweak current cross sections, proton structure functions and parton densities in new domains of Bjorken x and momentum transfer Q^2 [1, 2],
- search for states outside the standard model [3, 4],
- diffractive processes and the structure of the pomeron [5, 6, 7],
- testing perturbative and non-perturbative quantum chromodynamics predictions and measurement of α_s [8, 9, 10, 11, 12, 13],
- parton-fragmentation into exclusive and multijet final states [14, 15, 16], and
- production of heavy quark-antiquark states, of open charm and determination of gluon density [17, 18, 19, 20, 21].

We will report below on the analyses in heavy quark sector, where most of the activity of the Zürich groups concentrates below, and also give an update of the data sample at highest momentum transfers ($Q^2 \approx M_W^2$).

Besides the physics analysis, our activities deal with the maintenance, monitoring and continuously improving of the detector components built at Zürich for the central tracker

Parameter	1993	1994		1995	1996	1997	1998
	e^-p	e^-p	e^+p	e^+p	e^+p	e^+p	e^-p
Integrated luminosity \mathcal{L}							
HERA produced [pb^{-1}]	1.00	0.94	5.1	11.4	14.4	37.6	8.7
HERA physics [pb^{-1}]	0.88	0.85	4.7	10.4	13.3	35.8	8.1
H1 taken [pb^{-1}]	0.57	0.53	3.6	6.4	8.9	30.4	6.5
H1 physics [pb^{-1}]	0.53	0.49	3.5	5.7	8.6	26.4	4.7
HERA efficiency [%]	88	90	94	91	92	95	92
H1 efficiency [%]	60	58	73	55	65	74	58
Average luminosity [$(\mu\text{b s})^{-1}$]	0.27	0.62	1.29	2.13	2.64	4.38	2.25
Peak luminosity [$(\mu\text{b s})^{-1}$]	1.3	2.6	4.3	5.9	8.4	10.1	8.8
Average p current [mA]	10.8	28.6	41.0	54.0	60.3	74.5	63.2
Average e^\pm current [mA]	7.7	10.5	17.0	18.4	20.6	28.0	15.5
Colliding bunches	84	153	153	174	175	175	175
Pilot (e, p) bunches	10,6	15,17	15,17	15,6	14,6	14,6	14,6
HERA luminosity runs	218	116	176	304	241	411	187
Permanent H1 runs	3190	1141	1816	4208	3582	5369	2769
Average duration [s]	817	1115	1620	884	1159	1431	1163

Table 7.1: Summary of HERA and H1 operation during the last six years.

and the first level trigger of H1. As in the past we also continued to be strongly involved in adapting the first level triggers to the varying beam currents and backgrounds at H1. Most of our effort, however was directed towards our contribution to the upgrade program of the H1-detector.

7.2 Summary of activities related to the Zürich H1-components and their upgrade

The investigation of rare processes at the limits of the kinematically accessible range at HERA requires a luminosity upgrade of the machine [22]. The most important aspect of this program is the improvement of the focussing properties near the interaction region of the H1 detector. The luminosity is expected to increase by a factor of seven to $L = 7.4 \times 10^{31} \text{ cm}^{-2}\text{s}^{-1}$.

Part of the H1 upgrade plan [23] is the replacement of the existing inner two proportional chambers (CIP) and the inner drift chamber (CIZ) by a new five-layer proportional chamber. The goal to improve z -vertex triggering and track reconstruction, as well as the rejection capability of background events from synchrotron radiation and proton beam gas interactions can be achieved by increasing the number of readout channels both along the z -axis and in azimuthal direction. The implementation of five chambers instead of two will help to resolve ambiguities from the central silicon tracker (CST). The increased number of readout channels also requires new readout and trigger electronics.

The new CIP will have pad readout in 16 azimuthal sectors. The trigger scheme is based on a projective geometry of the pads along the z -axis, thus requiring a varying number of pads in each layer ranging from 119 to 93 pads for the innermost and outermost layer, respectively.

The University of Zürich is responsible for the mechanical design and construction of the multiwire proportional chambers. The high density of readout channels and new front-end electronics made it necessary to build a cylindrical prototype of the innermost chamber for

which the space limitations are critical. The construction of this prototype at 1/3 of the full length has started end of 1998 and will be completed in spring of 1999. The inner cylinder of the prototype chamber consisting of the inner cathode and anode wire layer is shown in Figure 7.1. Testing of the detector and the electronics will be done using a pion beam at PSI.

The construction of the full-length five-layer chamber will start in early summer of 1999 and should be completed within 16 months, thus being ready for the installation in the H1 detector in September 2000 during the HERA shutdown.

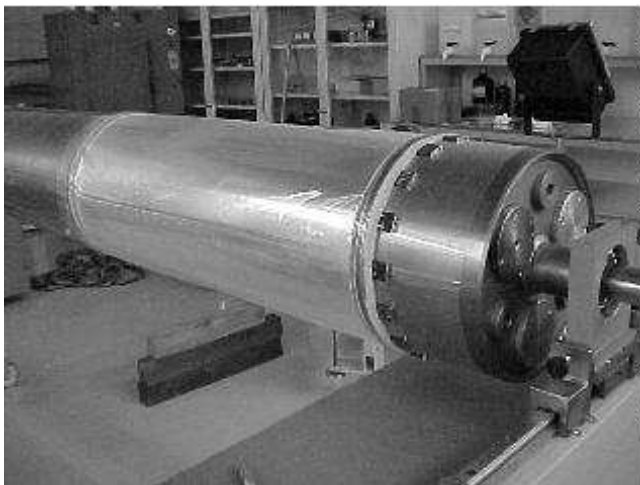


Figure 7.1: The prototype of the new central inner proportional chamber being built in the Physik-Institut shops.

7.3 Results from recent analyses

7.3.1 Deep inelastic scattering at highest momentum transfer and the standard model

The analysis of the high-momentum transfer ($150 < Q^2 < 30000 \text{ GeV}^2$) neutral and charged current data taken between 1994 and 1997 has been completed [24, 2]. We have already given some preliminary results last year. With an integrated luminosity of 36 pb^{-1} this analysis increases the statistics of the previously published results by an order of magnitude with smaller systematic errors and an expanded region of x_{Bjorken} and Q^2 . The proton structure function is extracted from the measured cross section $d^2\sigma/dxdQ^2$ and the Q^2 evolution of the parton densities predicted by quantum chromodynamics is tested for $0.0032 < x < 0.65$. No significant deviations from the electroweak standard model are found. The integrated cross section $d\sigma/dq^2$ (Figures 7.2 and 7.3) varies over seven orders of magnitude. The same holds for the preliminary data extracted from the electron runs (5 pb^{-1}) [1], which are also shown in Figure 7.2.

The published data sample comprises 75000 neutral current and 700 charged current events. The kinematical cuts are $E'_e > 11 \text{ GeV}$, $y_e = 1 - (E'_e/27.5) \sin^2(\theta_e/2) < 0.9$ for the neutral current (NC), and $p_T^{\text{miss}} > 12 \text{ GeV}$, $0.03 < y_{\text{hadron}} < 0.85$ for the charged current (CC) events. Photoproduction background is suppressed by requiring either $\sum E_i(1 - \cos \theta_i) > 35 \text{ GeV}$ (in a perfect detector without initial state radiation this sum would equal 55 GeV) for NC events, or for CC events the ratio of the transverse energy flow along the direction of the outgoing electron to that opposite to it to be less than 0.15.

The next to leading order QCD-fit shown superimposed to the data is derived from 235 H1 data points (including 77 from our previous analysis up to 1994 [25]) and 452 data points from previous fixed target experiments at the low Q^2 end. At the highest Q^2 the fit to the data requires the inclusion of the Z^0 -exchange in addition to γ -exchange in the NC-case. In

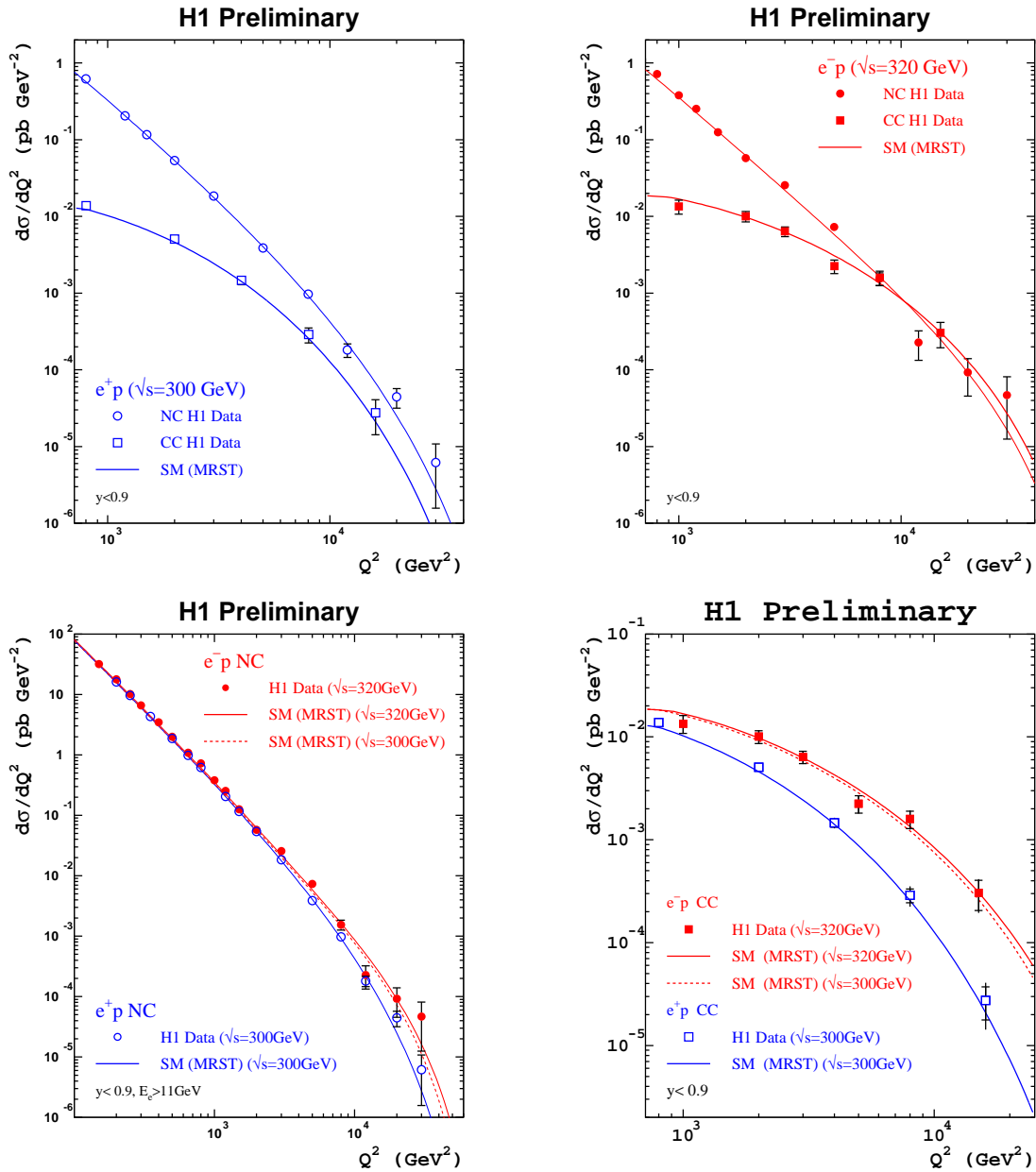


Figure 7.2: High momentum transfer charge and neutral cross sections for positron and electron deep inelastic scattering: e^-p preliminary data from 1998/99 (5 pb^{-1}) at $E_p = 920$ GeV and e^+p published data from 1994-97 (36 pb^{-1}) at $E_p = 800$ GeV.

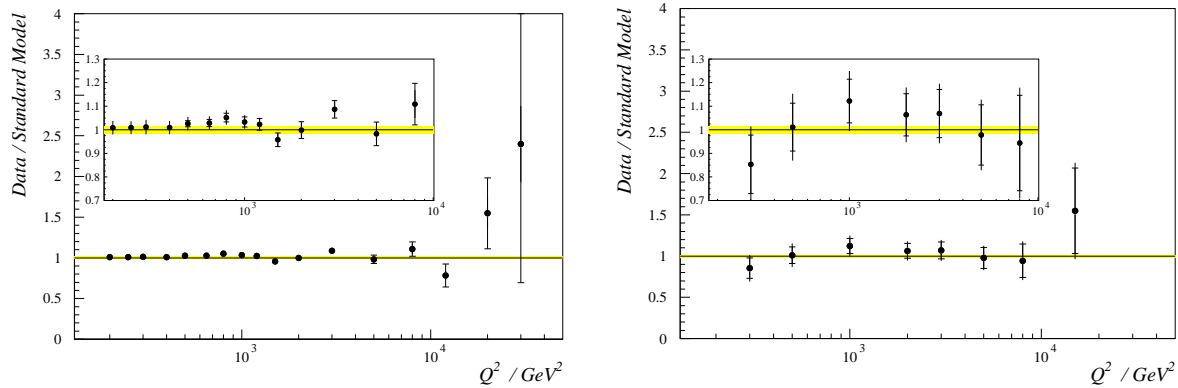


Figure 7.3: Ratio of the observed neutral (left) and the charged (right) current cross sections $d\sigma/dQ^2$ to that predicted by the standard model. The gray band indicates the normalisation error from the luminosity measurement. The inner error bars represent the statistical, the outer the systematical errors.

the CC-case the cross section is sensitive via the propagator term also to the mass of charged vector boson. We find $m_W = 79.2 \pm 3.1(\text{stat.}) \pm 1.6(\text{syst.}) \pm 3.5(\text{theor.})$. The inclusion of the 1997 data weakened the statistical significance of the deviations from the standard model prediction seen for $Q^2 > 10000 \text{ GeV}^2$ and $x \approx 0.4$ [24].

The data were also subjected to a thorough analysis searching for leptoquark bosons and lepton flavor violation [4]. The Yukawa couplings of first generation scalar and vector leptoquarks in the Buchmüller-Rückl-Wyler effective model [26] have been constrained, taking into account both s - and u -channel contributions as well as interference with standard model boson exchange. E. g. scalar leptoquarks are excluded with masses up to 275 GeV, for a coupling of electromagnetic strength. The exclusion limits derived improve not only previously extracted limits from HERA experiments, but also extend the coupling-mass domain covered so far at other colliders with a small branching ratio to eq . Leptoquarks possessing couplings to mixed fermion generations, which could lead to signals for lepton flavor violation are searched in events with a high transverse momentum μ or τ . No $\mu + X$ or $\tau + X$ event candidate is found that is compatible with the specific hypothesis of lepton flavor violation due to a leptoquark. The corresponding constraints can in some cases also extend the mass range set at other colliders and by low energy experiments such as $\mu \rightarrow e\gamma$ and K -decay.

In reference [3] we reported on the observation of a small number of events with a high p_T isolated lepton or large P_T^{miss} . The number of events seen and their kinematical distribution was found not to be consistent with the assumption of W production. Table 7.2 presents an update which includes the electron data. Unfortunately no new candidates have appeared [1].

7.3.2 Heavy quark production

Heavy quarks have become an increasingly interesting part in the physics field opened up by HERA. In the QCD picture of electron proton interactions, charm and beauty production involves the coupling to gluons. With the statistical power reached in the data now, charm quarks have become a direct probe of the gluonic component of hadronic structure. Since their masses are large compared to the QCD parameter Λ_{QCD} , they set the hard scale which is necessary for the methods of perturbation theory to be applied. The production process is therefore also an important testing ground for perturbative QCD. On the experimental

Data set	e^+p at $\sqrt{s} = 300$ GeV	e^-p at $\sqrt{s} = 320$ GeV
Luminosity	36.5 pb^{-1} 1994-97 published [3]	5.1 pb^{-1} 1998-99 preliminary
e events found	1	0
e events expected	2.4 ± 0.5	0.37 ± 0.07
e events from W decay	1.7 ± 0.5	0.23 ± 0.07
μ events found	5	0
μ events expected	0.8 ± 0.2	0.14 ± 0.04
μ events from W decay	0.5 ± 0.1	0.09 ± 0.02

Table 7.2: High transverse momentum p_T lepton and missing transverse momentum p_T^{miss} events seen by the H1-detector. The selection requires $p_T^{\text{calo}} > 25$ GeV, $p_T^{\text{track}} > 10$ GeV and no closely other tracks.

side, the first observation of b production at HERA last year has created interest. The still preliminary result indicates an unexpectedly high cross section. An independent measurement – using lifetime information based on the new Silicon vertex detector – is of high importance and within reach.

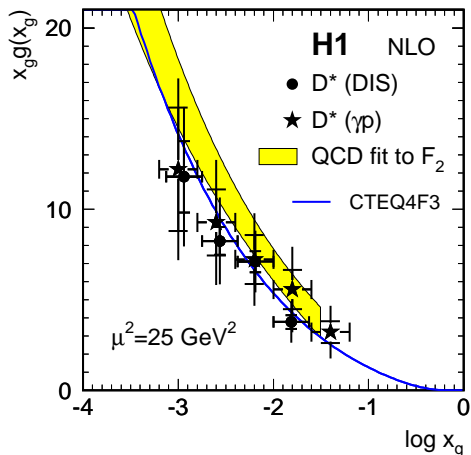


Figure 7.4: Gluon densities obtained from the two D^* analyses. The inner error bars represent the statistical and the outer the total error. The systematic error is a quadratic sum of all contributions, dominated by the theoretical uncertainty. Both results are compared to the result of the H1 QCD analysis of the inclusive F_2 measurement [25] at $\mu^2 = 25$ GeV² (light shaded band) and the CTEQ4F3 parameterization.

The measurement of the gluon density in the proton via charm production – observed through the fragmentation and decay chain $c \rightarrow D^{*+} \rightarrow D^0 \pi^+ \rightarrow (K^- \pi^+) \pi^+$ – in deep inelastic scattering (Thesis D. Müller [17]) has been discussed in our previous annual report. In 1998, a measurement following the same principle has been performed in photo-production. It strongly relies on differential cross section results (Thesis M. zur Nedden [18]) which demonstrate that the Next-to-Leading Order (NLO) QCD calculations used to extract the parton density information provide an adequate description of the data in the kinematic regime under consideration. The theses have been completed, and both results were published together [21]. Figure. 7.4 shows that they agree well with each other and also with the gluon density determined by H1 [25] from a QCD analysis of the scaling violations of the proton structure function F_2 . This amounts to an important verification of our understanding of the application of QCD and to a demonstration of the universality of the gluon distribution in the proton.

Pursuing these concepts further, charm production may also shed light on the dynamics of diffractive scattering. A fraction of about 10 % of the DIS events has a “rapidity gap”: in contrast to the general case the region surrounding the outgoing proton beam is void of any particles. This distinctively “diffractive” topology leads to an interpretation of the events in terms of the exchange of a color-less object, which may be identified with the Pomeron (\mathbb{P}) in the framework of hadron-hadron interaction phenomenology. HERA offers the possibility to study these phenomena in a perturbative regime and to investigate the partonic structure of the exchange, where charm production again singles out the gluonic component.

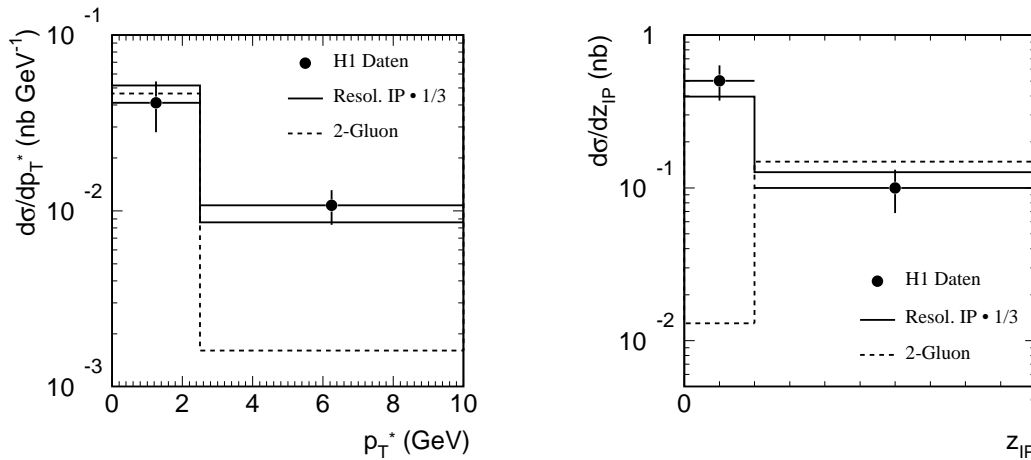


Figure 7.5: Differential cross sections for diffractive D^* production in DIS, with four-momentum transfer $Q^2 > 2 \text{ GeV}^2$ and $p_{\perp}(D^*) > 2$, as a function of p_{\perp} measured in the hadronic centre-of-mass frame, and of $z_{\mathbb{P}}$ which approximates the momentum fraction of the interacting parton as part of the exchanged object. The histograms represent the predictions of the “resolved Pomeron” model, scale by a factor 1/3, and the “two gluon” model.

The integrated luminosity accumulated in the years 1995-97 allows for the first time to take a step towards differential cross sections for diffractive D^* production (Thesis S. Hengstmann). In Figure 7.5 the data are compared to two different model predictions. In the “resolved Pomeron” model [27], the structure of the exchanged object is described in terms of quark and gluon densities which have been obtained from a fit to inclusive diffractive DIS data. In the “two gluon” model [28], the color-less exchange is realized in terms of two perturbative gluons, and cross sections are sensitive to the gluon density in the proton. The two approaches lead to remarkably different kinematic distributions; examples can be seen in Figure 7.5. p_{\perp}^* denotes the transverse momentum of the D^* meson in the hadronic centre-of-mass frame, and $z_{\mathbb{P}}$ is an observable correlated with the momentum fraction which the parton interacting with the $c\bar{c}$ pair holds as part of the exchanged object. In the “ $2g$ ” model, $z_{\mathbb{P}} = 1$ would hold if the partons could be directly observed. The data reveal that the “resolved \mathbb{P} ” approach gives a fair reproduction of the shape of the spectra, but fails in overall normalization. The “two gluon” model, on the other hand, matches the data at high $z_{\mathbb{P}}$, but a lack of higher order, low $z_{\mathbb{P}}$ contributions is apparent. The data thus provide valuable and rather distinctive indications for further refinement of the theoretical description.

Tagging heavy quark production with D^* mesons suffers from the low fragmentation and decay fraction of the preferred channel of 0.7% which is then further reduced by experimental efficiencies. Much higher tagging efficiencies can be obtained by making use of the long

lifetimes of c and b hadrons which can be measured with micro-vertex detectors. With its central silicon tracker (CST), H1 is the first experiment at HERA to be in the position to exploit these techniques. Fully commissioned in 1997, the CST is now being integrated into physics analyses. As an example of the first studies made, we show in Figure 7.6 the lifetime distribution of D^0 mesons originating from D^* decays. The lifetimes for each event have been obtained from a measurement of the decay length in the transverse detector plane - using the D^0 decay tracks measured in the CST - and from the the transverse momentum of the D^0 meson. The fitted curve is the convolution of a Gaussian resolution function - mainly reflecting the beam spot size - and an exponential decay law. It describes the gross features of the distribution well. Apart from developping the skills and understanding in dealing with the new detector, the motivation for the study is that contributions from beauty decays $B \rightarrow D^* X$ would give rise to excessively long reconstructed lifetimes, due to the additional B decay path. This may illustrate that the window to new physics opportunities is just now being opened.

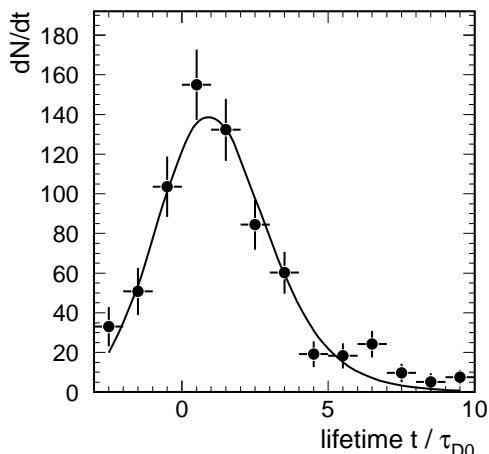


Figure 7.6: Distribution of D^0 meson lifetimes, calculated from the decay length measured with the CST, and the D^0 momentum, in units of the D^0 mean lifetime. The curve is a convolution of a resolution function and an exponential decay law.

References

- [1] *High Q^2 NC and CC results from H1*, V. Shekelyan, XXXIV. Rencontres de Moriond, on Electroweak Interactions and Unified Theories, Les Arcs, France, March 1999; available at http://www-h1.desy.de/h1/www/h1work/hip/results/high_q2_inclusive/.
- [2] *Measurement of Neutral and Charged Current Cross Sections in Positron Proton Collisions at Large Momentum Transfer*, C. Adloff et al. (H1-Collaboration), to be submitted to Eur. Phys. J. C.
- [3] *Observation of Events with an Isolated High Energy Lepton and Missing Transverse Momentum at HERA*, C. Adloff et al. (H1-Collaboration), Eur. Phys. J. **C5** (1998), 575.
- [4] *A Search for Leptoquark Bosons and Lepton Flavor Violation in e^+p collisions at HERA*, C. Adloff et al. (H1-Collaboration), submitted to Eur. Phys. J. C.
- [5] *Hadron Production in Diffractive Deep-Inelastic Scattering*, C. Adloff et al. (H1-Collaboration), Phys. Lett. **B428** (1998), 206.

- [6] *Diffractive Dijet Photoproduction at HERA*, C. Adloff et al. (H1-Collaboration), Eur. Phys. J. **C6** (1999), 421.
- [7] *Measurement of Leading Proton and Neutron Production in Deep Inelastic Scattering at HERA*, C. Adloff et al. (H1-Collaboration), Eur. Phys. J. **C6** (1999), 587.
- [8] *Differential (2+1) Jet Rates and Determination of α_s in Deep-Inelastic Scattering at HERA*, C. Adloff et al. (H1-Collaboration), Eur. Phys. J. **C5** (1998), 625.
- [9] *Multi-Jet Event Rates in Deep-Inelastic Scattering and Determination of the Strong Coupling Constant*, C. Adloff et al. (H1-Collaboration), Eur. Phys. J. **C6** (1999), 575.
- [10] *Forward Jet and Particle Production at HERA*, C. Adloff et al. (H1-Collaboration), Nucl. Phys. **B538** (1999), 2.
- [11] *Di-jet Rates in Deep-Inelastic Scattering at HERA*, C. Adloff et al. (H1-Collaboration), DESY 98 – 076, Eur. Phys. J. **C** (1999), in print.
- [12] *Measurement of Di-jet Cross Sections in Low Q^2 and the Extraction of an Effective Parton Density for the Virtual Photon*, C. Adloff et al. (H1-Collaboration), DESY 98 – 205, Eur. Phys. J. **C** (1999), in print.
- [13] *Measurement of Internal Jet Structure in Di-jet Production in Deep Inelastic Scattering at HERA*, C. Adloff et al. (H1-Collaboration), DESY 98 – 210, Nucl. Phys. **B** (1999), in print.
- [14] *Multiplicity Structure of the Hadronic Final State in Diffractive Deep-Inelastic Scattering at HERA*, C. Adloff et al. (H1-Collaboration), Eur. Phys. J. **C5** (1998), 439.
- [15] *Elastic Electroproduction of ρ Mesons at HERA*, C. Adloff et al. (H1-Collaboration), DESY 99 – 10, submitted to Eur. Phys. J. **C** (1999).
- [16] *Charmonium Production in Deep Inelastic Scattering at HERA*, C. Adloff et al. (H1-Collaboration), DESY 99 – 026, submitted to Eur. Phys. J. **C**.
- [17] *A Measurement of the Gluon Density in the Proton Based on Charm Production at HERA*, D. Müller, Thesis, Universität Zürich 1998.
- [18] *Photoproduction of Open Charm in ep -Collisions at HERA*, M. zur Nedden, Thesis, Universität Zürich 1998.
- [19] *Photoproduction of $\Psi(2s)$ Mesons at HERA*, C. Adloff et al. (H1-Collaboration), Phys. Lett. **B421** (1998), 385.
- [20] *Charged Particle Cross Sections in Photoproduction and Extraction of the Gluon Density in the Photon*, C. Adloff et al. (H1-Collaboration), DESY 98 – 148, Eur. Phys. J. **C** (1999), in print.
- [21] *Measurement of D^* Meson Cross Sections at HERA and Determination of the Gluon Density in the Proton*, C. Adloff et al. (H1-Collaboration), DESY 98 – 204, Nucl. Phys. **B** (1999), in print.
- [22] *ep physics beyond 1999*, H1 note H1-10/97-531, April 1998.
- [23] *H1 high luminosity upgrade 2000*, CIP and level 1 vertex trigger, M. Cuje et al., H1 note H1-01/98-539, January 1998.
- [24] C. Adloff et al. (H1-collaboration), Z. Phys. **C74** (1997), 191.
- [25] S. Aid et al. (H1 Collaboration), Nucl. Phys. **B470** (1996) 3.
- [26] W. Buchmüller, R. Rückl, and D. Wyler, Phys. Lett. **B191** (1987), 442.
- [27] H.Jung, Comput. Phys. Comm. 86 (1995) 147.
- [28] J. Bartels, H. Lotter, M. Wüsthoff, Phys. Lett. **B 379** (1996) 239; J. Bartels, C. Ewecz, H. Lotter, M. Wüsthoff, Phys. Lett. **B 386** (1996) 389.

7.4 Microstrip gas chambers

P. Robmann, S. Steiner, P. Truöl and T. Walter
in collaboration with the Universities of Heidelberg and Siegen

While there exists a reference design for the type of microstrip gas chamber (MSGC) which is to be used in the CMS central and forward/backward barrel tracker, the search for cheaper alternatives as well as designs with a more extended operation regime still continues actively. This was evident, when the forward/backward subgroup held one of their meetings in Zürich in November 1998.

The solution favored by most groups at the moment is a MSGC with a supplementary electron multiplier foil, termed GEM-MSGC (see last year's report [1]). This is also the type of chamber, which is being produced and installed for the inner tracker of the HERA-B experiment. We have designed masks for these chambers, controlled the quality of the substrates at produced industrially at IMT and started the design of the support structure for the chambers in the magnet.

In 1998 we also had two chamber test runs at PSI, one in July and another in October. A major part of the software for the data analysis of these runs was written in Zürich (in C^{++}), where we also analyse the data. The unfortunate conclusion from these runs, from the exposure of the chambers to an intense X-ray source in Heidelberg and to the HERA-B environment at DESY is, that a completely satisfactory solution for the inner tracker has not yet been found. Since the tests as well as the analysis are still in progress, only a few rather incomplete results can be given below.

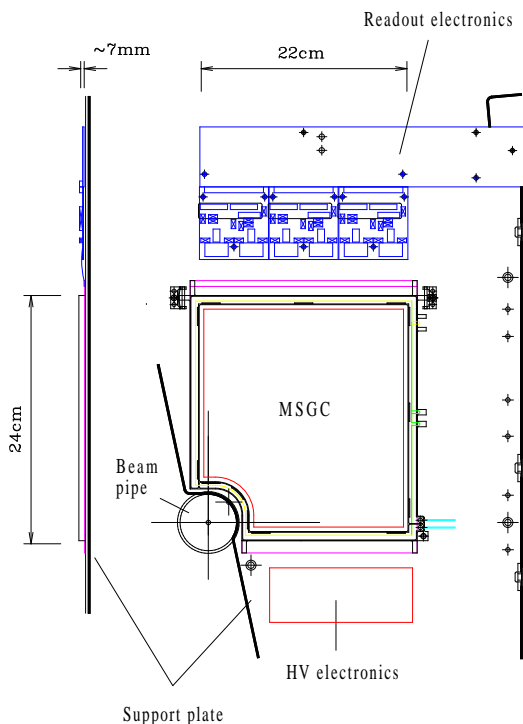


Figure 7.7: *HERA-B MSGC mounted on the support plate with the necessary readout and supply electronics.*

7.4.1 The GEM-MSGC detector for HERA-B

In Figure 7.7 the layout of a typical HERA-B MSGC is sketched. The chamber and the corresponding electronics, etc. are mounted on the support plate which is a compound of honey comb covered by a layer made out of carbon fibre on both sides.

The cover of the chamber consists of a 0.3 mm G10 plate (to ensure mechanical stability) and a 125 μm thick Kapton foil covered with 1 μm copper, which serves as the drift cathode. With a 3 mm drift gap the total chamber capacity is 200 pF. With a drift field in the range of 5.7 kV/cm we find a drift velocity of 52 mm/ μs for an Argon/DME (50/50) mixture. The GEM foil, which is produced in the CERN workshop, is mounted below the drift gap. This 50 μm thick Kapton foil is covered with 7 μm copper on each side. The 55 μm diameter holes in the Kapton are staggered with a pitch of 140 μm , and are surrounded by a 90 μm diameter hole in the copper. An electronically stabilized voltage of about 390 V is applied

between the upper and the lower surface of the GEM foil. Resistors of $2\text{ M}\Omega$ on each side decouple the large cable capacity from the GEM capacity, which was measured as 30 nF . We expect a visible gas gain of about 20 to 30 in the GEM, determined from the size of the pulses seen at the output of the preamplifier-shaper. The charge produced in the GEM foil is transferred by an electrical field of about 5.2 kV/cm through the transfer gap of 2.8 mm to the MSGC wafer. The wafer substrate consists of 0.4 mm AF45 glass, which is coated with a diamond-like layer at the Fraunhofer Institut for Surface Engineering and Thin Films, Braunschweig, Germany. The coating has a thickness of about $0.08\text{ }\mu\text{m}$ and a typical surface resistance of $10^{14}\text{ }\Omega/\text{square}$, about two orders of magnitude less than the bulk resistance of the glass. The electrode structure is produced with the lift-off technique by IMT in Greifensee, Switzerland. The production masks are manufactured from the layouts provided by us at IMT. The metallisation consists of a $0.5\text{ }\mu\text{m}$ thick, very soft gold layer on a $0.08\text{ }\mu\text{m}$ titanium which serves as the sticking layer to the coated substrate. For HERA-B three types of substrates are needed, types 1 and 2 have an active area of $220 \times 240\text{ mm}^2$ with 752 anodes (UZHHERA6, UZHHERA 5, substrate size $300 \times 300\text{ mm}^2$), and differ only in the size of the cutout near the beam pipe. The pitch is $300\text{ }\mu\text{m}$, the anodes are $10\text{ }\mu\text{m}$ wide and the gap is $60\text{ }\mu\text{m}$, resulting in $170\text{ }\mu\text{m}$ wide cathode strips. The active area of type 3 is $260 \times 265\text{ mm}^2$ with 756 anodes (UZHHERA7, substrate size $300 \times 325\text{ mm}^2$). Here the pitch is $350\text{ }\mu\text{m}$ and with the same anode and gap width as above the cathode strips are $220\text{ }\mu\text{m}$ wide. Sixteen cathodes are always connected together, which then form the 48 cathode groups. The layout for chamber type 2 was designed in 1997, for types 1 and 3 in 1998.

7.4.2 Substrate production and quality control at IMT

During the last year IMT produced about 200 substrates (see Figure 7.8), of which 135 type 2 and 58 type 3 are already accepted. The production of 40 type 1 substrates will finish by the end of April 1999.

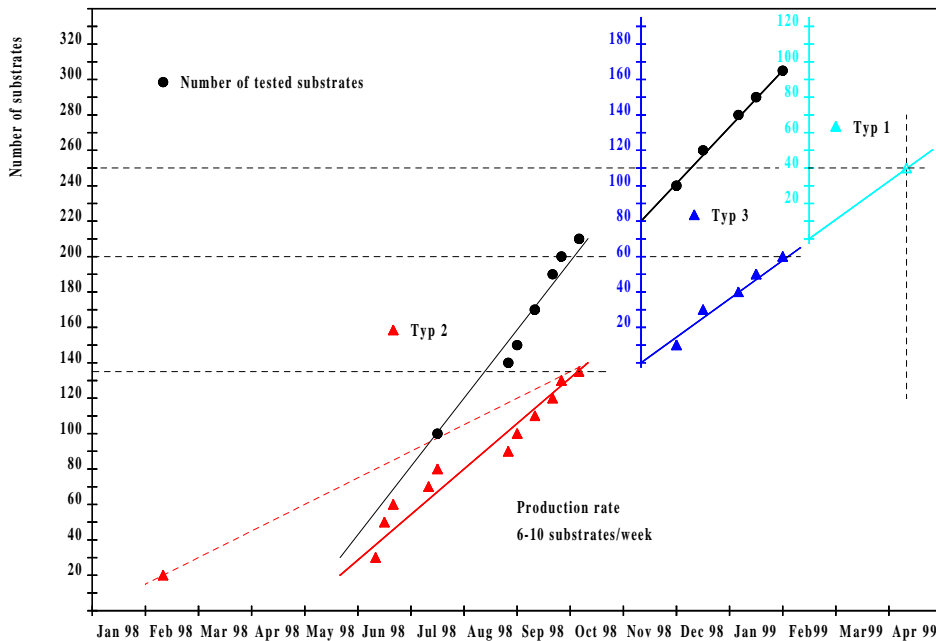


Figure 7.8: Number of substrates produced at IMT (Greifensee) during the last year. The dots show the number of tested substrates.

The quality of the substrate is controlled with the testing facility developed by us (see last year's report [1]). The setup is installed at IMT. This allows a fast feedback and guaranties a continous quality improvement. The dots in figure 7.8 show the number of tested substrates. Comparing this number with the number of accepted substrates shows a production yield of about 70%. An accepted detector substrate has to have less than 50 non-adjacent broken anodes and no shorts. Typically 15 or 2 % of the anodes are broken as Figure 7.9 indicates.

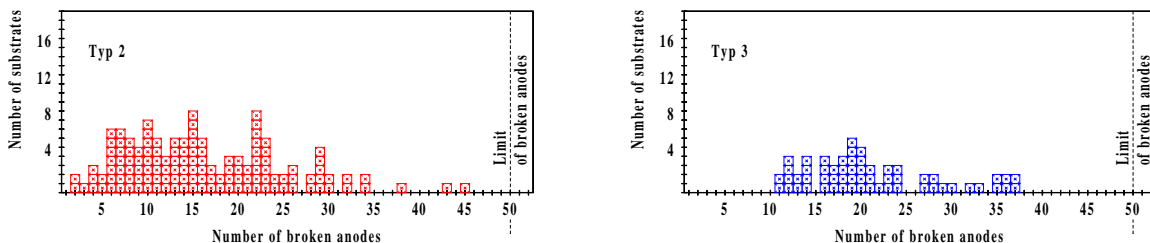


Figure 7.9: Number of broken anodes for the accepted substrates of type 2 and type 3.

7.4.3 MSGC tests at PSI

During the PSI test run in July for the first time a large GEM-MSGC with the fully pipelined readout system designed for the HERA-B experiment has been operated at high hadronic particle rates (see [2]). The system showed the expected performance with a relatively large gas amplification, which is not quantitatively understood yet. After subtracting correlated pickup signals and offset values channelwise the remaining noise is still somewhat higher than the expected thermal noise on the detector and input stage of the electronics. The correlation of the efficiency with additional occupancy due to noise shows that the operating conditions are realistic for a larger experiment, but the safety margin in signal amplitude is small (see Figure 7.10).

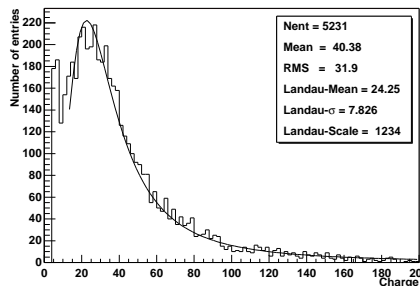


Figure 7.10: Measured charge, the curve shows a fitted Landau distribution.

In the October 1998 test run we operated a set of three detectors. This allows track reconstruction and the determination of efficiencies and spatial resolution. In Figure 7.11 the threshold dependence of the efficiency of the middle detector is plotted, when we are looking for tracks, which have a hit in the first and the last detector. In Figure 7.12 the residuals, i.e. the distance from the hit to the track, are plotted. The shift shows the missalignment of the setup of 120 μm .

After irradiation with the high rate proton beam at PSI we observed ageing of the GEM-MSGC detectors. The gas ageing manifests itself by deposits on the irradiated anodes. The deposits (Carbon and/or C-H-molecules) lead then to a reduction of the gas gain. Consequently the efficiency will also drop. Figures 7.13 and 7.14 show a comparison of an anode from a new substrate and an anode from a substrate, which was irradiated at PSI. Laboratory ageing tests indicate, that the deposits originate from polluted materials used in the

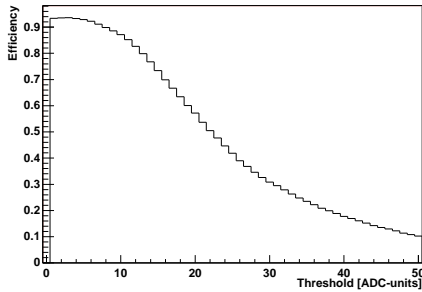


Figure 7.11: *Track finding efficiency depending on the threshold.*

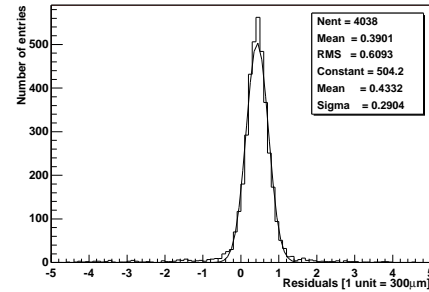


Figure 7.12: *Distribution of the residuals, the difference from the track to the measured hit.*

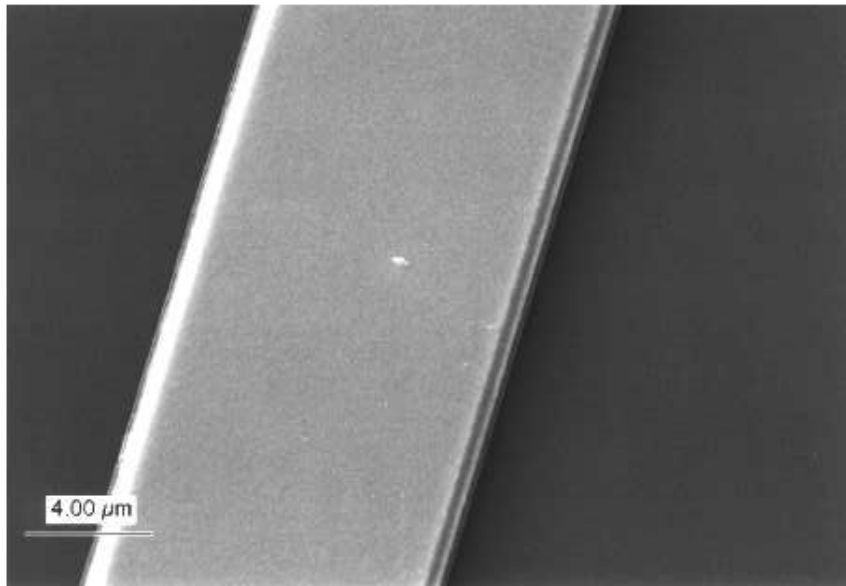


Figure 7.13: *REM picture of an Anode on a new substrate.*

detectors.

7.4.4 Status of the HERA-B experiment

The HERA-B experiment is part of the worldwide effort to understand the origin of the baryon-antibaryon asymmetry in the universe related to the small observed CP-violation in the neutral kaon system. The electroweak standard model, in which the physical states are related to the weak eigenstates through the quark mixing matrix incorporates CP-violation. The observed charge asymmetry in K_L^0 decay as well as the coexistence of K_L^0 decays into two and three pions are both consistent with the electroweak standard model, but can not yet taken as proof, that nature has taken this path. The standard model predicts larger asymmetries in the decays of neutral B -mesons, which is why most of the experimental effort is directed to this system. Three avenues are taken, using hadron colliders, using electron-positron colliders and directing the highest energy proton beams available onto fixed targets. The experiments BaBar and Belle at an high-intensity e^+e^- storage ring (SLAC B-factory) operating at a center of mass energy of 10.5 GeV and producing $B_d\bar{B}_d$ pairs are starting this year. The 1 TeV $\bar{p}p$ collider at Fermilab with its two experiments D0 and CDF resumes

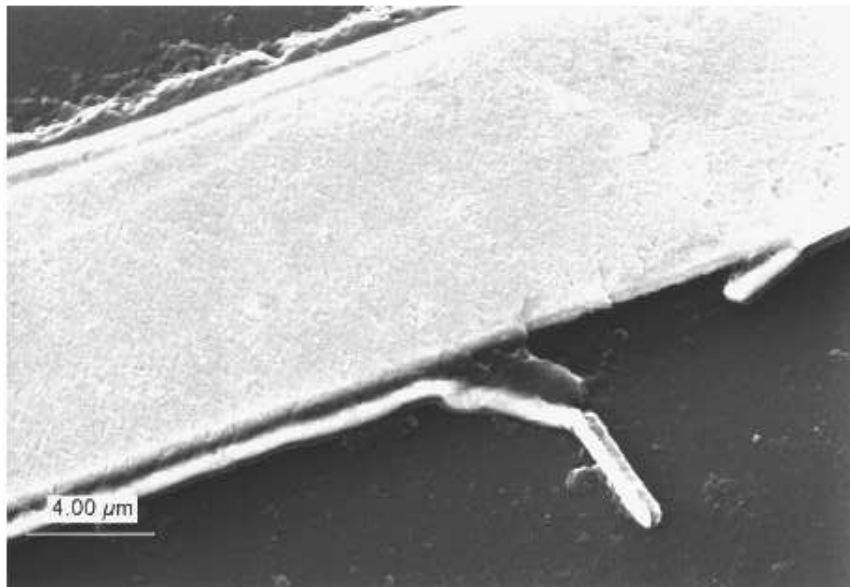


Figure 7.14: *REM picture of an anode, irradiated during the test at PSI in October 1998.*

operation next year with increased luminosity. It is with these four experiments, which the HERA-B experiment competes.

Effects to further scrutinize the information from the K^0 system continue. The combined results from precision experiments at CERN and Fermilab comparing the charged and neutral two pion decays of the K_L^0 and measuring the parameter ϵ'/ϵ [3] indicate a direct CP-violation in the decay, not only induced through quark mixing. Future experiments at Brookhaven and Fermilab propose to measure the extremely rare decay $K_L^0 \rightarrow \pi^0 \nu \bar{\nu}$.

At HERA-B the tails of the coasting 920 GeV proton beam strike an internal wire target producing 10^9 B -mesons per year similar to Fermilab, and about 10 times more than at the B -factories. Since the B -production cross section rises strongly with energy, ultimately, at the 7 TeV pp-collider LHC typically three orders of magnitude in rate can be gained, which is why B -physics plays a central role in the CMS-program, too, as we indicated in previous annual reports. The disadvantage of hadronic production is, that only one in 10^6 interaction produces a B -meson pair, i. e. 10^{15} interactions have to occur within the detector to produce 10^9 B -mesons, with 1000 golden decays $B^0 \rightarrow J/\Psi K_S^0$; $J/\Psi \rightarrow e^+e^-$, $\mu^+\mu^-$; $K_S^0 \rightarrow \pi^+\pi^-$ (see Figure 7.15) among them detected. The HERA-B detector (see Figure 7.16) has to be able to select one interesting decay in 10^{12} interactions, withstand an event rate of 40 MHz and a particle density of $10^{-5} R^{-1}/\text{mm}^2\text{s}$, where R [cm] is the perpendicular distance to the beam axis.

At the beginning of 1999 only a fraction of the HERA-B detector was installed yet [4, 5]. One complete station and three half stations of a total of eight of the vertex detector are available. The electromagnetic calorimeter has all tubes installed, the RICH is operating and a major part of the muon system is ready, too. For the outer tracker a revision of construction materials and techniques based on extensive beam tests has led to the start of module production; a small number of modules is being tested within the HERA-B environment. The inner tracker is completely missing for the reasons discussed above. Plans for the short shutdown in May 1999 include the completion of the vertex detector and the muon system, and instal one third of both outer and inner tracker. Whether the latter goal can be reached is doubtful in view of the MSGC ageing problems which are still under investigation. The

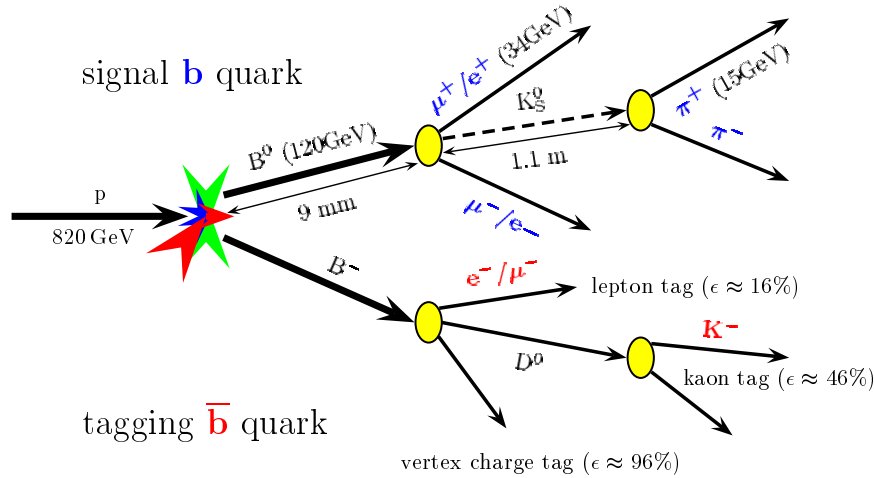


Figure 7.15: The *golden* decay $B^0 \rightarrow J/\Psi K_S^0; J/\Psi \rightarrow e^+e^-, \mu^+\mu^-; K_S^0 \rightarrow \pi^+\pi^-$. The following probabilities apply: 1) production target $\sigma_{B^0\bar{B}^0}/\sigma_{\text{inel}} \approx 8 \times 10^{-7}$; 2) branching ratio product from decay vertices $5 \times 10^{-4} \cdot 0.12 \cdot 0.69$ 3) trigger, track and vertex reconstruction efficiency 0.17 4) tagging 0.07.

detector systems which are available at the moment however allow a parallel commissioning of the readout and trigger electronic and data acquisition system. The HELIX chip can in its present version (HELIX2.2) only be used for the silicon vertex detector and not the inner tracker because the trigger outputs fail. The next iteration (HELIX3.0) is presently being tested, but a series will not be ready for the 1999 installation. The readout electronic for RICH, outer tracker and the muon system is completed. The first level trigger is derived so far only from part of the calorimeter, but allowed commissioning of the final DAQ system and calibration of those subsystems, which are operative. It is foreseen to measure the B meson production cross section early this year, and hoped to see the first few example of the J/Ψ decay chain early next year.

The merits of the different CP violation experiments in the B system are usually evaluated by comparing the uncertainty with which the angles of the unitarity triangle (see Figure 7.17) can be measured. If the Wolfenstein parametrisation of the quark-mixing matrix is used as

$$\begin{pmatrix} V_{ud} & V_{us} & V_{ub} \\ V_{cd} & V_{cs} & V_{cb} \\ V_{td} & V_{ts} & V_{tb} \end{pmatrix} = \begin{pmatrix} 1 - \frac{1}{2}\lambda^2 & \lambda & A\lambda^3(\rho - i\eta) \\ -\lambda & 1 - \frac{1}{2}\lambda^2 & A\lambda^2 \\ A\lambda^3(1 - \rho - i\eta) & -A\lambda^2 & 1 \end{pmatrix},$$

the unitarity triangle is the geometrical representation of the condition

$$V_{ud}V_{ub}^* + V_{cd}V_{cb}^* + V_{td}V_{tb}^* = 0.$$

The complex phase η of the matrix is directly related to CP violation.

The *golden* decay mode is favored, because hadronic uncertainties are small, the CP-asymmetry and the two leptons from J/Ψ decay offer good trigger conditions. If the initial flavor (b or \bar{b}) is tagged with the second B meson (see Figure 7.15) the time integrated $B_0\bar{B}_0$ asymmetry affords a measurement of $\sin 2\beta$ with an accuracy of about 0.13 comparable to CDF, and not quite as good as BaBar and Belle. A similar uncertainty can be expected for $\sin 2\alpha$ from $B^0 \rightarrow \pi^+\pi^-$, but here the interpretation and experimental conditions are less clearcut.

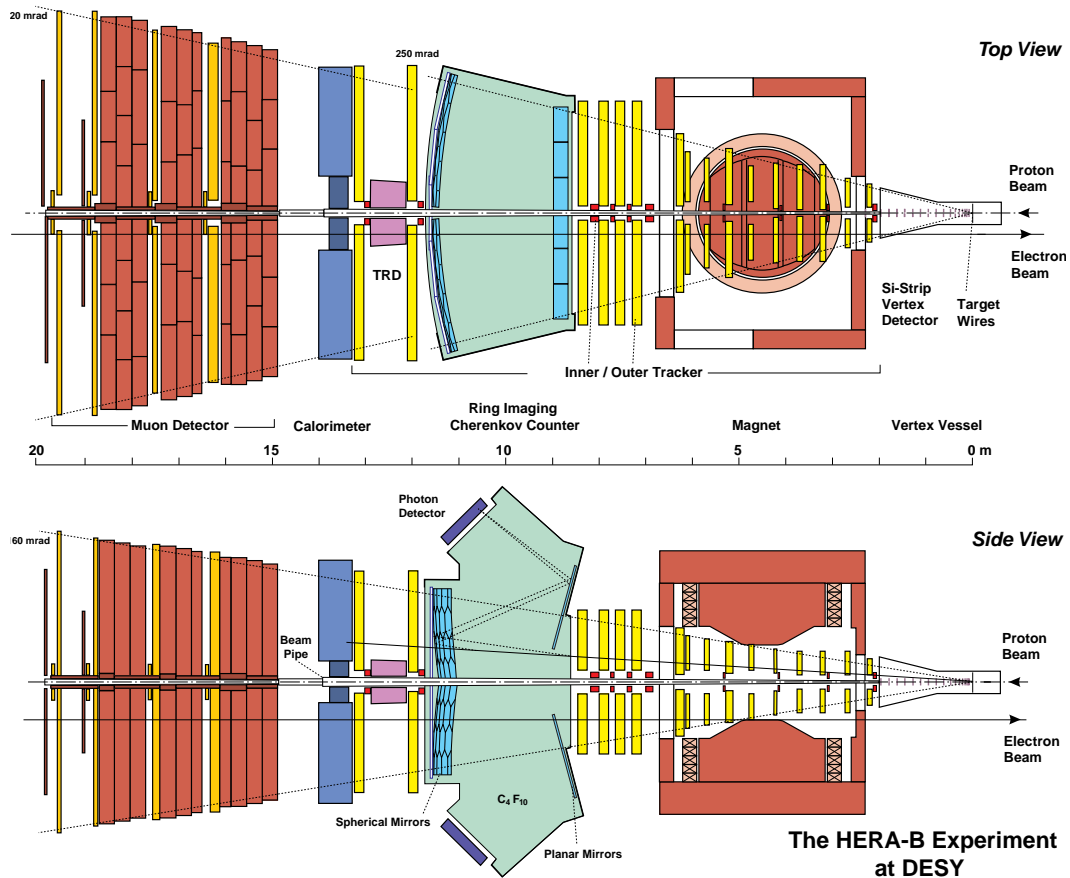


Figure 7.16: The HERA-B detector: magnet bending power 2 Tm; inner tracker ($R < 20$ cm) with MSGC-GEM; outer tracker with 5 and 10 mm drift cells; electromagnetic calorimeter with W/Pb scintillator shaslik; muon system with tube, pad and gas pixel chambers; vertex detector with $12 \mu\text{m}$ resolution Si strips; ring imaging Čerenkov counter (RICH) with multianode photomultipliers.

If the precise measurements of the B_d^0 oscillation frequency, the limit on the B_s^0 oscillation frequency, the improved determination of the mass of the top quark, and of $|V_{ub}|$ are used as input [6] one arrives at the limits shown in Figure 7.17, which correspond to $\sin 2\alpha = 0.06 \pm 0.40$, $\sin 2\beta = 0.75 \pm 0.09$, $\rho = 0.160 \pm 0.085$ and $\eta = 0.381 \pm 0.060$. This analysis, though performed within and consistent with the standard model, rests on the assumption, that the theoretical uncertainties of a number of non-perturbative hadronic quantities, have been properly assessed, which is why it does not make the new generation experiments superfluous.

The HERA-B experiment therefore still very well justified. It may be seen as a prototype and pioneering experiment, from a physics as well as a technology point of view for the considerably more ambitious LHCb and CMS projects in this area.

References

- [1] Physik-Institut, Universität Zürich, Annual Report 1997/98, available at <http://www.physik.unizh.ch/jb/1998/kap4.ps>
- [2] *Operation of a large GEM-MSGC detector in a high intensity hadronic test beam using fully pipelined readout electronics*, HERA-B int. note 98-149, available at <http://www->

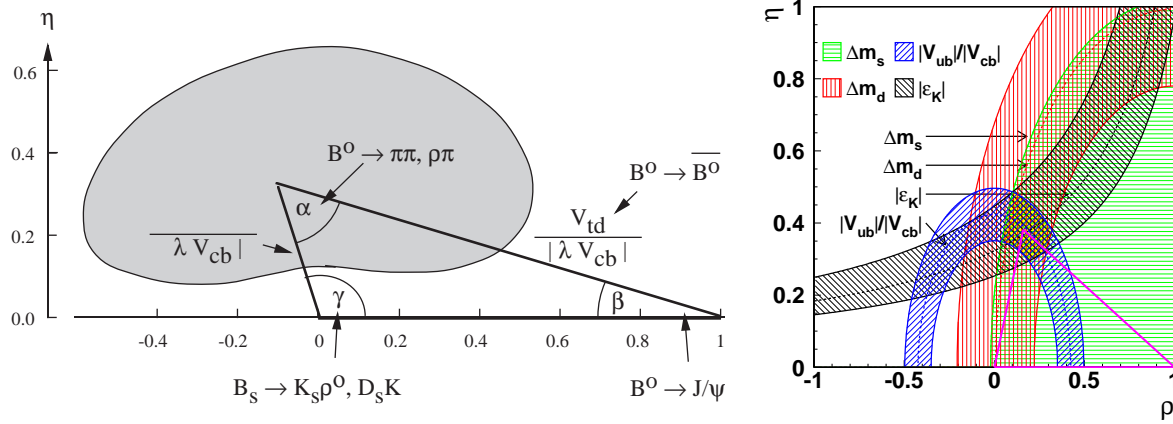


Figure 7.17: The unitarity triangle in the Wolfenstein parametrisation of the Cabbibo-Kobayashi-Maskawa mixing matrix. Left: the different B-meson decay channels which contribute to the determination of the angles and sides of the unitarity triangle to be studied in the HERA-B experiment. The shaded area indicates the uncertainty in the position of the tip of the triangle at the time of the HERA-B proposal. Right: summary of present knowledge on the triangle using K-decay and (indirect) information from LEP experiments [6]

hera-b.desy.de/notes/98/98-149.ps

- [3] *First ϵ'/ϵ result from the KTeV experiment*, P. Shawhan, Fermilab (February 1999), available at <http://fnphyx-www.fnal.gov/experiments/ktev/epsprime/epsprime.html>
- [4] *The HERA-B experiment*, C. Padilla, 26th Int. Meet. on Fundamental Physics, Illa da Toxa, Pontevedra (Spain) (June 199) available at <ftp://ftp.desy.de/pub/herab/talks/Winter-Meeting/toja.ps>
- [5] HERA-B status report, January 1999, R. Eckmann, available at ftp://ftp.desy.de/pub/herab/talks/prctalk/prc_Jan99.PDF
- [6] *Indirect measurement of the vertex and the angles of the unitarity triangle*, S. Mele, preprint CERN-EP/98-133, (hep-ph/9810333)

8 Neutrino Masses and Mixing

E. Holzschuh, W. Kündig, L. Palermo, and P. Wenk

The masses of the neutrinos are known to be small when compared with the masses of their charged partners. How small is unknown, however. If the neutrino masses are nonzero, it is considered likely that there is also neutrino mixing. In our project we are using β -spectroscopy to investigate these questions. Mixing would mean in this case that the electron neutrino, emitted in β -decay, is described by a superposition of states with two or more different masses m_i . The signature would be a characteristic 'kink' in an otherwise smooth β -spectrum at an energy $E_0 - m_i$, where E_0 is the endpoint energy for zero neutrino mass.

The objective of the project is a systematic search with high sensitivity in the β -decay of the isotopes ^{63}Ni and ^{35}S for neutrino masses up to 100 keV. The project is now nearly completed. The last measurements were performed in spring 1998. Thereafter we had to disassemble the experiment for the reason that on this location at the Paul-Scherrer-Institute the new Swiss-Light-Source is being built.

A detailed description of the β -spectrometer, some auxiliary experiments and simulations of electron scattering in the spectrometer have been published [1]. The measurements with ^{63}Ni formed the basis of P. Wenk's dissertation [2] and the final results have been published [3]. A new method for preparing thin ^{35}S -sources [4], the measurements with ^{35}S , and preliminary results are described in the dissertation of L. Palermo [5]. The final results should be ready for publication shortly.

8.1 Calibration

The ^{63}Ni -source contained a small contamination with ^{109}Cd and the K conversion line showed up as a small peak in the measured ^{63}Ni spectrum at $E = 62.25$ keV, that is below the endpoint $E_0 = 67$ keV. The peak could be corrected in the analysis and was not a serious problem. As the L conversion lines are well above E_0 , the ^{109}Cd contamination could be used to test the calibration and the computed resolution of the spectrometer. Figure 8.1

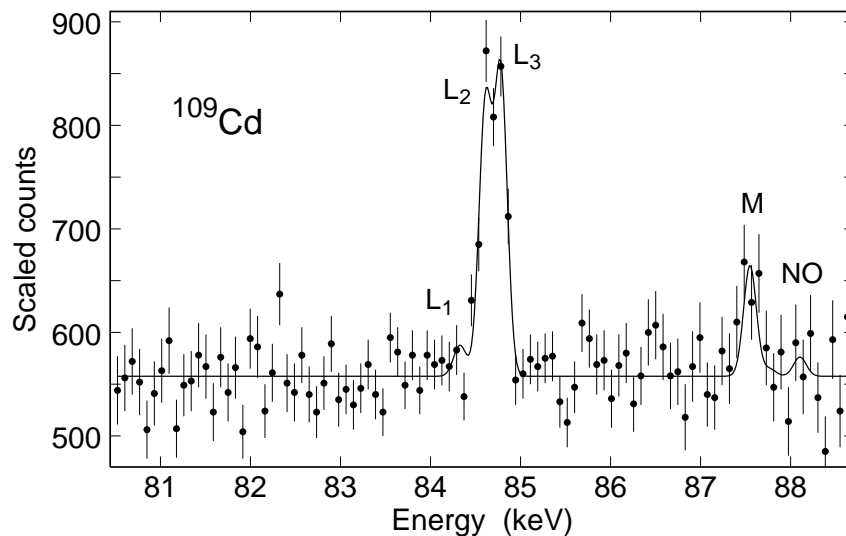


Figure 8.1: Measured conversion line spectrum of ^{109}Cd contamination (points) and best fit (line).

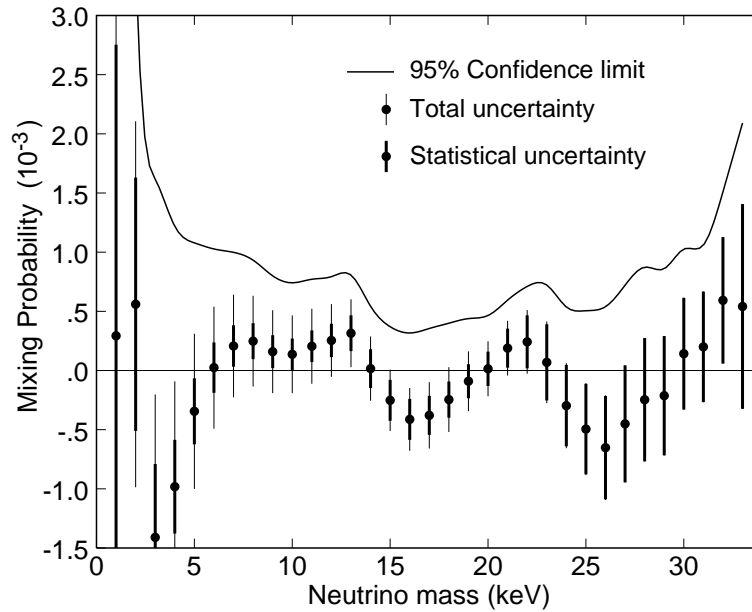


Figure 8.2: *Best fit (points) of the mixing probability as a function of assumed neutrino mass, from the ^{63}Ni data. The error bars combine statistical and systematic errors. The solid line is an upper limit at 95 % confidence.*

shows the data of a measurement over an energy range containing the L and M lines. The L_2 and L_3 lines are clearly seen. The M lines are also significant but not resolved. The data were fitted assuming the line shapes to be given by the computed spectrometer resolution function for this setting. The relative line intensities and the energy differences of the lines were taken from the literature [6]. A good fit was obtained, showed the reliability of the computed spectrometer resolution.

8.2 Results for ^{63}Ni

The ^{63}Ni β -spectrum was measured over an energy range from about 33 to 68 keV. The total number of counts in the data set was 5.2×10^9 . Neutrino mixing was search for assuming the mass of a heavy neutrino in the range up to 33 keV. The fitted mixing probability is plotted in figure 8.2. The error bars combine statistical and systematic errors. As can be seen, there is no indication for neutrino mixing. The solid line in figure 8.2 is an upper limit at 95 % confidence.

8.3 Results for ^{35}S

The ^{35}S source, prepared as described in Ref. [4], had an initial activity of 5.3 mCi and was supported by a thin (2000 Å) foil of Kapton. The β -spectrum of ^{35}S was measured from 45 keV to 170 keV (endpoint of ^{35}S is $E_0 = 167$ keV). This range was divided in five overlapping regions which were measured separately, starting at high energy to avoid too large counting rates. The total number of counts is 3×10^{10} in the complete data set.

Preliminary results from about half of the available ^{35}S data is shown in figure 8.3. The analysis is not complete, however, for the following reason. During the measurements, the thin support foil of the ^{35}S source broke and had to be repaired as there was no time available to make a new source. The repair parts had necessarily a mass large compared with the thin

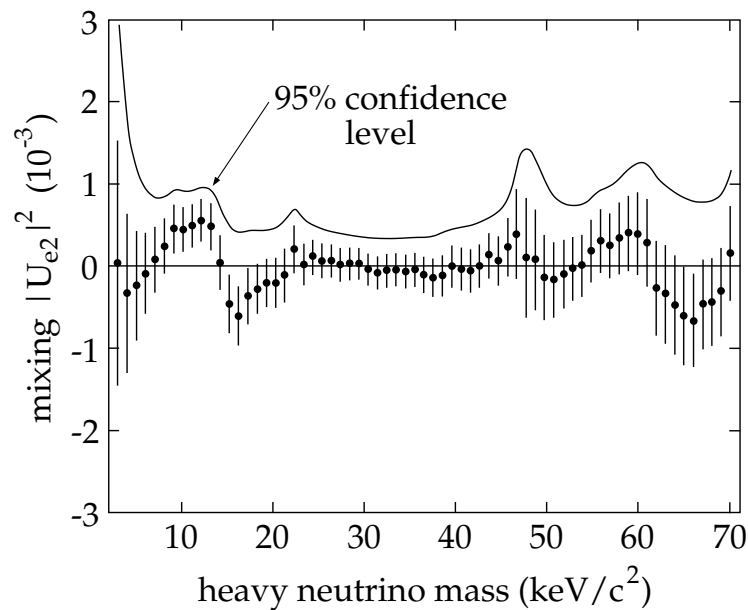


Figure 8.3: Preliminary results from a part of the ^{35}S data. Plotted is the best fit (points) of the mixing probability as a function of assumed neutrino mass. The error bars combine statistical and systematic errors. The solid line is an upper limit at 95 % confidence.

foil and thus scattered a significant number of electrons into the acceptance angle of the spectrometer. We are confident that an appropriate correction can be computed by Monte Carlo simulation.

8.4 Conclusion

The measurements have been successfully completed. The remaining results will be published shortly.

References

- [1] E. Holzschuh, W. Kündig, L. Palermo, H. Stüssi, and P. Wenk
Nucl. Inst. Meth. A **423**, 52 (1999).
- [2] P. Wenk, Dissertation, Uni. Zürich 1997.
- [3] E. Holzschuh, W. Kündig, L. Palermo, H. Stüssi, and P. Wenk
Phys. Lett. B, in print.
- [4] L. Palermo, E. Holzschuh, W. Kündig, P. Wenk, and R. Alberto
Nucl. Inst. Meth. A **423**, 337 (1999)
- [5] L. Palermo, Dissertation, Uni. Zürich 1998.
- [6] C.M. Lederer *et al*, Table of Isotopes, John Wiley, New York, 1978.

9 Measurement of the gravitational constant G

F. Nolting, S. Schlamminger, J. Schurr, E. Holzschuh, and W. Kündig

The gravitational constant G is the least accurately known fundamental constant of nature. The value presently recommended by CODATA¹ with an uncertainty of 128 ppm was measured by Luther and Towler [1] in 1982.

The goal of our experiment is a measurement of G with an uncertainty ten times smaller than at present. The experiment uses a beam balance to measure gravitational forces and has become feasible due to recent progress in the construction of beam balances with extremely high sensitivity. The principle of the experiment will be explained in the following section.

The experiment is set up and running. A first result for G with an uncertainty of 230 ppm was published recently [2]. F. Nolting completed his dissertation and obtained a value $G = (6.6749 \pm 0.0014) \times 10^{-11} \text{ m}^3 \text{ kg}^{-1} \text{ s}^{-2}$ (relative uncertainty 220 ppm). His result is completely dominated by systematics and the statistical error with 10 ppm is comparatively small.

During the last year we were mainly occupied with improvements of the experiment and with investigations of systematic uncertainties. These will briefly be described in this annual report.

9.1 The principle of the experiment

The experiment has been set up in a 4.8 m deep pit at the Paul-Scherrer-Institute. A schematic view is shown in figure 9.1. The essential components of the set-up are a single-pan beam balance, two test masses and two large field masses. The test masses (1 kg each) are suspended with thin tungsten wires and alternately connected to the balance. The difference of their weights is measured with high precision and taken as the signal. The balance and the test masses are inside a vacuum system. The field masses are cylindrical in shape and have a central bore such that the test masses can pass through. By moving the field masses between the two positions shown, their gravitational force on the test masses changes the signal. From the difference of the signal for the two states and from known values for the masses, densities, and distances, the gravitational constant G can be computed.

There are several features which make this principle of measurement very promising. The test masses are placed at positions where the gravitational force of the field masses has a local extremum. Therefore the relative position of the masses is quite uncritical. The value of G is computed from a double difference and many disturbing forces and drift effects cancel in the result. The field masses are vessels made of stainless steel with a volume of 500 l each. They can be filled with a liquid, either water or mercury. Compared with solids, a liquid is much to be preferred. This is because the density of a liquid is homogeneous, provided its temperature is homogeneous and this can be measured. The effect of compressibility is negligible. The effect of the vessel walls can be measured with empty vessels and subtracted if necessary.

9.2 Measurements with mercury

During most of 1998 the experiment was in operation and measurements with mercury filled vessels were performed. The measurements were frequently interrupted and various changes in the set-up were made to investigate systematic effects. The measured signal amplitude is plotted in figure 9.2. The error bars are statistical standard deviations with a typical value of 20 ng. During March and October the vacuum system was vented to fix problems. Such

¹The Committee on Data for Science and Technology of the International Council of Scientific Unions

operations are big disturbances as the system needs a rather long time until the residual gas pressure reaches a stable equilibrium value. Although still not clear, gas pressure effects might be one possible explanation for the systematic difference between the first set of data (January, February) and the remaining data.

Initially, the vessels were moved periodically with a period of about eight hours. To investigate whether periodic external disturbances (day–night or weekly) interfere with the measurement period, measurements were performed where the time interval between vessel movements were chosen at random. No significant effect was observed.

To investigate a possible nonlinearity of the balance response, additional loads were placed on the pan of the balance. Such loads should cancel precisely in the first difference which, however, seems not to be the case. This effect is expected to be smaller with the modified balance (see below).

9.3 Improvements of the experiment

Various improvements of the experiment have been made during the last year, mainly aimed at an increased stability and a higher resolution of the balance.

The balance was supplied by Mettler Toledo. The commercial version has a large measuring range, unnecessary for our purpose. To increase the resolution and to reduce noise, the range was originally set to 20 g and recently further reduced to 4 g. The flexure-strips, supporting the beam of the balance, were replaced by thinner ones. The result of these modifications can be seen in figure 9.3, showing histograms of the reproducibility, defined here as the standard deviation of 22 measured test mass differences. Before (left), the average was 360 ng and after the modification (right), its value decreased to 220 ng. This is not as good as we had hoped. There are indications that a significant part of the noise is caused by numerical rounding errors. This would seem to be a simple problem to correct, but it requires access to the internal software of the balance, which we do not have at present. Noise, external to the balance, is certainly also present and needs further investigations.

To monitor the positions of the vessels, a precision measuring system was installed. It has a resolution of $0.5\ \mu\text{m}$, which is quite sufficient.

With the present set-up, drifts due to changing temperature, residual gas pressure, etc., are quite large. Due to the double difference, these should cancel. However, this does not seem to be precisely the case and extra noise is induced, in an indirect way, by a changing temperature. Preparations have been started to install a better temperature controlling system and to improve the vacuum.

Acknowledgement

We thank the PSI for its hospitality, Mettler Toledo, especially M. Baumeler, for the high precision balance and the calibration of various standard weights. The experiment was supported by the Swiss National Science Foundation and the Scientific Research Foundation of the University of Zürich.

References

- [1] G.G. Luther and W.R. Towler, *Phys. Rev. Lett.* 48, 121 (1982).
- [2] J. Schurr, F. Nolting, and W. Kündig, *Phy. Rev. Lett.* 80, 1142 (1998).
- [3] F. Nolting, Dissertation, Uni. Zürich 1998.

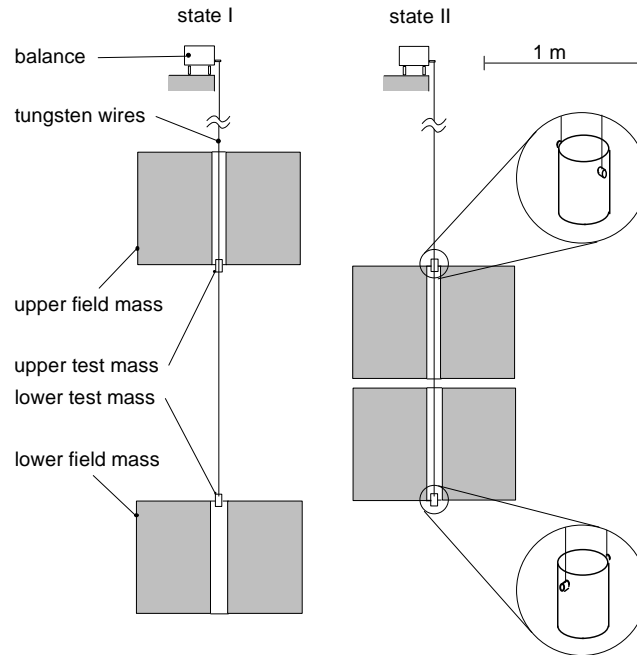


Figure 9.1: Schematic view of the experiment to measure the gravitational constant. See main text for explanation.

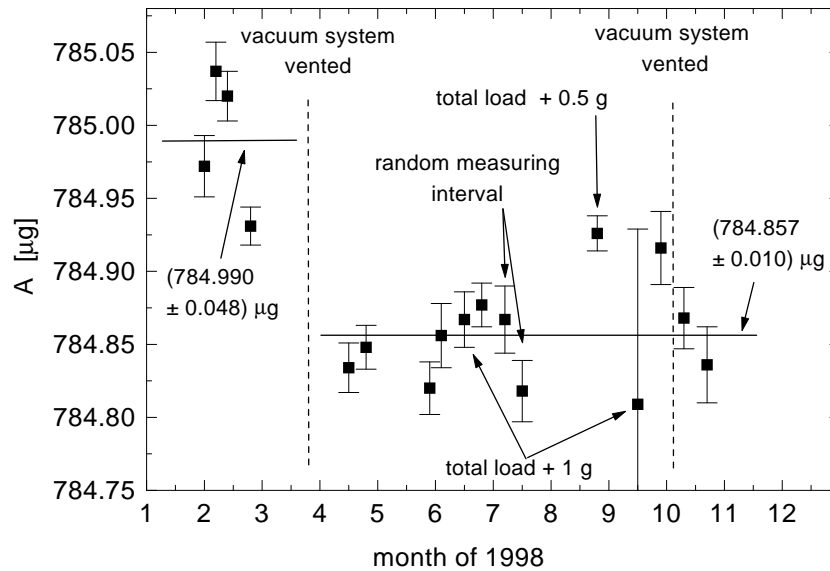


Figure 9.2: Signal amplitude as measured during 1998 with mercury filled vessels. The error bars are statistical standard deviations. Various changes of the measurement and operations performed are indicated. There are obvious systematic deviations which are presently not well understood.

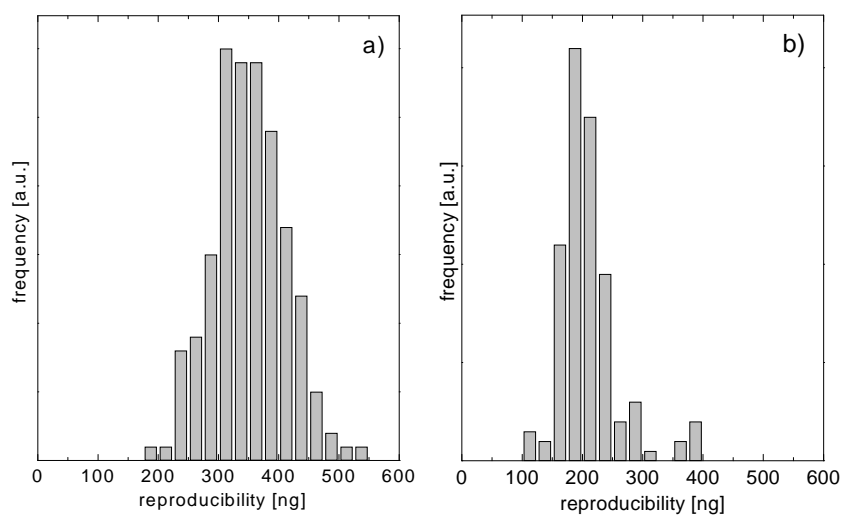


Figure 9.3: *Histograms of the reproducibility of the balance before the modification (left) and after (right).*

Part II

Condensed Matter Physics

There are three solid state physics groups in the department. The main research topics include high-temperature superconductivity, fast ion conductivity, and physics at high-pressure, as well as surface physics and the nanosciences. The research groups profit from a variety of first class equipment for some of the major experimental methods in these fields: nuclear magnetic and quadrupole resonance (NMR/NQR) including a diamond-anvil-cell for high-pressure studies, electron spin resonance (ESR), superconducting quantum interference device (SQUID) and torque magnetometry, angle-resolved X-ray and UV photoelectron spectroscopy (XPS/UPS), laser spectroscopy, scanning tunneling and atomic force microscopy (STM/AFM), as well as muon spin rotation at the Paul Scherrer Institute (PSI) and neutron scattering at the Institute Max von Laue-Paul Langevin in Grenoble (ILL, France). The research activities will also make use of the recently commissioned spallation neutron source (SINQ) at PSI, and of the synchrotron radiation source (SLS, commissioning 2001), where our department is actively involved in the planning of a UV surface science beamline.

A group of theoreticians in computational physics supports the above mentioned experimental groups. The mainly numerical work on high-speed computers comprises investigations such as the microscopic electronic structure of high-temperature superconductors including a diamond-anvil-cell for high-pressure studies and quantum Monte Carlo simulations of antiferro-magnetic structures. In addition the group collaborated with the Institute of Physical Chemistry, the University Hospital and the Department of Neurology.

All research groups enjoy the benefits of national and international collaborations, the most important of which are with ETH Zürich, University of Fribourg, IBM Rüschlikon, PSI at Villigen and the Sincrotrone Trieste (Italy).

Part II of this Annual Report presents motivations and results on the following projects:

- NMR/NQR Spectroscopy
- Magnetic Properties of Superconductors
- Surface Physics
- Spontaneous Ordering in AlGaAs
- Computer Assisted Physics.

10 NMR/NQR Spectroscopy

D. Brinkmann, S. Berger, M. Mali, R. Pozzi, F. Raffa, J. Roos, A. Suter, and A. Zavidonov .
Diploma students: M. Foglia, U. Lehmann, J. Plaz.

Guests: Dr. M. Igarashi, Gunma College of Technology, Gunma (Japan), till September 1998;
Prof. M. Itoh, Chiba University (Japan), April - August 1998; Dr. I.A. Larionov, Kazan
State University (Russia), since October 1998; I. Eremin, Kazan State University (Russia),
December 1998; Prof. K.N. Shrivastava, University of Hyderabad (India), February 1999.

This is the last Annual Report of the Physics Institute's NMR/NQR group in its present constitution. The 1998/1999 period has been dominated by all Ph.D. students finishing their theses and writing their final research papers, and the diploma students taking their final examinations. As in previous years, we have employed NMR/NQR techniques to probe, at a *microscopic* level, advanced materials like high-temperature superconductors, their antiferromagnetic parent compounds, and superionic conductors. One of the special techniques has been high-pressure NMR/NQR. Our major recent results will be summarized below.

10.1 Colloquium on *MAGNETIC RESONANCE IN HIGH- T_c SUPERCONDUCTORS*

After 12 years of ever increasing magnetic resonance activity in the field of high- T_c superconductors, we thought that a gathering of people involved in this research is appropriate and useful. We organized a small, well-focused meeting (in the spirit of our 1991 Colloque AMPERE with a similar title) which provided a general overview of the present state of the art of NMR, NQR, and EPR studies in high-temperature superconductors. Or in simple words: "What have we learnt so far about high- T_c superconductors from magnetic resonance studies?" The meeting also marked the end of our superconductor research of more than one decade.

The Colloquium took place in Engelberg from 17 through 22 January 1999 and it consisted of oral presentations (both invited and contributed) and private discussion. The meeting had been attended by about 35 scientists, many of them from abroad. We were pleased to see that the participants regarded the Colloquium as highly successful and very stimulating.

10.2 High-temperature superconductors

The topics of this project are central issues in this field of research and are all dealing with Y-Ba-Cu-O superconductors: the isotope effect of the spin gap, the inter-plane electronic spin polarization transfer in the superconducting state, the spin and charge dynamics in Cu-O chains combined with a theoretical study of the magnetic properties of these chains, and the cluster formation of chain oxygen vacancies and its relation to vortices.

10.2.1 Isotope effect of the spin gap

The work on the isotope effect of the spin gap has now been published [1]. We have shown by high-precision ^{63}Cu NQR spin-lattice relaxation experiments that the spin gap as characterized by the temperature T^* [where the relaxation rate per Kelvin reaches its maximum], is isotope dependent with an isotope exponent $\alpha_{T^*} = 0.061(8)$ which agrees quite well with

the corresponding exponent $\alpha_{T_c} = 0.056(12)$ for T_c as determined by SQUID magnetization measurements. This fact seems to confirm the growing evidence for a common origin of the superconductivity and the pseudo gaps. Finally, a possible relation between the opening of the spin gap and a CDW transition has been discussed.

On the other side, a quantitative prediction of an isotope dependence of the pseudo gap had been made within the charge-density wave (CDW) scenario; an isotope exponent $\alpha_{T_{\text{CDW}}} = 0.028$ has been calculated which is roughly a factor of 2 smaller than the experimental value. It is important to stress that according to this model, $\alpha_{T_{\text{CDW}}}$ and α_{T^*} do not need to be identical. However, the result that both parameters are of the same order, is consistent with a possible relation between a CDW transition and the opening of the spin gap.

The group of Williams *et al.* [2] had claimed the absence of an isotope effect on the spin gap. After our paper has appeared, Williams *et al.* now report that their data also favor the isotope effect.

10.2.2 Spin and charge dynamics in the Cu–O chains of $\text{YBa}_2\text{Cu}_4\text{O}_8$

There is an increasing interest in the physics of hole-doped Cu–O chains, as they may play an essential role in the normal and superconducting states of the superconductors $\text{YBa}_2\text{Cu}_3\text{O}_7$ and $\text{YBa}_2\text{Cu}_4\text{O}_8$. We therefore have continued our study of $\text{YBa}_2\text{Cu}_4\text{O}_8$ by performing NQR-NMR experiments with its chain copper and apex oxygen [3].

Above T_c , the temperature dependences of the Cu spin-lattice relaxation rate and the Knight shift are quantitatively described within the framework of the one-dimensional electron gas model [4, 5], where the anisotropy and the correlation of the chain electron system are taken into account. Electric field gradient fluctuations due to charge carriers in the chains contribute partly to the chain Cu relaxation and dominate the apex oxygen relaxation. The different temperature dependences of the magnetic and quadrupolar relaxation rates of the chain Cu (see Figure 10.1) seem to confirm the separation of low energy spin and charge excitations (spin-charge separation), expected in the framework of the one-dimensional electronic gas model.

Finally, we showed that the drop in the chain's magnetic shift at T_c seems to be related to the occurrence of superconductivity in the chains through the proximity effect. Our experimental findings are not compatible with a charge density wave transition in the chains. Such a transition has been discovered in the chains of $\text{PrBa}_2\text{Cu}_3\text{O}_7$ and has been suggested for the chains of $\text{YBa}_2\text{Cu}_3\text{O}_7$.

10.2.3 Magnetic properties of Cu–O chains in $\text{YBa}_2\text{Cu}_3\text{O}_7$ and $\text{YBa}_2\text{Cu}_4\text{O}_8$

A different and more sophisticated approach to understand hole-doped chains in Y–Ba–Cu–O superconductors is the following. It is known that, in one-dimension, the Fermi-liquid paradigm, based on the quasi-particle picture, breaks down and leads to anomalies of the magnetic properties. It is believed that the Luttinger-liquid approach is most appropriate for the description of the properties of 1D quantum systems [6]. This approach implies that the low-energy spectrum of the real 1D quantum system can be reproduced by the effective Luttinger-Tomonaga model which can be solved exactly [7].

Mapping the one-dimensional Hubbard model into the Luttinger–Tomonaga model, we have calculated the temperature dependencies of the chain copper nuclear magnetic spin-lattice relaxation rate and Knight shift for the normal state of the superconducting materials $\text{YBa}_2\text{Cu}_3\text{O}_7$ and $\text{YBa}_2\text{Cu}_4\text{O}_8$ [8]. The dynamic spin susceptibility has been calculated by

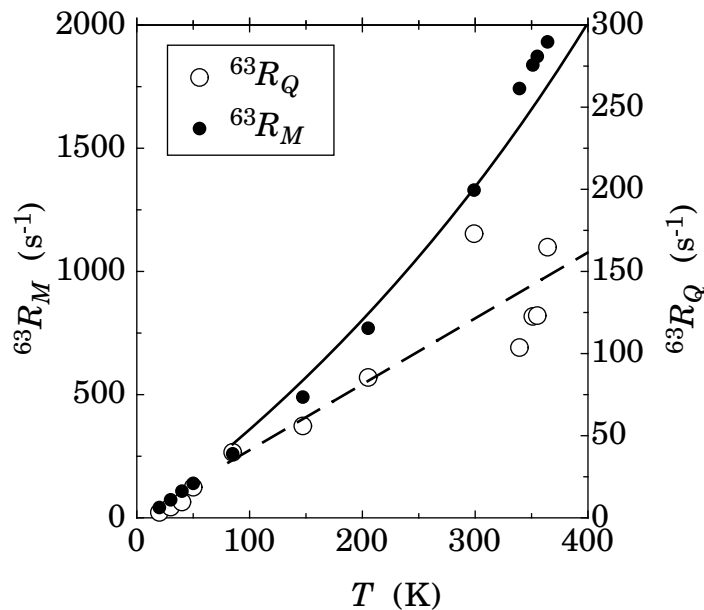


Figure 10.1: *Temperature dependence of the magnetic (R_M) and quadrupolar (R_Q) spin-lattice relaxation rate. The solid line is the result of the analysis based on the electron gas model. The dashed line is a guide to the eye.*

using a bosonization technique and results of the renormalization group analysis for the one-dimensional quantum systems. A comparison of our results with NMR data shows that the model is able to reproduce the main features of the spin dynamics in both materials. The set of fit parameters have reasonable values for both compounds and are naturally connected with each other.

10.2.4 Interplane electronic spin polarization transfer in the superconducting state of $Y_2Ba_4Cu_7O_{15}$

Superconductivity in Y–Ba–Cu–O compounds takes place in the CuO_2 planes which form double planes or bilayers. The coupling between individual planes of a bilayer and its influence on the spin dynamics are one of the most important topics in present research. In the past, we have performed extensive NQR/NMR studies of $Y_2Ba_4Cu_7O_{15}$ (2–4–7) by measuring various planar Cu NQR/NMR parameters such as different relaxation times and the Knight shift. We also have used NQR spin-echo double resonance (SEDOR) to confirm independently and directly the existence of the inter-plane coupling in 2–4–7 and have determined the temperature dependence of the inter-plane component of the static electron spin susceptibility in the normal state.

We have then extended those studies into the superconducting phase by again performing SEDOR NQR with the planar Cu sites in 2–4–7 [9]. The detailed analysis of the temperature dependence of the indirect in-plane relaxation rate, R_2 , and the inter-plane spin-spin relaxation rate, R_S^{inter} , reveals two results (see Figure 10.2): (i) In the normal conducting state, strong antiferromagnetic correlations exist between adjacent CuO_2 layers. (ii) In the superconducting state, the electronic spin polarization transfer between these layers is drastically reduced for decreasing temperature. Both results together strongly favor the interlayer tunneling model of P.W. Anderson and his colleagues.

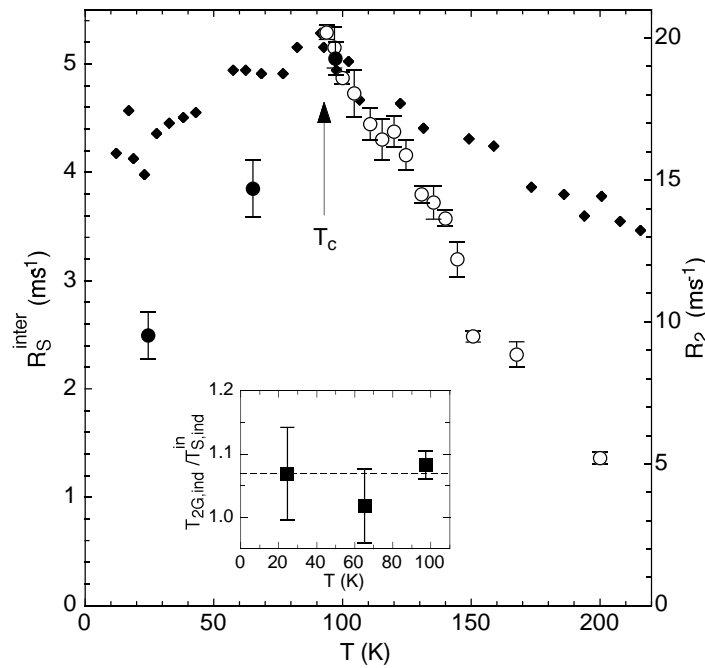


Figure 10.2: *Temperature dependence of the relaxation rates in $Y_2Ba_4Cu_7O_{15}$. Left scale: R_S^{inter} for the experiment $I = {}^{63}\text{Cu}(2), S = {}^{63}\text{Cu}(3)$ (open circles, our previous work) and for $I = {}^{63}\text{Cu}(3), S = {}^{63}\text{Cu}(2)$ (bullets). Right scale: R_2 of ${}^{63}\text{Cu}(3)$ (black diamonds, previous work). The vertical arrow denotes T_c . The inset shows $T_{2G,\text{ind}}/T_{S,\text{ind}}^{\text{in}}$ vs. temperature for the 1-2-4 block, where $T_{2G,\text{ind}}$ refers to ${}^{63}\text{Cu}(3)$ and $T_{S,\text{ind}}^{\text{in}}$ to the I-spin ${}^{65}\text{Cu}(3)$. The dashed line is a theoretical prediction.*

10.2.5 Cluster formation of chain oxygen vacancies in $\text{YBa}_2\text{Cu}_3\text{O}_{7-\delta}$ as the origin of the fishtail anomaly

There is an anomaly in the irreversible magnetization hysteresis curve in single crystals of $\text{YBa}_2\text{Cu}_3\text{O}_7$, often referred to as “fishtail effect”: the magnetization increases anomalously on increasing the magnetic field. This feature is still of particular interest since the high critical currents calculated from the maximum of the magnetization curve suggests that even at high fields large critical currents can be passed through this material.

It is a striking feature of *highly pure single crystals* of $\text{YBa}_2\text{Cu}_3\text{O}_{6.9}$ (1–2–3–6.9) that the fishtail effect can be switched off and on in a reversible manner by changing the annealing temperature. Erb *et al.* [10] have proposed the following model. Annealing the crystal at 510 K (and 1 bar oxygen pressure) causes clustering of the oxygen vacancies and the clusters form pinning centers which then lead to the fishtail effect. However, annealing the same sample at 650 K (and 100 bar), produces a random distribution of the vacancies which are now too small to act as pinning centers. In $\text{YBa}_2\text{Cu}_3\text{O}_7$, no fishtail effect could be observed due to the absence of vacancies.

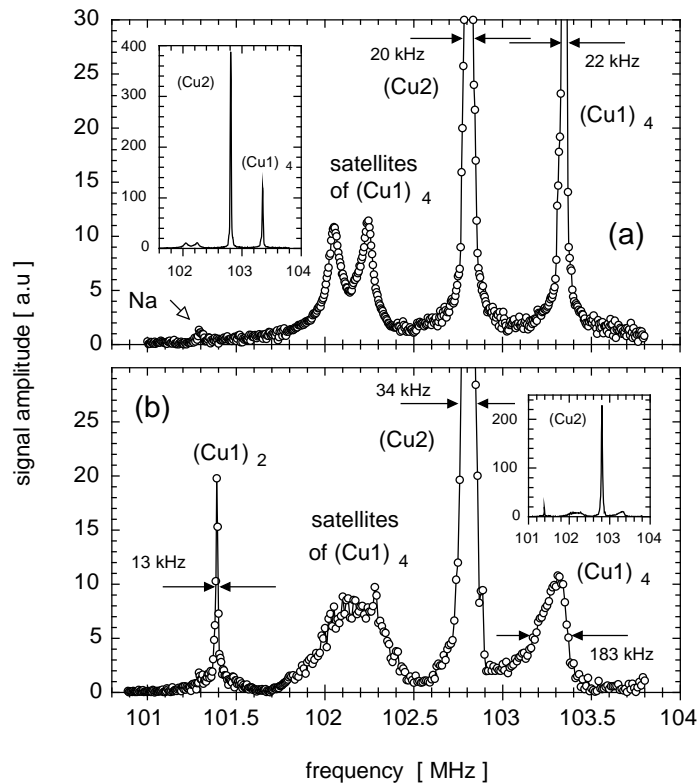


Figure 10.3: ^{63}Cu central (and satellite) lines of different sites are shown (a) for $\text{YBa}_2\text{Cu}_3\text{O}_7$ and (b) for $\text{YBa}_2\text{Cu}_3\text{O}_{6.9}$ at room temperature. The index denotes the oxygen coordination of the respective Cu site. The external magnetic field (8.995 Tesla) was oriented along the *c*-axis of the single crystal. The insets show the full size of the lines.

We have completed an extended series of Cu NMR and NQR (see *e.g.* Figure 10.3) to check the vacancy cluster hypothesis [11]. Together with magnetization measurements and positron annihilation spectroscopy, we found evidence that the formation of oxygen vacancy

clusters is the origin of the fishtail anomaly in $\text{YBa}_2\text{Cu}_3\text{O}_{7-\delta}$. Note that single vacancies or point defects cannot be responsible for the anomaly, since the anomaly can also be suppressed in the optimally doped state where vacancies are present. Thus, a formation mechanism that leads to larger nevertheless still microstructural inhomogeneities must be responsible for this effect. In the case of $\text{YBa}_2\text{Cu}_3\text{O}_{7.0}$, the anomaly is intrinsically absent unless the crystals contain metallic impurities. In such $\text{YBa}_2\text{Cu}_3\text{O}_{7.0}$ samples, melting of the vortex lattice has been observed by calorimetric measurements as a first order transition between 4 and 26.5 T, which was the highest available field, giving further support for our interpretation and yields new insight into the nature of the vortex matter.

What is still missing is the NMR/NQR evidence for the “inverse effect”: if the fishtail effect is absent, the NMR/NQR spectra should display the corresponding signals. However, it is difficult to suppress the fishtail effect completely in the large samples needed for the NMR/NQR experiments.

10.3 Antiferromagnetic parent compounds

There is a twofold interest in the electronic and magnetic structure of antiferromagnetic (AF) parent compounds from which many high-temperature superconductors are derived. First, there is the question about a possible interplay between magnetism and superconductivity. Even if there is no direct relation between magnetism and the mechanism of superconductivity, magnetism in these compounds certainly reflects the strong electronic correlation that exists and that must be taken into account in any attempt to explain electron pairing in cuprates. Second, the crossover between two-dimensional (2D) and three-dimensional (3D) magnetic systems offers insight into the spin dynamics of a so-called spin-1/2 2D quantum Heisenberg AF. We have continued these investigations by some general considerations of all these AF compounds and by a very detailed study of the bilayered $\text{YBa}_2\text{Cu}_3\text{O}_6$.

10.3.1 Sublattice magnetization in the antiferromagnetic parent compounds

The 3D ordered state of the AF parent compounds is a peculiar state with extreme anisotropic exchange couplings. One of the most important features of this AF state are the magnon excitations which can be studied via the temperature dependence of the sublattice magnetization, $M(T)$. Especially suited for these investigations is NMR in zero external magnetic field, a technique we have employed for several years, since the NMR Larmor frequency is a measure of $M(T)$.

The three antiferromagnets La_2CuO_4 , $\text{YBa}_2\text{Cu}_3\text{O}_6$, and $\text{Ca}(\text{Sr})\text{CuO}_2$ exhibit a common feature: the temperature dependence of the relative decrease of $M(T)$ follows a power law, that is $[M(0) - M(T)]/M(0) = AT^n$, up to one-half of the Néel temperature (T_N) with the same power, $n \sim 2$; only the prefactor A differs from compound to compound. This behavior of $M(T)$ suggests a common mechanism responsible for the decrease.

We have now performed the missing *numerical* calculation of $M(T)$ for $\text{Ca}(\text{Sr})\text{CuO}_2$ [12] using the spin-wave model applied to a quasi-2D Heisenberg antiferromagnet (see Figure 10.4). We confirmed the experimental result that the power law is obeyed at temperatures below about $T_N/2$. Thus, all three antiferromagnets are well described, in the respective temperature range, as quasi 2D $S=1/2$ Heisenberg systems with the inter-layer coupling constant, J' , dominating the value of the prefactor A .

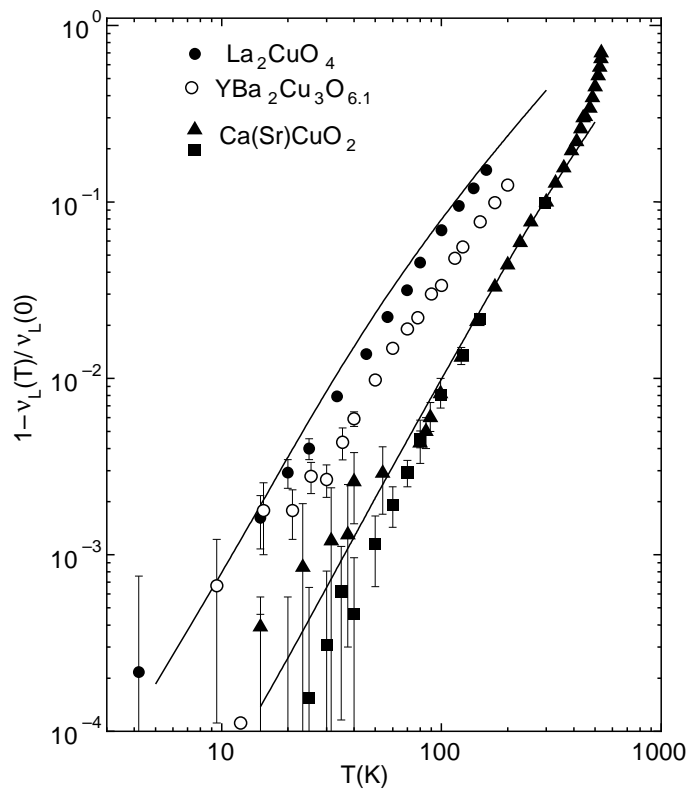


Figure 10.4: *The temperature dependence of the decrease of the Larmor frequency, $\nu_L(T)$, in La_2CuO_4 , $\text{YBa}_2\text{Cu}_3\text{O}_{6.1}$, and $\text{Ca}(\text{Sr})\text{CuO}_2$. The remeasured data for $\text{Ca}(\text{Sr})\text{CuO}_2$ are shown by full squares. The solid lines for La_2CuO_4 and $\text{Ca}(\text{Sr})\text{CuO}_2$ represent theoretical values calculated by means of the linear spin-wave model.*

10.3.2 The paramagnetic phase of $\text{YBa}_2\text{Cu}_3\text{O}_6$

Although $\text{YBa}_2\text{Cu}_3\text{O}_6$ is the AF parent compound of the whole Y–Ba–Cu–O superconductor family, an adequate NMR study of the planar Cu(2) site in the *paramagnetic* phase has still been missing. This is due to severe experimental difficulties like the extremely short spin–spin and spin–lattice relaxation of the planar Cu(2) nuclei as well as its disadvantageous quadrupole coupling. Because now sufficiently large *single* crystals are available (synthesized by A. Erb, University of Geneva), we have extended our studies to a large temperature range, extending from slightly below $T_N \cong 410$ K up to nearly 1000 K [13]. Our major results are as follows.

Above 500 K, the Cu(2) relaxation data reveal that $\text{YBa}_2\text{Cu}_3\text{O}_{6.12}$ is in the renormalized classical (RC) regime of a 2D quantum Heisenberg AF with spin $S=1/2$, what means that electron spins of neighboring planes fluctuate independently. From the data, we calculated the temperature dependence of the AF correlation length (see Figure 10.5) and determined a value for the hyperfine coupling constant at the Cu(2) site and the effective magnetic moment. We concluded that, among the antiferromagnets La_2CuO_4 , $\text{YBa}_2\text{Cu}_3\text{O}_6$, and $\text{Ca}_{0.85}\text{Sr}_{0.15}\text{CuO}_2$, the value of the effective magnetic moment is larger the stronger the magnetic inter–plane coupling. Above 600 K, the Cu(2) hyperfine coupling constant exhibits an unusual change which is not yet explained. We inferred, from the Cu(1) relaxation above 500 K, that diffusion of remnant oxygen in the chains is present.

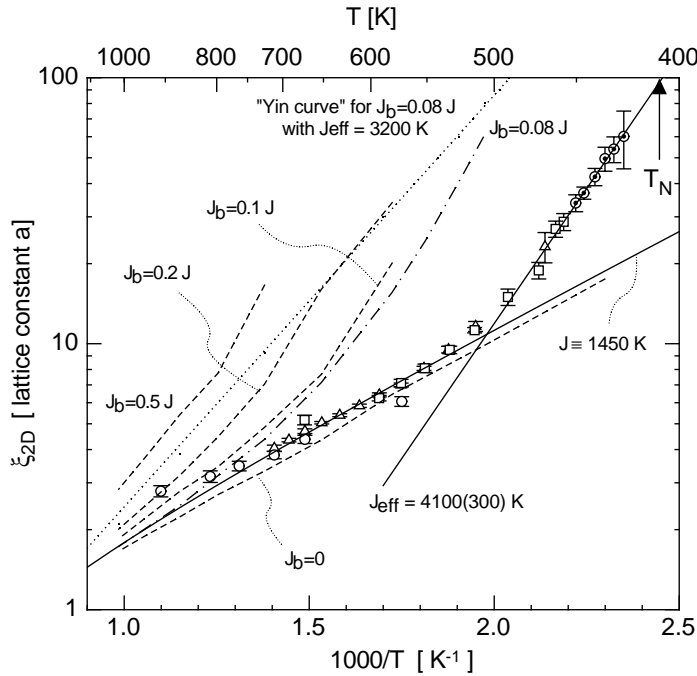


Figure 10.5: The planar antiferromagnetic correlation length, ξ_{2D} , as a function of inverse temperature. The solid lines are fits to the experimental data at high temperature and above T_N , respectively. The dotted line represents the prediction for a $S=1/2$ bilayer quantum Heisenberg antiferromagnet in the renormalized classical regime with intra–bilayer coupling constant $J_b = 0.08J$. The dashed and dashed–dotted curves are the results of Quantum Monte Carlo calculations for bilayers with J_b ranging from $0.08J$ to $0.5J$.

Below 500 K, the individual layers in $\text{YBa}_2\text{Cu}_3\text{O}_{6.12}$ start to couple into pairs and the temperature dependence of the AF correlation length abruptly crosses over to a faster increase

when T_N is approached. The corresponding effective AF in-plane coupling constant becomes $J_{eff}=4100$ K, a value nearly three times larger than $J=1450$ K known for the isolated layer. A comparison with Quantum Monte Carlo calculations allows one to estimate an intra-bilayer coupling constant, $J_b/J \lesssim 0.01$, which is significantly smaller than $J_b/J = 0.08$ as obtained by neutron scattering experiments. The origin of this disagreement is not yet known. Only ≈ 5 K above T_N , also the bilayers begin to couple as indicated by a suppression of the Cu(1) relaxation rate.

The decoupling of the planes adds, at least partially, to the unusual increase of the ^{89}Y relaxation rate above 425 K. This rate enhancement with rising temperature was measured previously and was not fully understood.

Measuring the susceptibility anisotropy, we detected a crossover in the Cu(2) spin fluctuations. In the range $T_N \pm 5$ K, these fluctuations are XY-like and become, with rising temperature, increasingly isotropic; the crossover is already complete around 500 K. This behavior is similar to the crossover we observed recently in $\text{Ca}_{0.85}\text{Sr}_{0.15}\text{CuO}_2$.

The Néel temperature of $\text{YBa}_2\text{Cu}_3\text{O}_{6.12}$ does not depend on the orientation of the applied magnetic field of 5.16 Tesla. This behavior contrasts with that of $\text{Sr}_2\text{CuO}_2\text{Cl}_2$ where the orientational dependence of T_N is a consequence of its low value, namely 257 K.

10.4 Superionic glasses

10.4.1 Relaxation of the stationary phosphorus nucleus

Our investigation of lithium conducting phosphate glasses of composition $x\text{LiF}\cdot(1-x)\text{LiPO}_3$ has been motivated by the fact that addition of the dopant salt, LiF, enhances the conductivity; hence, we became interested in the microscopic counterpart of this effect. While previously dealing with ^7Li , ^6Li , and ^{19}F nuclei, we then turned to the nucleus, ^{31}P , of the stationary phosphorus ion. After studying the undoped sample, we now completed the investigations of doped samples [14].

Parameters of the lithium motion could be extracted from the ^{31}P NMR since the ^{31}P spin-lattice relaxation is driven by magnetic fluctuations due to lithium ion motion. For modelling the temperature and frequency dependence of the spin-lattice relaxation rates, we employed the Bloembergen-Purcell-Pound theory modified with a Gaussian distribution of activation energies for the lithium motion. This distribution function takes care of the intrinsic disorder of the glass. We achieved to describe the relaxation data in the rotating frame as well as in the laboratory frame of reference with the *same* parameter set, thereby covering a wide frequency range from about 30 kHz to 80 MHz (see Figure 10.6). For both samples, the values for the center of the activation energy distribution agree very well with results obtained by DC conductivity measurements. The increase of the distribution width with increasing LiF content is attributed to a larger variety of lithium sites in the doped sample. These results demonstrate that even a “simple” relaxation model allows considerable insight into the ion dynamics. At low temperature, the relaxation rates evidence augmented network dynamics in the doped sample which is in accordance with the lower value of the glass transition temperature.

10.4.2 Magic angle spinning

Magic angle spinning (MAS) makes the time averaged dipolar coupling in a solid to vanish; it eliminates chemical shift anisotropies and first-order quadrupole couplings. In order to

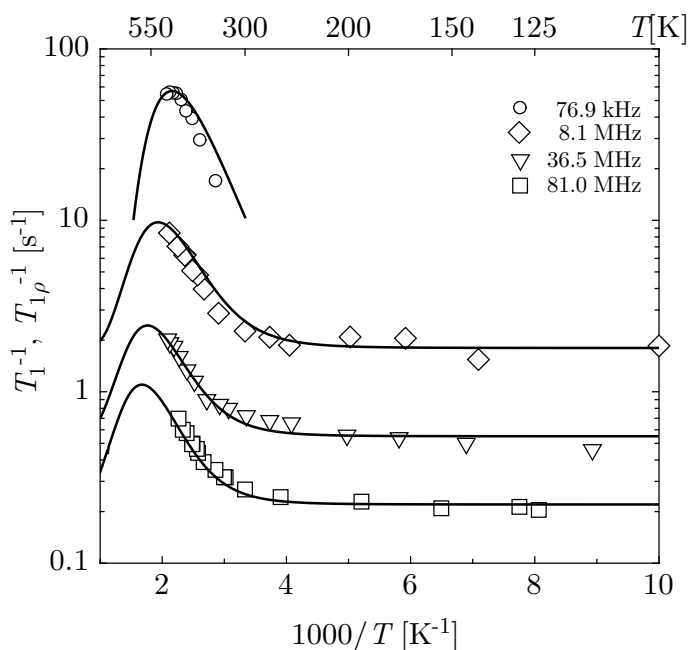


Figure 10.6: *Temperature dependent ^{31}P spin-lattice relaxation rates in $0.35\text{LiF}\cdot 0.65\text{LiPO}_3$ at various frequencies. Rates at 76.9 kHz have been measured in the rotating frame, the others in the laboratory frame.*

investigate the influence of doping on the structural change of the glassy network in $x\text{LiF}\cdot(1-x)\text{LiPO}_3$, we have now employed ^{31}P MAS [15] to samples with x between 0 and 0.35 (see Figure 10.7).

Usually, the phosphate glass structure is described by Q^n groups which are basic structure units (PO_4 tetrahedra) where n is the number of bridging oxygens per PO_4 tetrahedron. The MAS spectra obtained at room temperature reveal two peaks. The former peak is attributed to Q^e tetrahedra (end groups) while the latter is a superposition of mid-chain and cyclic Q^2 phosphates. With increasing LiF content the number of end units increases whereas the number of cyclic/mid-chain phosphate groups is reduced.

10.4.3 ^{31}P - ^{19}F spin-echo double resonance (SEDOR)

We have resumed our study of the stationary fluorine ions by performing new ^{19}F NMR experiments in $0.3\text{LiF}\cdot 0.7\text{LiPO}_3$. One part of the fluorine ions substitutes bridging oxygens in a PO_4 tetrahedron leading to structural depolymerization by creating PO_3F chain-end groups. The other part of the fluorine ions is embedded in the glassy structure as Li^+F^- fragments. Both types of ions show up in the ^{19}F NMR spectrum as resonance lines with different chemical shifts (see “Left” of Figure 10.8). The spectrum has been fitted by three Gaussian curves, A1, A2, and A3; the latter curve has been introduced because of the asymmetry of the spectrum at higher frequency. In the literature so far, the assignment of the two fluorine lines was simply based on the similarity of their shifts with ^{19}F shifts observed in other fluorinated phosphate compounds.

We obtained a more direct proof for the line assignment by performing a ^{31}P - ^{19}F spin-echo double resonance (SEDOR) experiment which directly yields the second moment of the heteronuclear dipolar coupling between ^{31}P and ^{19}F nuclear spins; the moment is highly de-

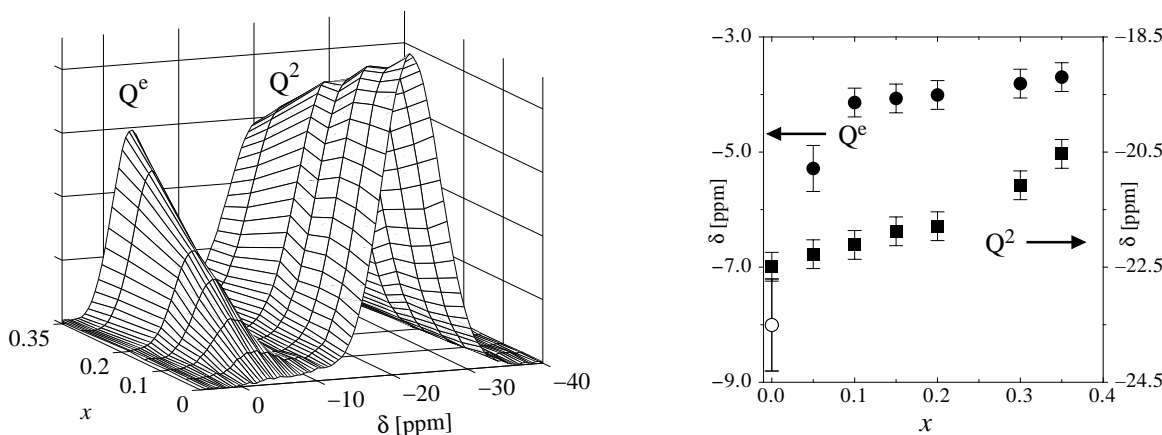


Figure 10.7: ^{31}P MAS in $x\text{LiF}\cdot(1-x)\text{LiPO}_3$. Left: Spectra. Right: Isotropic chemical shift, δ , of phosphate end groups (Q^e , \bullet , left axis) and middle units (Q^2 , \blacksquare , right axis) as a function of x . The open circle refers to Q^1 tetrahedra in undoped LiPO_3 .

pendent on the distance between these nuclei, $r_{\text{P-F}}$, via a term $(r_{\text{P-F}})^{-6}$. The second moment leads to a decay of the echo intensity as observed in the measurement (see “Right” of Figure 10.8). The much stronger echo decay of line A2 compared to the two others immediately shows that the corresponding fluorine nuclei are closest to the phosphorus nuclei. Hence, fluorine nuclei yielding line A2 have to be assigned to PO_3F tetrahedra and lines A1 and A3 to the Li^+F^- fragments which are more distant to the central phosphorus atom of the PO_4 tetrahedra.

10.5 High-pressure NMR in $\text{Ca}_{0.85}\text{Sr}_{0.15}\text{CuO}_2$

Last year, we had reported on high-pressure studies of the antiferromagnet $\text{Ca}_{0.85}\text{Sr}_{0.15}\text{CuO}_2$ (CASCO) using our helium-pressure device. We have studied this compound very intensively before by other NMR/NQR techniques.

Having improved our diamond-anvil cell device, we now extended our CASCO studies to pressures beyond 0.7 GPa. Our objective is to determine the variation of the sublattice magnetization with pressure, that is in the antiferromagnetic phase. By employing the internal magnetic field, one performs ^{63}Cu NMR without an external magnetic field; the Larmor frequency is a measure for the sublattice magnetization. Between 1 and 2 GPa, we measured an increase of the magnetization with increasing pressure; this is in accord with our results from the helium-pressure experiments below 0.7 GPa. However, beyond 2 GPa we observed a decrease of the magnetization. This is very difficult to understand and it might be due to a technical defect. Thus, further experiments are needed in that pressure range before a final conclusion can be drawn.

References

- [1] F. Raffa, T. Ohno, M. Mali, J. Roos, D. Brinkmann, K. Conder, and M. Eremin, Phys. Rev. Lett. 81 (1998) 5912

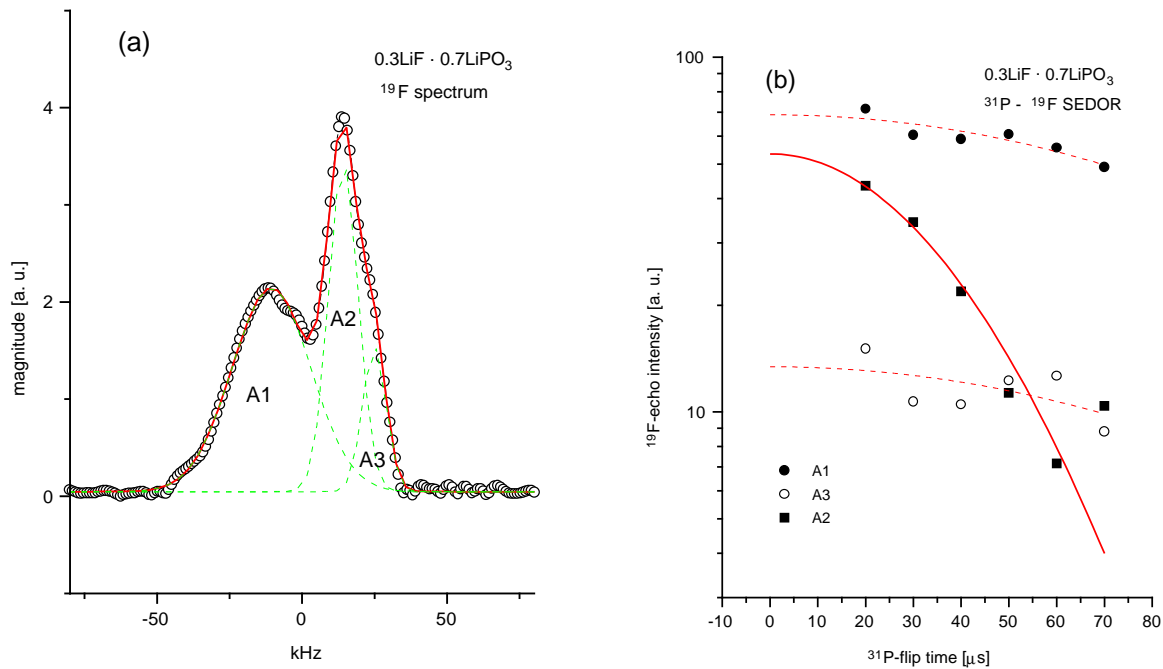


Figure 10.8: ^{31}P - ^{19}F spin-echo double resonance (SEDOR) experiment in $0.3\text{LiF} \cdot 0.7\text{LiPO}_3$. Left: ^{19}F spectrum with three signals A1, A2, and A3. Right: Decay of the three ^{19}F echo signals if the ^{31}P spin is flipped.

- [2] G.V.M. Williams, J.L. Tallon, J.W. Quilty, H.J. Trodahl, and N.E. Flower, Phys. Rev. Lett. 80 (1998) 377
- [3] F. Raffa, M. Mali, A. Suter, A. Yu. Zavidonov, J. Roos, D. Brinkmann, and K. Conder, submitted to Phys. Rev. B
- [4] J. Solyom, Adv. Phys. 28 (1979) 201; V. J. Emery, in *Highly Conducting One-Dimensional Solids*, edited by J. T. Devreese, R. P. Evrard, and V. E. van Doren (Plenum, New York and London, 1979) Chap. 6
- [5] C. Bourbonnais, P. Wzietek, F. Creuzet, D. Jérôme, P. Batail, and K. Bechgaard, Phys. Rev. Lett. 62 (1989) 1532; C. Bourbonnais, J. Phys. I France 3 (1993) 143
- [6] V. J. Emery, in *Highly Conducting One Dimensional Solids*, edited by J. T. Devreese *et al.* (Plenum Press, New York, 1978)
- [7] D. C. Mattis and E. H. Lieb, J. Math. Phys. 6 (1965) 304
- [8] A. Yu. Zavidonov and D. Brinkmann, to be submitted to Phys. Rev. B
- [9] A. Suter, M. Mali, J. Roos, and D. Brinkmann, Phys. Rev. Lett. 82 (1999) 1309
- [10] A. Erb, J.Y.Genoud, F. Marti, M. Däumling, E. Walker, and R. Flükiger, J. Low Temp. Phys. 105 (1996) 1033
- [11] A. Erb, A. A. Manuel, M. Dhalle, F. Marti, J.-Y. Genoud B. Revaz, A. Junod, D. Vasumathi, S. Ishibashi, A. Shukla, E. Walker, Ø. Fischer, R. Flükiger, R. Pozzi, M. Mali, and D. Brinkmann, submitted to Phys. Rev. Lett.

-
- [12] M.Matsumura, F.Raffa, and D. Brinkmann, submitted to Phys. Rev. B
 - [13] R. Pozzi, M. Mali, D. Brinkmann, A. Erb, and R. Flükiger, submitted to Phys. Rev. B
 - [14] S. Berger, J. Roos, A.Yu. Zavidonov, and D. Brinkmann, Solid State Ionics 112 (1998) 87
 - [15] S. Berger, M. Foglia, J. Roos, and D. Brinkmann, Joint 28th AMPERE - 13th ISMAR Conference, Berlin, August 2-7, 1998

11 Magnetic and Thermal Properties of Superconducting and Related Materials

H. Keller, C. Aegerter (till Jan. 99), J. Hofer, V.A. Ivanshin (visiting scientist), A. Schilling, A. Shengelaya, M. Willemin, G.M. Zhao, and K.A. Müller (Honorarprofessor)

11.1 Introduction

Over the past year we have continued and extended our investigations of the magnetic properties of high-temperature superconductors (HTS) and related magnetic systems. In order to achieve this goal we have used a combination of muon spin rotation (μ SR), neutron scattering, electron paramagnetic resonance (EPR), together with bulk SQUID and torque magnetometry, and thermal measurements.

During the last year we have continued our muon-spin rotation (μ SR) and neutron scattering experiments on the structure of the magnetic field distributions in superconductors (see Sec. 11.2). Apart from the well established neutron scattering investigations at the Institut Laue-Langevin (ILL), we have this year also had the opportunity to carry out experiments on the new spallation source SINQ at the Paul Scherrer Institut (PSI). These investigations at PSI will hopefully in the future complement the work at ILL. Moreover, we have extended our detailed investigations of the magnetic penetration depth in cuprate and related superconductors to the $\text{YBa}_2\text{Cu}_4\text{O}_8$ family (see Sec. 11.3).

In the last year we have further developed the technique to study vortex matter in highly anisotropic superconductors by means of ultrasensitive torque magnetometry (see Sec 11.4). In particular, we have demonstrated that the application of an additional oscillating magnetic field perpendicular to the main field may affect dramatically the irreversibility of high-temperature superconductors. The reversible domain in the (H, T) phase diagram can be extended, which is of particular interest for torque investigations in samples dominated by pinning. Ultrasensitive torque magnetometry measurements on untwinned single crystal of $\text{YBa}_2\text{Cu}_3\text{O}_{7-\delta}$ reveal that the vortex-lattice melting transition is unaffected by this additional ripple magnetic field.

In a further project, we have completed a detailed thermal and magnetic study on the angular dependencies of the discontinuities in entropy and in magnetization at the first-order vortex-lattice melting transition in untwinned $\text{YBa}_2\text{Cu}_3\text{O}_{7-\delta}$. We have also built up a new sensitive heat capacity device (estimated resolution 10^{-10} J/K) that can be operated between 40 K and 300 K, and in magnetic fields up to 10 T (see Sec 11.5).

We have continued our studies of oxygen-isotope effects in the magnetoresistive manganites $\text{Ln}_{1-x}\text{A}_x\text{MnO}_3$ (Ln is a rare-earth element, A is a divalent element) using magnetization and resistivity measurements (see Sec. 11.6.1). We found that the exponent of the oxygen-isotope effect on the Curie temperature T_C is simply proportional to the pressure-effect coefficient, and is a unique and simple function of T_C in the composition region where there is a metallic ground state. The results clearly show that the giant oxygen-isotope effects observed in the manganites are intrinsic, which give strong evidence for the polaronic nature of charge carriers in these materials. We have also studied the oxygen-isotope effect on the charge-ordering transition in $\text{Nd}_{0.5}\text{Sr}_{0.5}\text{MnO}_3$ and $\text{La}_{0.5}\text{Ca}_{0.5}\text{MnO}_3$. As the main result of this study, we discovered a colossal oxygen-isotope shift (> 40 K) of the charge-ordering transition temperature in both materials when a magnetic field of 5.4 T is applied. The isotope effect increases rapidly with increasing magnetic field. These results clearly establish that the strong electron-phonon coupling plays an essential role in the charge-ordering of manganites. Furthermore, we have studied the oxygen-isotope effects on the stripe for-

mation temperature T^* , and on the local structure deviations in the single-layer cuprate superconductors $\text{La}_{2-x}\text{Sr}_x\text{CuO}_4$, using x-ray absorption near-edge spectroscopy (XANES) (see Sec. 11.6.2). We found a very large oxygen isotope shift of T^* . Upon replacing ^{16}O with ^{18}O , the stripe formation temperature in $\text{La}_{1.94}\text{Sr}_{0.06}\text{CuO}_4$ increases from about 110 K to 170 K. Furthermore, the amplitude of the dynamic lattice distortions strongly depends on the oxygen isotope mass, that is, the amplitude of the distortion in the ^{18}O sample is much larger than that in the ^{16}O sample. These results will place important constraints on the microscopic origin of the stripe phase and on the microscopic mechanism of high-temperature superconductivity.

Electron Paramagnetic Resonance (EPR) is a powerful tool in solid state physics, which allows to study crystal electric fields, electron-phonon interactions, static and dynamic magnetic correlations on a *microscopic* level. EPR is a contact-less method, thus samples of any form (powder, pellet, single crystal, thin film) can be measured. Due to the extreme sensitivity of EPR, only a tiny amount of material is necessary. Our research interest during the last year was mainly concerned with oxygen isotope effects in high- T_c cuprates (see Sec. 11.6.3).

This work was done in collaboration with scientists from ETH Zürich (G. Blatter, K. Conder, J. Karpinski, and G.I. Meijer), IBM Rüşchlikon Research Laboratory (C. Rossel), University of Birmingham (E.M. Forgan, S.H. Lloyd, T. M. Riseman, T. J. Jackson, and P.G. Kealey), University of St. Andrews (S.L. Lee, F. Y. Ogrin, and C. Ager), Institut Max von Laue-Paul Langevin, Grenoble (R. Cubitt), University of Oxford (S.J. Blundell and B. W Lovett), RIKEN-RAL (F.L. Pratt), University of Warwick (D. McK. Paul and N. Bancroft), Oak Ridge National Laboratory (M. Yethiraj), Tohoku University (T. Sasaki), and Université Paris-Sud (S.T. Johnson and A. Revcolevschi), University of Maryland (R. L. Greene and K. Ghosh), University of Rome (A. Bianconi, N. L. Saini, and A. Lanzara), University of Berkeley (R.A. Fisher and N.E. Phillips), Los Alamos National Laboratory (M. Hundley and A. Lacerda), Argonne National Laboratory (U. Welp, W.K. Kwok, R.J. Olsson, and G.W. Crabtree), Institute of Low Temperature and Structure Research, Polish Academy of Sciences, Wroclaw, Poland (P.W. Klamut), and Northern Illinois University, DeKalb, USA (B. Dabrowski).

11.2 Investigating vortex matter at central facilities

The microscopic methods of muon spin rotation (μSR) and neutron small angle scattering (SANS) are ideal tools to investigate many facets of condensed matter systems. In our work we have been primarily occupied with investigating the structure and dynamics of magnetic flux-lines in superconductors. These structures are interesting in themselves, as they present a type of ‘matter’ whose microscopic structure (magnetic field) and interactions are well understood, but whose mesoscopic behavior is far from trivial. On a more applied note, the understanding of flux-lines sheds light on the superconducting properties of a specific system (as e.g. the low-temperature superconductor Sr_2RuO_4) and thus the superconducting mechanism of the material in question.

During the last years we have also started the investigation of the superconducting behavior of Sr_2RuO_4 (SRO). SRO is a superconductor, which is isostructural to the high- T_c cuprates, but does not contain copper [1]. Beside this obvious similarity, there are however also many differences that make SRO a research subject in its own right. Its electronic behavior differs in many respects and in the normal state can be well described by an anisotropic Fermi liquid [2]. This, together with the strong Hund’s rule coupling and the ferromagnetic nature of the relative compound SrRuO_3 , has lead to the theoretical expectation of very unusual superconducting behavior [3, 4]. It is thought that similar to superfluid He-3, the

pairing (of electrons) in SRO is in a triplet state, making SRO a p-wave superconductor. This makes it an exciting field of research decoupled from the HTS. The supposed p-wave nature of the superconductivity in SRO may also lead to very unconventional behavior of the flux line lattice in this material [4]. In the course of our studies using both SANS [5] and μ SR [6], we have found that the vortex lattice is of a square symmetry. In μ SR, this has been inferred from the detailed shape of the internal field distribution, determined by the positions of the minimum, maximum and saddle point fields as shown in Fig. 11.1. The SANS pattern, shown in the insert of Fig. 11.1, was taken subsequently to the μ SR experiments and confirms the earlier findings. The samples used in the investigations were from different sources with different levels of impurities, indicating that the squareness of the lattice is independent of the amount of impurities. This may arise from several reasons, such as a combination of non-local interactions and in-plane anisotropy. These effects have for instance been shown to give rise to unconventional (in some cases square) flux-lattices in superconductors of the Nickelborocarbide family [7]. In SRO a square lattice may also arise from the predicted effects of a p-wave symmetry of the supercarriers [4].

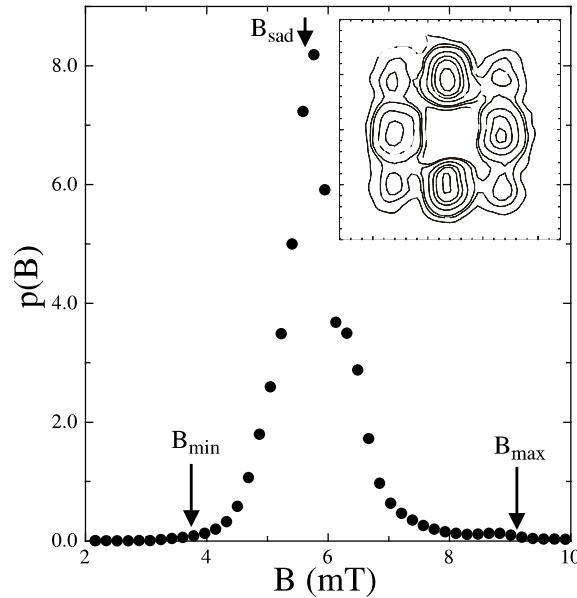


Figure 11.1: The μ SR lineshape $p(B)$ in SRO taken after cooling from above T_c in an applied field of 6mT. From the relative positions of the characteristic fields B_{min} , B_{max} and B_{sad} , we may induce the symmetry of the vortex lattice [6]. The insert shows a neutron diffraction pattern at a field of 20 mT.

Measurements of the temperature dependence of the penetration depth that is observable via the second moment of the field distribution and the scattered neutron intensity would be able to give further confirmation of the pairing state. In simple constant node theories of p-wave superconductivity [3] a saturation at low temperatures is expected. Our current measurements on this subject are still ambiguous and probably influenced by impurities. In order to further investigate the occurrence of a square flux-line lattice in this material, we also currently perform additional measurements with the applied field away from the high symmetry c -axis, which will allow us to discard possibilities like anisotropy or non-local effects due to the high anisotropy of the material. With the field at an angle, the upper critical field is increased considerably, leading to a strong reduction in non-local interactions. Furthermore, a possible in-plane anisotropy also becomes negligible due to the high c -axis anisotropy.

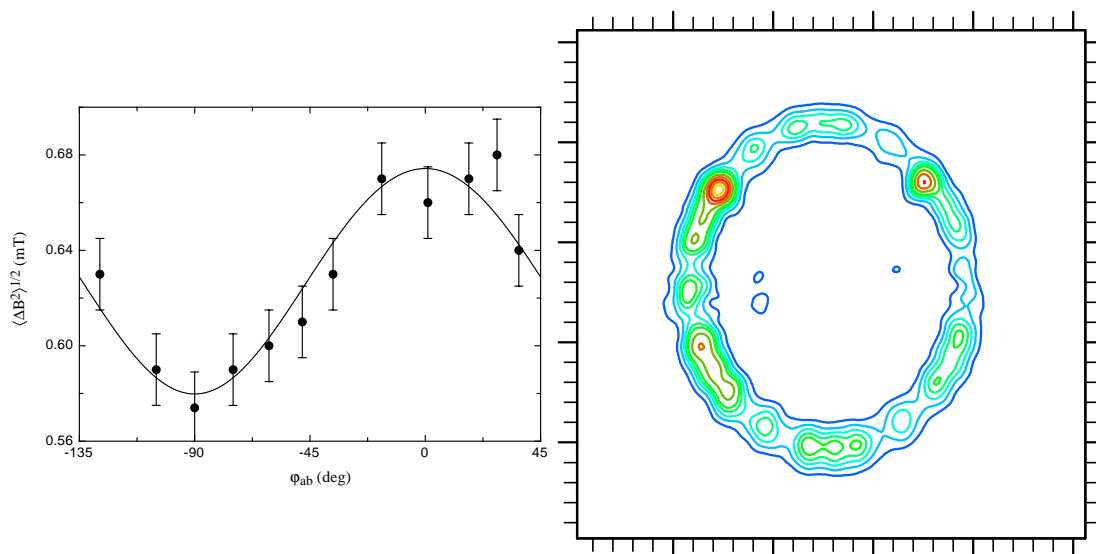


Figure 11.2: *The angular dependence of the second moment of the internal field distribution (left) and the neutron diffraction pattern for an untwinned sample (right). This gives a measure of the ab -anisotropy in the penetration depth.*

Due to the supposed d-wave pairing symmetry one might also expect unconventional vortex structures in the high-temperature superconductors (HTS). In many of these systems however, there are additional complications, such as the dimensional break-up of the vortex-lattice at fields much lower than H_{c2} in $\text{Bi}_2\text{Sr}_2\text{CaCu}_2\text{O}_{8+\delta}$ or twin-plane boundaries acting as strong pinning sites [8] in $\text{YBa}_2\text{Cu}_3\text{O}_{7-x}$ (YBCO) and anisotropic superconducting behavior in the crystallographic ab -planes. How these properties influence the structure of the vortex lattice in YBCO has been studied. We find that in heavily twinned samples, the effect of the pinning to twin boundaries dominates the observed structure leading to a fourfold diffraction pattern in SANS. This symmetry arises from the presence of both orientations of the ab -planes and does not correspond to a square lattice as has been claimed [9]. Even in nominally untwinned samples, there are still remaining influences of the pinning to twin boundaries. However, the ab -anisotropy in an untwinned sample is clearly observable in both neutron scattering and μSR . In the case of μSR the in-plane anisotropy is determined from the change in the width of the internal field distribution as the field is applied at different angles to the a -axis within the plane. The anisotropy also gives rise to the ellipsoidal shape of the scattering pattern in SANS, thus allowing a measurement of the anisotropy-parameter. This is illustrated in Fig. 11.2. Both methods determine the ab -anisotropy to be $\gamma_{ab} = 1.16(2)$ [10].

In addition, we have studied the melting of the vortex lattice in twinned and untwinned samples, where the melting is at much higher temperatures than for instance in BSCCO [11]. We find good agreement with specific heat [12, 13] and torque measurements [14] on similar crystals. The observed transition in twinned samples is gradual, consistent with being of second order. In the untwinned samples however, the transition is sharper down to low fields. Given the size of the crystals used in the investigation this is not inconsistent with a first order transition [13]. Furthermore, the melting temperatures are only weakly influenced by the presence of the twin planes, again in accord with specific heat measurements [12], and are in fair agreement with anisotropic scaling theory and latent heat measurements [15].

11.3 Penetration depth measurements in $\text{YBa}_2\text{Cu}_4\text{O}_8$ family superconductors

The magnetic field penetration depth λ is one of the fundamental lengths of a superconductor. The temperature dependence $\lambda(T)$ reflects the quasiparticle density of states available for thermal excitations and therefore probes the superconducting gap structure. A systematic and comprehensive study of the penetration depth and its temperature dependence in various families of cuprates is important for understanding the occurrence of superconductivity in these materials.

Detailed μSR investigations of polycrystalline high-temperature superconductors (HTS) have demonstrated that λ can be obtained from the μSR depolarization rate $\sigma(T) \sim 1/\lambda^2(T)$ [16]. Early μSR studies on polycrystalline HTS have concluded that σ has a weak temperature dependence for $T \ll T_c$, suggesting there is an energy gap in the spectrum of excitations, as expected for conventional *s*-wave pairing. On the other hand, more recent μSR measurements on high-quality $\text{YBa}_2\text{Cu}_3\text{O}_{7-\delta}$ (Y123) single crystals revealed a linear temperature dependence of σ up to $0.4T_c$ [17]. It is not clear why μSR measurements in polycrystalline and single crystal samples give different $\lambda(T)$ dependencies at low temperatures. It was suggested that small amounts of impurities or other crystalline imperfections can change the low-temperature behavior $\lambda(T)$ from a linear to a quadratic dependence [17], which is difficult to distinguish from the conventional BCS behavior without precise low-temperature data.

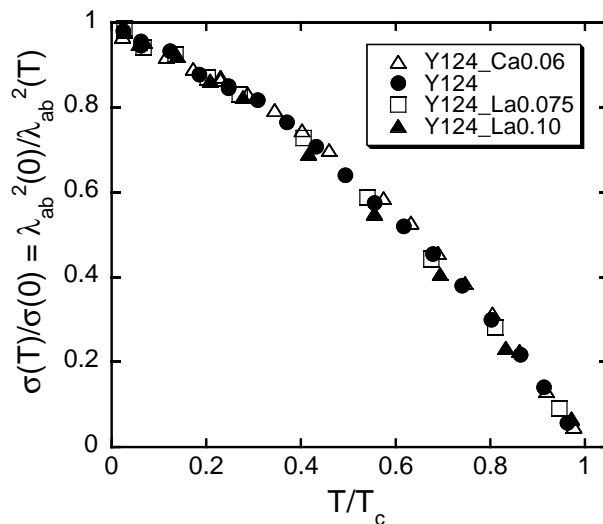


Figure 11.3: Normalized depolarization rate $\sigma(T)/\sigma(0)$ as a function of reduced temperature T/T_c for pure, Ca- and La-doped Y124 superconductors.

We have decided to study this problem in some detail by investigating the penetration depth in $\text{YBa}_2\text{Cu}_4\text{O}_8$ (Y124) with a special attention to the low-temperature behavior. The structure of Y124 is distinguished by its high thermal stability and fixed oxygen stoichiometry with well-ordered double CuO chains. We have investigated polycrystalline Ca- and La-doped $\text{YBa}_2\text{Cu}_4\text{O}_8$ superconductors with T_c ranging from 72 to 88 K [18]. It was found that in all samples $\sigma(T)$ is a linear function of T below ~ 25 K. In Fig. 11.3 we plot the normalized depolarization rate $\sigma(T)/\sigma(0)$ versus the reduced temperature $t = T/T_c$ so that the temperature dependencies for samples with different doping levels can be compared directly. It is seen that all samples exhibit quite a similar temperature dependence. Such a scaling behavior has recently been found by Hardy *et al.* [19] for single-crystal $\text{YBa}_2\text{Cu}_3\text{O}_{7-\delta}$

with $\delta=0.01, 0.05,$ and 0.40 from surface impedance measurements. This observation puts important constraints on models proposed to explain the linear temperature dependence of the penetration depth in HTS at low temperatures.

11.4 Investigating vortex matter by torque magnetometry

11.4.1 Enhancement of the vortex-lattice relaxation by means of an external ac magnetic field

Torque magnetometry has proven to be a useful method for determining superconducting parameters such as the in-plane penetration depth λ_{ab} , the in-plane coherence length ξ_{ab} , and especially the effective mass anisotropy γ in HTS. These parameters are generally derived by fitting the measured angular-dependent reversible torque with a theoretical expression derived by Kogan and coworkers [20] for a three-dimensional (3D) anisotropic superconductor in the mixed state. However, for a reliable analysis, the reversibility of the torque curves is required, i.e., the vortex lattice must be in a reversible state, corresponding to its thermodynamical equilibrium. Unfortunately, in most superconductors, only a narrow reversible range in the field-temperature (H, T) phase diagram below the upper critical field $H_{c2}(T)$ can be explored, owing to the onset of irreversibility by pinning effects at lower T . Moreover, close to T_c , the distortion of the torque signal due to the domination of thermal fluctuations has been predicted theoretically and observed experimentally [21]. In this regime, it is almost impossible to get a reliable value of γ . On the other hand, in a not too strong pinning regime, it is possible to analyze the reversible curve approximated by $\tau_{rev}(\theta) \simeq \frac{1}{2}(\tau^+(\theta) + \tau^-(\theta))$. However, in the presence of a large irreversibility, the anisotropy γ extracted in this way is overestimated.

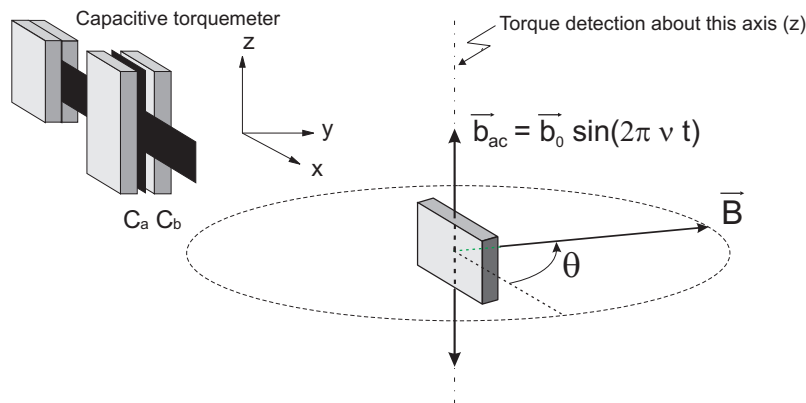


Figure 11.4: *Geometrical configuration for the “vortex-shaking procedure” during an angular-dependent torque measurement. \vec{B} and \vec{b}_{ac} denote the main and the weak ac field, respectively.*

In order to extend the reversible regime, a new method has been developed [22]. The application of a transverse ac magnetic field to the main magnetic field “shakes” the vortices out of their pinning potential, which enhances the relaxation of the flux-line lattice (FLL) towards its thermodynamical equilibrium (see Fig. 11.4). The vortex-shaking method is compatible with capacitive [23] as well as piezoresistive torque sensors [24] (see also Annual Reports 96/97 and 97/98). The power of this technique has been verified in several HTS compounds. A typical set of angular-dependent torque measurements for an untwinned single crystal of $\text{YBa}_2\text{Cu}_3\text{O}_{7-\delta}$ with and without FLL shaking is displayed in Fig. 11.5. In the absence of an oscillating field (no FLL shaking) the reversible torque curve $\tau_{rev}(\theta)$ can be fitted

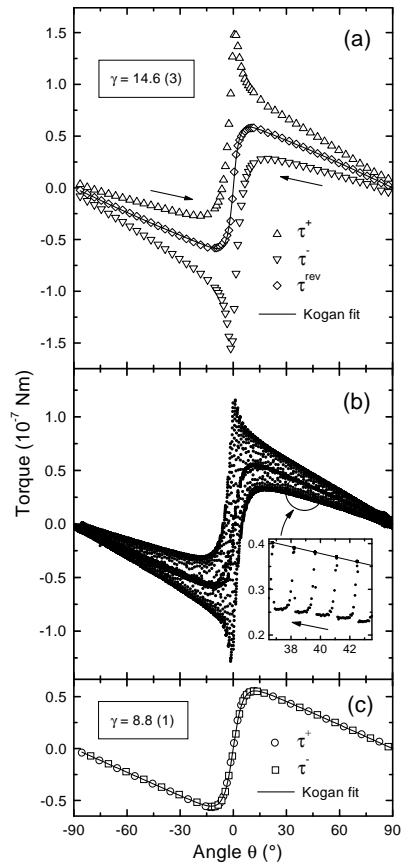


Figure 11.5: Angular-dependent torque measurements in the ac plane on an untwinned single crystal of $YBa_2Cu_3O_{7-\delta}$ ($\theta = 0^\circ$ for \vec{B} parallel to the ab -plane). (a) Torque for clockwise (τ^+) and counterclockwise (τ^-) rotations of \vec{B} obtained without FLL shaking at $T = 91.2$ K, $B = 0.1$ T and $d\theta/dt = 110^\circ/\text{min}$. The solid line represents the fit to $\tau_{\text{rev}}(\theta) \simeq 1/2(\tau^+(\theta) + \tau^-(\theta))$ with Kogan's expression, yielding $\gamma \simeq 14.6(3)$. (b) Similar measurements as in (a), but with vortex shaking. Details of relaxation sequences are shown in the inset. (c) The fit after FLL shaking gives $\gamma = 8.8(1)$. The curves are fully reversible in this case.

by the expression given by Kogan *et al.* [20] (Fig. 11.5(a)). By doing so, an unrealistically high value $\gamma = 14.6(3)$ is obtained, which is explained by the large irreversibility that peaks at $\theta \simeq 0$, i.e., for \vec{B} close to the ab plane of the sample. The above expression for $\tau_{rev}(\theta)$ is not suitable in this case. However, by applying the shaking procedure to the crystal at the same field ($B = 0.1$ T) and temperature ($T = 91.2$ K), a fully reversible curve is obtained as shown in Fig. 11.5(b). By considering only the data after the FLL relaxation, the fit leads to a realistic anisotropy $\gamma = 8.8(1)$ (Fig. 11.5(c)). For investigations of HTS in the mixed state this method is not only restricted to torque magnetometry, but can also be used by other techniques, like specific heat or resistivity.

11.4.2 First-order vortex-lattice melting transition in $\text{YBa}_2\text{Cu}_3\text{O}_{7-\delta}$ near the critical temperature detected by magnetic torque

Recent experimental work on the vortex-lattice melting in HTS clearly showed that the melting transition from the ordered vortex solid to a vortex-fluid phase, at the so-called “melting temperature” T_m , is of first order [25]. A first-order transition is characterized by a discontinuity ΔS in the entropy $S = -(\partial F/\partial T)_H$. This entropy discontinuity ΔS can be related to a discontinuity in the magnetization ΔM , according to the Clausius-Clapeyron equation

$$\Delta S = -\Delta M \mu_0 \frac{dH_m^c}{dT}. \quad (11.1)$$

Note that the melting temperature T_m depends on the applied magnetic field $\mu_0 H$, which forms the “melting line” $H_m(T)$ in the (H, T) phase diagram. Torque magnetometry is a very powerful tool for detecting the vortex-lattice melting transition (VLMT). Indeed, the discontinuity in magnetization ΔM is related to a step in the torque signal $\Delta\tau$. In a first approximation, assuming a magnetization perpendicular to the Cu-O planes of the crystal, the step in the torque signal is given by $\Delta\tau = V\Delta M\mu_0 H \cos\theta$, where V is the volume of the sample, and θ is the angle between the applied magnetic field \vec{H} and the Cu-O planes.

Figure 11.6(a) shows the VLMT as observed by field-dependent torque measurements taken at $T = 90.70$ K ($T_c = 93.3$ K) and different field-sweep rates. The solid phase is characterized by an irreversible behavior of the torque, which disappears in the fluid phase. At low sweep rates, the torque signal shows clearly more intrinsic noise. This is due to the fact that vortices discontinuously enter or leave the sample in successive flux bundles, while the magnetic field is swept. By adding a weak ac transverse magnetic field (vortex shaking), the irreversibility in the solid phase can be shifted down to lower magnetic fields (Fig. 11.6(b)). This offers the possibility to tune the irreversibility, leaving the VLMT unchanged. We performed a systematic study of the VLMT in $\text{YBa}_2\text{Cu}_3\text{O}_{7-\delta}$ by ultrasensitive torque magnetometry, especially near the critical temperature T_c (Ref. [14]). The novel results obtained in this study complement previous results from specific-heat measurements [26].

11.5 Detection of small thermal effects in basic and applied condensed matter physics

We have completed a detailed thermal and magnetic study on the angular dependencies of the discontinuities in entropy and in magnetization at the first-order vortex-lattice melting transition in untwinned $\text{YBa}_2\text{Cu}_3\text{O}_{7-\delta}$.

The melting lines $H_m(T, \vartheta)$, (where ϑ is the angle between the applied magnetic field \vec{H} and the c -axis of the crystal), as defined by the thermal experiments, scale perfectly according to recent scaling rules for anisotropic superconductors, with an anisotropy parameter $\gamma \approx 8$.

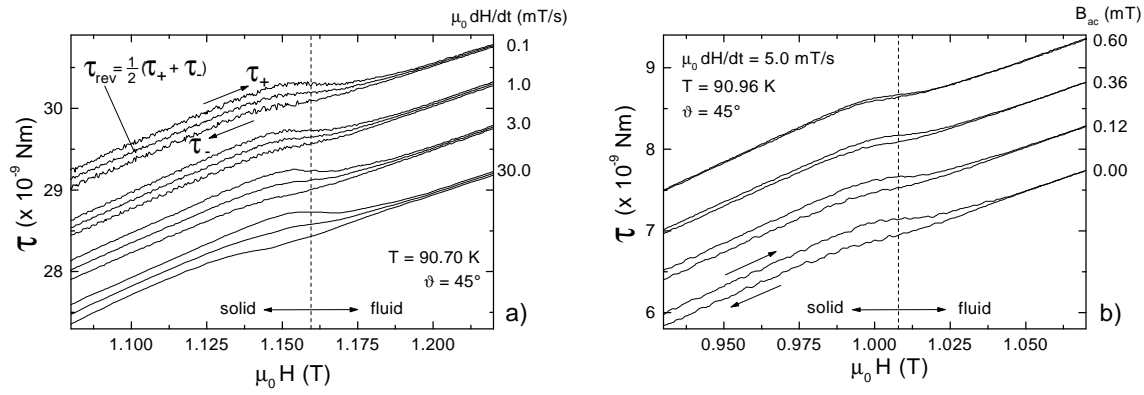


Figure 11.6: *The phase transition associated with vortex-lattice melting (dashed vertical line) as observed by field-dependent torque measurements on an untwinned single crystal of YBCO. (a) Magnetic torque τ for increasing (τ_+) and decreasing (τ_-) magnetic field $\mu_0 H$ for different sweep rates $\mu_0 dH/dt$, taken at 90.70 K and $\vartheta = 45^\circ$. The data reveal a constant magnetization jump ΔM at the VLMT, determined from the reversible torque curve τ_{rev} . (b) Similar measurements (90.96 K , $\vartheta = 45^\circ$) with an additional weak transverse ac magnetic field B_{ac} show a progressive suppression of irreversibility, remaining the VLMT itself unaffected. In both figures each set of data is vertically shifted for clarity.*

In the temperature range $81\text{ K} < T < T_c = 92\text{ K}$ and for any choice of ϑ , the discontinuity in entropy at melting, ΔS per unit volume of sample, depends solely on the temperature T where melting occurs, but does not depend on ϑ and the corresponding applied magnetic field $H_m(T, \vartheta)$, which is in full agreement with these scaling rules [26]. The temperature dependence of $\Delta S(T)$ near the critical temperature T_c , can be quantitatively explained by a recently developed theory that accounts for the strong T dependence of the model parameters near T_c for the London model describing the thermodynamics of the vortex system [27]. Along with the discontinuities in entropy due to the latent heat, nearly step-like increases in the specific heat of $\text{YBa}_2\text{Cu}_3\text{O}_{7-\delta}$ at the vortex-lattice melting temperature are observed [26]. These increases are reflected in changes in the slope $\Delta(\partial S/\partial T)_H$ at the melting temperature. However, the thermal data alone do not allow to conclude whether or not these slope changes depend only on T as predicted by theory.

To clarify these issues we performed a series of magnetization measurements on a different crystal in our home built torque magnetometer, in the temperature range $91\text{ K} < T < T_c = 93.3\text{ K}$ (in collaboration with C. Rossel, IBM Ruschlikon Research Laboratory). We measured the torque $\vec{\tau} = V\vec{M} \times \mu_0\vec{H}$ at a fixed temperature T for different magnetic fields H , and varied the angle ϑ . The resulting discontinuities at the melting transition are $\Delta\tau(\vartheta)$, with associated changes in slope $\Delta(\partial\tau/\partial H)_T$. In this way, the transverse component of the discontinuity $\Delta\vec{M}$ in magnetization \vec{M} can be directly measured. However, the smallness of both the investigated crystal and the effect to be observed, does not allow for a direct measurement of the longitudinal component of $\Delta\vec{M}$, e.g., using a SQUID magnetometer. We derive this component indirectly from thermodynamics. We use the fact that ΔS depends only on T , and the Clausius-Clapeyron formula gives an additional restriction. In this way we were able to determine both components of the vector $\Delta\vec{M}$, and to study its rotation when the angle ϑ approaches the direction of the Cu-O planes.

The final result is that the vector $\Delta\vec{M}$ is always directed parallel to the total magnetization \vec{M} (but not necessarily parallel to the c -axis), and is rotating away from c by the angle φ

according to $\tan \varphi = \tan \vartheta / \gamma^2$. The corresponding changes in slope, $\Delta(\partial\tau/\partial H)_T$, strongly depend on ϑ . They can be translated to discontinuities in specific heat using rather complex thermodynamic relations, and turn out to be independent of ϑ as expected by theory. The agreement between all these magnetic data and the thermal data is excellent. The anisotropy parameter γ can be extracted from all these measurements, and turns out to be constant ($\gamma \approx 8.2$) up to the highest investigated temperature ($T = 92.4$ K).

We have also done an additional series of thermal measurements in magnetic fields up to 18 T, to study the critical endpoint of the vortex-lattice melting line, and to investigate whether or not there are additional phase boundaries in the magnetic phase diagram (in collaboration with the Los Alamos National Laboratory, Los Alamos, USA). The critical point in the investigated sample is at $\mu_0 H = 12$ T for $\vec{H} \parallel c$. Measurements at fixed temperature and in varying magnetic field allowed us to investigate the thermomagnetic behavior both below and above the vortex-lattice melting line. There is no conclusive thermal sign of a horizontal phase boundary as suggested by theory, that should indicate the transition (or crossover) from a 3D-like to a 2D-like vortex dynamics.

We have built up a new sensitive heat capacity device that is based on a differential calorimetry technique [28]. It can be operated between 40 K and 300 K, and in magnetic fields up to 10 T. The sample holder can be rotated in the magnetic field, and allows therefore for convenient angular dependent heat-capacity experiments. With a new design and improved thermometry, we are able to achieve a resolution in heat capacity that is improved by a factor of 100 compared to the standard technique [28].

11.6 Studies of oxygen isotope effects

11.6.1 Oxygen isotope effects in the manganites

The giant oxygen-isotope shift of the Curie temperature T_C in $\text{La}_{0.8}\text{Ca}_{0.2}\text{MnO}_{3+y}$ discovered by us [29] provides crucial evidence for the existence of small polarons (Jahn-Teller (JT) polarons [30]) in these materials, and place important constraints on the microscopic mechanism of the colossal magnetoresistance effect. However, some physicists have raised criticisms on those isotope-effect experiments by speculating that the observed oxygen-isotope effects have nothing to do with a strong electron-phonon interaction, but are caused by the presence of excess oxygen. In order to address this issue, we systematically studied the oxygen-isotope effects in $\text{Ln}_{1-x}\text{A}_x\text{MnO}_3$ as a function of x and of T_C , and compared the results with the pressure effect data. We found that the exponent of the oxygen-isotope effect on the Curie temperature T_C is simply proportional to the pressure-effect coefficient, and is a unique and simple function of T_C in the composition region where there is a metallic ground state (see in Fig. 11.7). The results clearly show that the observed oxygen-isotope effects in the manganites are intrinsic. There are no correlations between the oxygen-isotope effects and the excess oxygen; the oxygen-isotope exponent is a unique function of T_C .

The real-space ordering of charge carriers in crystals is one of the most interesting phenomena in condensed matter physics. Such a charge-ordering state has been observed mostly in transition-metal based oxides, such as Ti_4O_7 [31], $\text{La}_{2-x}\text{Sr}_x\text{NiO}_4$ [32], $(\text{La,Pr,Nd})_{0.5}\text{Ca}_{0.5}\text{MnO}_3$ [33, 34], $(\text{Pr,Nd})_{0.5}\text{Sr}_{0.5}\text{MnO}_3$ [35, 36], etc. In particular, the charge-ordering in manganites is rather exotic. As an example, the charge-ordering state in the manganites $\text{Nd}_{0.5}\text{Sr}_{0.5}\text{MnO}_3$ and $\text{Pr}_{0.5}\text{Sr}_{0.5}\text{MnO}_3$ can be destroyed by a small magnetic field (< 10 Tesla) [35, 36]. Theoretically, it has been proposed that the long-range Coulomb repulsive interaction among conduction carriers might be responsible for the charge-ordering in these systems [37, 38, 39].

Our isotope experiments do not support these theoretical models. There is a large oxygen isotope effect on the charge-ordering transition temperature in both $\text{Nd}_{0.5}\text{Sr}_{0.5}\text{MnO}_3$ and

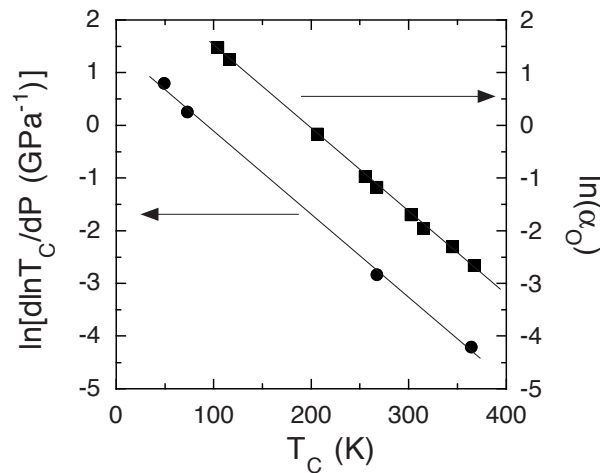


Figure 11.7: The pressure-effect coefficient β (for a fixed $x = 0.3$) and the oxygen-isotope exponent α_O ($0.2 < x < 0.33$) as a function of T_C .

$\text{La}_{0.5}\text{Ca}_{0.5}\text{MnO}_3$. In Fig. 11.8, we show the temperature dependence of the normalized magnetizations for the ^{16}O and ^{18}O samples of $\text{Nd}_{0.5}\text{Sr}_{0.5}\text{MnO}_3$ under a magnetic field of 2.5 T. The transition from a high magnetization to a low magnetization state is a signature of the transition from a ferromagnetic to a charge-ordering (CO) state. It is clear that there is a large oxygen isotope shift (~ 20 K) of the charge-ordering transition temperature T_{CO} , and that the shift is completely reversible upon the oxygen isotope back-exchange. Furthermore, we found that with an increase of the external magnetic field, the charge-ordering temperatures of both ^{16}O and ^{18}O samples decrease, but the decreasing rate for the ^{18}O sample is much slower than for the ^{16}O sample. This leads to a dramatic increase in the oxygen isotope shift with increasing magnetic field

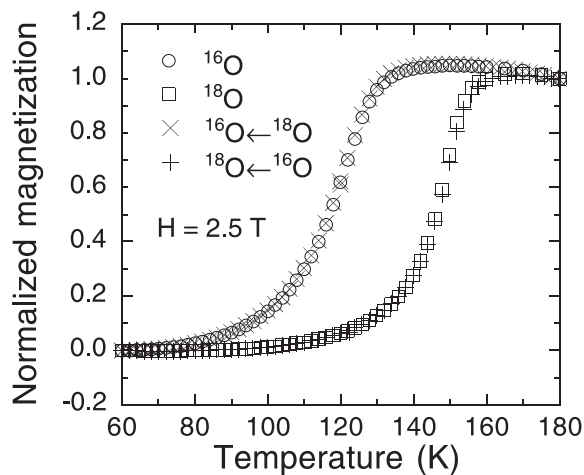


Figure 11.8: Oxygen-isotope effect on the charge-ordering transition in $\text{Nd}_{0.5}\text{Sr}_{0.5}\text{MnO}_3$ and the oxygen isotope back-exchange result.

The observed large oxygen-isotope shift of the charge-ordering temperature and its strong dependence on the applied magnetic field are difficult to understand on the basis of the existing theories. In most theoretical models, the charge-ordering arises from a long-range

Coulomb repulsive interaction between carriers [37, 38, 39]. So these models predict no isotope effect, and cannot explain our present results.

11.6.2 Oxygen isotope effects in $\text{La}_{2-x}\text{Sr}_x\text{CuO}_4$

One of the outstanding features of cuprate superconductors is the formation of alternative spin and charge stripes below a characteristic temperature [40, 41]. Various x-ray absorption spectroscopic measurements [42, 43, 44] suggest that the local structures in the alternated stripes are different, forming an incommensurate superlattice. Such a stripe phase is believed to be important to the understanding of the pairing mechanism of high-temperature superconductivity. However, the microscopic origin of the stripe phase is still highly debated. It could be caused by purely electronic interactions and/or by a strong electron-phonon coupling. In order to assess whether the latter interaction plays an important role in this phenomenon, we studied the isotope effects on the stripe formation temperature and on the local lattice distortions. We found a very large oxygen isotope shift of the stripe formation temperature in $\text{La}_{1.94}\text{Sr}_{0.06}\text{CuO}_4$ from x-ray absorption spectroscopic study. Upon replacing ^{16}O with ^{18}O , the stripe formation temperature in $\text{La}_{1.94}\text{Sr}_{0.06}\text{CuO}_4$ increases from about 110 K to 170 K. Furthermore, the amplitude of the dynamic lattice distortions strongly depend on the oxygen isotope mass, that is, the amplitude of the distortion in the ^{18}O sample is much larger than that in the ^{16}O sample. Such a huge oxygen-isotope effect cannot be explained by any theoretical models which have ignored a strong electron-phonon interaction. The results will place important constraints on the microscopic origin of the stripe phase and on the microscopic mechanism of high-temperature superconductivity.

11.6.3 EPR study of oxygen isotope effect in $\text{La}_{2-x}\text{Sr}_x\text{CuO}_4$

Cuprate superconductors are known to exhibit a strong Jahn-Teller (JT) effect, which can lead to JT polaron formation. It is well known that the important theoretical concept of JT polarons proposed by Höck et al. [30] led to the original discovery of high-temperature superconductivity [45].

To check this possibility we decided to perform a EPR study of $\text{La}_{2-x}\text{Sr}_x\text{CuO}_4$ (LSCO) with different oxygen isotopes (^{16}O and ^{18}O). This compound was doped with a few percent of Mn ions (1-2 %) which served as a EPR probe [46]. LSCO is particularly suitable for this kind of investigation. First of all, the structure of this compound is the simplest among the cuprates, containing a single Cu site which allows to dope Mn ions into the copper-oxygen layers. Furthermore, LSCO is the only cuprate superconductor for which the chemical composition can be varied over a wide enough range to obtain the full spectra of electronic properties: from an undoped antiferromagnetic to an overdoped metallic state. A symmetric EPR signal with a lineshape very close to Lorentzian and a g -value of 2.0 was observed in all samples. Fig. 11.9 shows the EPR signal of 2% Mn-doped $\text{La}_{1.94}\text{Sr}_{0.06}\text{CuO}_4$ for ^{16}O and ^{18}O isotope substituted samples. Note that the signal of the ^{16}O sample is stronger than that of the ^{18}O sample. The strong isotope effect observed in the EPR spectra is similar to our previous results obtained in the mixed valence perovskite manganite $\text{La}_{1-x}\text{Ca}_x\text{MnO}_{3+y}$ [47]. We have found that the isotope effect is strong in samples with small Sr doping (underdoped regime) and decreases with Sr concentration. An observation of the oxygen isotope effect on the EPR signal and its dependence on doping level in $\text{La}_{2-x}\text{Sr}_x\text{CuO}_4$ provides crucial information on the importance of the electron-phonon interaction in the spin dynamics of HTS and reflects the polaronic nature of the charge carriers in these compounds.

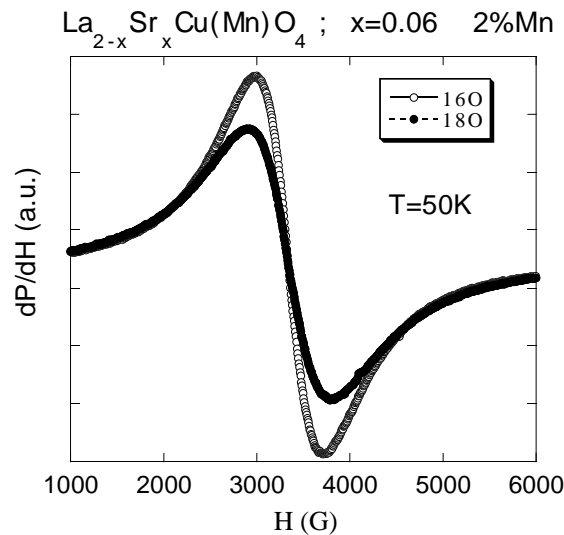


Figure 11.9: *EPR signal of ^{16}O and ^{18}O samples of $\text{La}_{1.94}\text{Sr}_{0.06}\text{Cu}_{0.98}\text{Mn}_{0.02}\text{O}_4$ measured at $T=50\text{ K}$ under identical experimental conditions.*

References

- [1] Y. Maeno *et al.*, *Nature* **372**, 532 (1994).
- [2] A.P. Mackenzie *et al.*, *Phys. Rev. Lett.* **76**, 3786 (1996).
- [3] T.M. Rice and M. Sigrist, *J. Phys (Cond. Mat.)* **7**, L643 (1995).
- [4] D.F. Agterberg, T.M. Rice, M. Sigrist, *Phys. Rev. Lett.* **78**, 3374 (1997); D.F. Agterberg, preprint (cond-mat 9802151).
- [5] T.M. Riseman *et al.*, *Nature* **396**, 242 (1998).
- [6] C. M. Aegerter *et al.*, *J. Phys. Cond. Mat* **10**, 7445 (1998).
- [7] D. McK. Paul *et al.*, *Phys. Rev. Lett.* **80**, 1517 (1998).
- [8] G. Blatter, J. Rhyner, and V. M. Vinokur, *Phys. Rev. B* **43**, 7826 (1991).
- [9] B. Keimer *et al.*, *Phys. Rev. Lett.* **73**, 3459 (1994); *Science* **262**, 83 (1993).
- [10] S.T. Johnson *et al.* to be published in *Phys. Rev. Lett.* (1999); C. Ager *et al.* preprint.
- [11] C.M. Aegerter *et al.*, *Phys. Rev. B* **57**, 1253 (1998); C.M. Aegerter *et al.* preprint.
- [12] M. Roulin, A. Junod, and E. Walker, *Science* **273**, 1210 (1996); *Physica C* **296**, 137 (1998).
- [13] A. Schilling *et al.*, *Nature* **382**, 791 (1996).
- [14] M. Willemin *et al.*, *Phys. Rev. Lett.* **81**, 4236 (1998).
- [15] A. Schilling *et al.*, *Phys. Rev. Lett.* **78**, 4833 (1997).
- [16] See, e.g. H. Keller, in *Materials and Crystallographic Aspects of HTc-Superconductivity*, edited by E. Kaldis (Kluwer Academic Publishers, 1994), p.265; C.M. Aegerter and S.L. Lee, *Applied Magnetic Resonance* **13**, 75 (1997) and references therein.

- [17] J.E. Sonier *et al.*, Phys. Rev. Lett. **72**, 744 (1994).
- [18] A. Shengelaya *et al.*, Phys. Rev. B **58**, 3457 (1998).
- [19] W.N. Hardy *et al.*, in *Proceedings of the 10th Anniversary HTS Workshop*, edited by B. Batlogg *et al.*, World Scientific, Singapore (1996).
- [20] V.G. Kogan, Phys. Rev. B **24**, 1572 (1981); V.G. Kogan, M.M. Fang, and S. Mitra, Phys. Rev. B **38**, R11958 (1988).
- [21] T. Schneider *et al.*, Eur. Phys. J. B **3**, 413 (1998); J. Hofer *et al.*, to appear in Phys. Rev. B.
- [22] M. Willemin *et al.*, Phys. Rev. B **58**, R5940 (1998).
- [23] C. Rossel *et al.*, Rev. Sci. Instrum. **69**, 3199 (1998).
- [24] M. Willemin *et al.*, J. Appl. Phys. **83**, 1163 (1998).
- [25] S. L. Lee *et al.*, Phys. Rev. Lett. **71**, 3862 (1993); U. Welp *et al.*, Phys. Rev. Lett. **76**, 4809 (1996); A. Schilling *et al.*, *Proceedings of the 10th Anniversary HTS Workshop on Physics, Materials and Applications, Houston, Texas, 1996*, edited by B. Batlogg *et al.*, (World Scientific, Singapore, 1996), p.349; A. Schilling *et al.*, Nature (London) **382**, 791 (1996).
- [26] A. Schilling *et al.*, Phys. Rev. B **58**, 11157 (1998).
- [27] M.J.W. Dodgson *et al.*, Phys. Rev. Lett. **80**, 837 (1998).
- [28] A. Schilling and O. Jeandupeux, Phys. Rev. B **52**, 9714 (1995).
- [29] G.M. Zhao *et al.*, Nature **381**, 676 (1996).
- [30] K.-H. Höck, H. Nickisch, and H. Thomas, Helv. Phys. Acta. **56**, 237 (1983).
- [31] M. Marezio *et al.*, Phys. Rev. Lett. **28**, 1390 (1972).
- [32] C. H. Chen *et al.*, Phys. Rev. Lett. **71**, 2461 (1993).
- [33] C. H. Chen *et al.*, Phys. Rev. Lett. **76**, 4042 (1996).
- [34] M. Tokunaga *et al.*, Phys. Rev. B **57**, 5259 (1998).
- [35] H. Kuwahara *et al.*, Science **270**, 961 (1995).
- [36] Y. Tomioka *et al.*, Phys. Rev. Lett. **74**, 5108 (1995).
- [37] V. I. Anisimov *et al.*, Phys. Rev. B **55**, 15494 (1997).
- [38] S. K. Mishra *et al.*, Phys. Rev. B **56**, 2316 (1997).
- [39] L. Sheng *et al.*, Phys. Rev. B **57**, 5265 (1997).
- [40] J. M. Tranquada *et al.*, Nature (London) **375**, 561 (1995).
- [41] H. A. Mook *et al.*, Nature (London) **395**, 580 (1998).
- [42] A. Bianconi *et al.*, Phys. Rev. Lett. **76**, 3412 (1996).
- [43] A. Lanzara *et al.*, Phys. Rev. B **55**, 9120 (1997).
- [44] S. D. Conradson *et al.*, J. Supercond. **10**, 329 (1997).
- [45] J.G. Bednorz and K.A. Müller, Z. Phys. B **64**, 189 (1986).
- [46] B.I. Kochelaev *et al.*, Phys. Rev. B **49**, 13106 (1994).
- [47] A. Shengelaya *et al.*, Phys. Rev. Lett. **77**, 5296 (1996).

12 Surface Physics

T. Greber, R. Holzner, E. Wetli, J. Kröger, P. Schwaller,
J. Wider, H. J. Neff, C. Cepek, W. Auwärter, F. Baumberger, S. Berner,
M. Hoesch, A. Schneider, W. Deichmann, J. Osterwalder

In the surface physics laboratory we study well-defined surfaces of solid materials as well as adsorbed atomic and molecular monolayers and ultrathin films, prepared under ultrahigh-vacuum (UHV) conditions. In order to obtain detailed information on the geometric arrangement of the atoms within the first few monolayers of the surface we apply predominantly electron-based techniques such as x-ray photoelectron diffraction (XPD), medium-energy electron diffraction (MEED), low-energy electron diffraction (LEED), and more recently also scanning-tunneling and atomic force microscopy (STM/AFM - see below). A time-resolved MEED experiment is being developed with a temporal resolution in the picosecond range. Based on a new experimental geometry for XPD, where photoelectron diffraction effects are measured near a node of the photoexcited electron wave, the concept of photoelectron holography is tested as to whether it could finally fulfill its promises as a direct structural technique on surfaces.

Angle-resolved UV photoelectron spectroscopy (ARUPS) gives us access to the electronic band structure of solids and surfaces. Specifically, our experimental setup permits to directly map sections through the Fermi surfaces of such systems, which represent the electronic degrees of freedom relevant for transport properties, magnetic interactions and phase transitions. We could also extend the measuring range of photoemission above the Fermi level to observe thermally excited electrons within the band structure. An important asset of all these experiments is that the same probe (photoemission) gives us structural, electronic and magnetic information, and we can therefore study the interplay between these different degrees of freedom on the same sample.

In a common project with H. Keller we were able to purchase a combined STM/AFM system (Park Scientific) with one measuring head in UHV complementing our electron-scattering based techniques and one head working at ambient pressure serving as a general purpose surface characterization tool for the Physics Department and other interested departments. The UHV head has been mounted on a dedicated UHV chamber which also contains a basic sample preparation facility, and which can eventually be connected to our photoelectron spectrometer. The high efficiency of the vibration isolation of the chamber and the STM head is demonstrated by atomic resolution images on metal surfaces (Ni(111), Au(111)) measured with a turbomolecular pump running. This instrument is now an important element in our pool of surface analytical tools (see section 12.2).

We have continued our collaboration with the surface chemistry group of Prof. J. R. Huber of the Physical Chemistry Department (P. Willmott, H. Manoravi, H. Spillmann, N. Baiker) who have developed excellent thin film preparation capabilities using pulsed reactive crossed-beam laser ablation. They have grown single crystalline films of several materials of high technological relevance ($\text{TiC}_x\text{N}_{1-x}$, GaN, $\text{Ti:Al}_2\text{O}_3$, SiN_x and CN_x), and they were using our photoelectron spectrometer for surface composition analysis and for verifying the crystallinity of their films.

In a new collaboration with Prof. M. Sancrotti (TASC Laboratory of the Istituto Nazionale per la Fisica della Materia, Trieste, Italy) we investigate structural and electronic properties of C_{60} monolayer films on metal surfaces.

12.1 X-ray photoelectron diffraction in the backscattering geometry

The precise knowledge of the adsorption geometry of atoms, molecules and molecular fragments on metal surfaces is one of the keys to understanding the mechanisms of catalytic activity and selectivity. XPD has not been a very fruitful technique for this type of problem, since the strong forward scattering signals of the photoelectrons excited from the adsorbates point into the crystal and therefore cannot be measured. In the course of our study of the oxygen-covered Rh(111) surface we could measure for the first time the weak backscattering signals in adsorbate emission, and we were able to show that these signals are uniquely sensitive to the oxygen bonding distance to the surface and to the bonding site [1]. Fig. 12.1

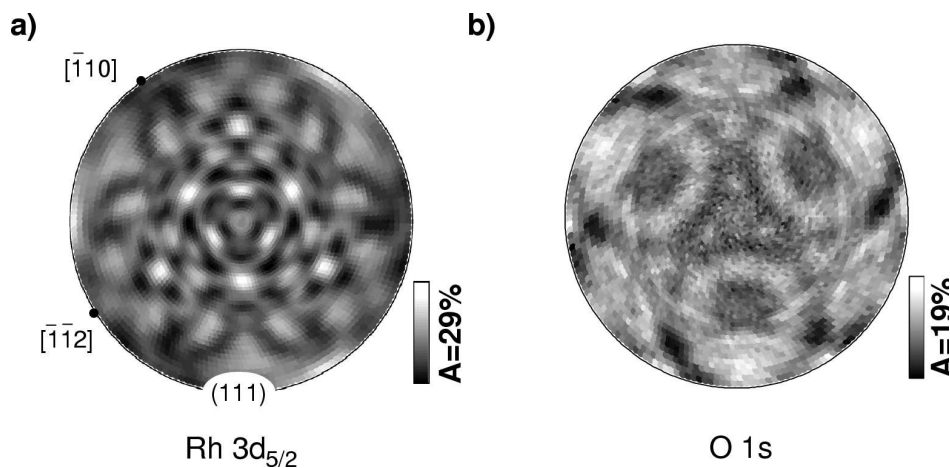


Figure 12.1: Measured photoelectron diffraction patterns a) for Rh $3d_{5/2}$ emission ($E_{kin}=947$ eV) from a clean Rh(111) surface, and b) for O $1s$ emission ($E_{kin}=723$ eV) from a (2×1) -1O/Rh(111) surface. The data are stereographically projected. Intensities are represented in a linear grey scale with grey bars indicating the overall anisotropy $A = (I_{max} - I_{min})/I_{max}$ for each pattern.

shows full XPD patterns of Rh $3d_{5/2}$ substrate emission and of O $1s$ adsorbate emission. The substrate pattern provides the structure and the orientation of the crystal lattice to which the adsorbate structure can be referenced. In the adsorbate pattern the most prominent features are three ring-like structures arranged in a threefold symmetric fashion. They represent circles of constructive interference of electrons emitted from the O atoms directly and electrons backscattered by nearest-neighbour Rh atoms. The centers of the circles are related with the oxygen to rhodium bond directions, while the circle radii are a measure for the bond distance. This is further illustrated in fig. 12.2, where we give single-scattering cluster calculations for O emission using oxygen near-neighbour configurations of different bond lengths and sites. The site is identified immediately by the orientation of the three-circle pattern, while the circles are seen to be very sensitive to changes of 0.1 Å in the adsorption height z_0 . Given the accuracy with which we can measure these backscattering signals we estimate a precision in bond length of ± 0.02 Å.

12.2 Hexagonal boron nitride films on Ni(111)

Metal-insulator-metal structures are very important as tunneling junctions between any combination of normal metals, ferromagnets or superconductors. The ultimate junction is reached with a single monolayer of insulating material. Recently it was discovered that very stable monolayers of hexagonal boron nitride (h -BN) can be prepared by the reaction of benzene-

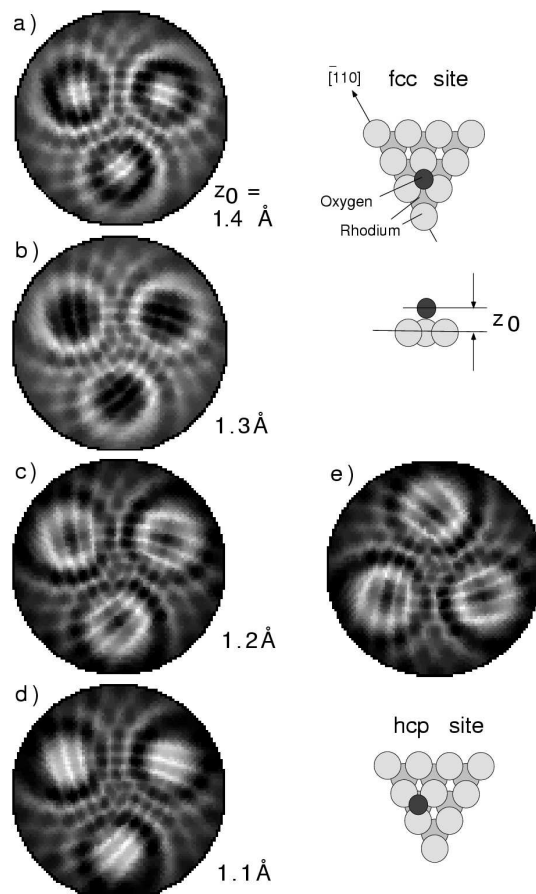


Figure 12.2: XPD single scattering cluster calculations for O 1s emission at $E_{kin}=723$ eV for simple four-atom clusters representing one oxygen atom and three nearest-neighbour Rh atoms forming a threefold hollow adsorption site. In a)-d) the O atom occupies the fcc site at various bond distances (see illustration), while e) shows the adsorption in the hcp site.

like borazine $(\text{BN})_3\text{H}_6$ with Ni(111) at 1100K [2]. With the aim of studying the electronic and magnetic coupling across such films we characterized their growth by XPD and by STM. From the XPD analysis we learn that film growth stops before a second layer starts to form [3]: Strong forward scattering signals in both B 1s and N 1s emission would reveal second layer formation already at the percent level.

Fig. 12.3 shows two STM images of such monolayers recorded in our new UHV-STM chamber. The image (a) shows a wide area scan of $3000 \times 3000 \text{ \AA}$. The film is extremely flat, and the density of monoatomic steps is lower than it was on the Ni(111) substrate before growth, suggesting that the borazine exposure at high temperature induces long range mass transport of Ni atoms flattening the surface. No defects are observed at this scale. The image (b) shows a much smaller area with atomic resolution. A periodic hexagonal pattern with a lattice constant of 2.5 \AA is found, consistent with epitaxial *h*-BN on Ni(111). At this point of our investigation it is not clear which states contribute to the tunneling signal in this image: At the low tunneling voltage (tungsten tip at +4.8 mV) one does not expect to reach electronic states of the boron nitride which has a band gap of 5.2 eV in its bulk form. We may observe tunneling of Ni electrons through this thin insulating barrier, or maybe

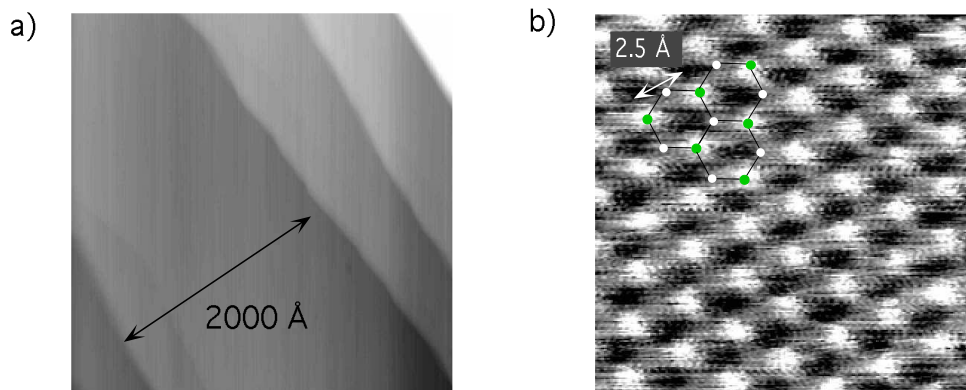


Figure 12.3: *STM images of h-BN on Ni(111): a) large area topography; b) atomic resolution image of h-BN. The overlaid drawing illustrates the structure of this film. We do not yet know which atom within the unit cell causes the bright spots, i.e. the structure model is arbitrarily placed within the image.*

the monolayer of h-BN on Ni(111) is no longer an insulator. This issue is currently under investigation.

We have thus confirmed that these films are not only flat and limited to one monolayer (XPD) but that they are highly contiguous and defect-free. They represent thus an ideal system for studying metal-insulator-metal structures at monolayer definition. Preliminary results show that cobalt can be grown on such films in a wide variety of morphologies, ranging from rather monodisperse small circular clusters to larger flat islands of regular triangular shape and to thick, contiguous films of rather high roughness.

12.3 Time-resolved medium-energy electron diffraction

We are developing an experimental method for obtaining structural information on solid surfaces on a very short time scale. For this purpose, we generate a pulsed electron beam of typically 2 keV energy and measure the angular distribution of the backscattered electrons on a channelplate detector: medium-energy electron diffraction (MEED). The electron pulses are produced by shining femtosecond laser pulses on a photocathode. Considering the electron optical properties of our electron gun we expect electron pulses of a few picoseconds duration [4]. The number of electrons in a single pulse is naturally not sufficient to create a measurable diffraction pattern on the screen, and thus we have to operate the experiment in a pump-probe mode where we periodically prepare the surface in a defined way at a certain time t_0 and have the electron pulse impinge on the surface with a defined delay dt . In order to achieve picosecond resolution in the delay, the preparation step must necessarily be triggered by a laser pulse which is temporally correlated with the probe electron pulse.

A Ti:sapphire laser system in our laboratory produces femtosecond pulses of nanojoule energies at a repetition rate of 80 MHz. This laser works at a wavelength of 800 nm. For the production of the electron pulses at the photocathode we have to double the optical frequency using a nonlinear crystal (BBO). A pulse compression line has been built for higher photoemission efficiency. Using a beam splitter and a computer-controlled optical

delay line we have characterized the pulse width to be 90 fs by refocusing the delayed and undelayed beams onto the Ag photocathode. Ag serves as an autocorrelator because at the work function of 4.3 eV two photons of 3 eV are required for producing a photoelectron.

We have started an investigation of the system Pb/Ge(111). At $1/3$ of a monolayer of Pb this system presents a $(\sqrt{3} \times \sqrt{3}) - R30^\circ$ structure at room temperature. Below 280 K, this surface forms a charge density wave with a (3×3) symmetry [5]. Our aim is to study the dynamics of this charge density wave formation by time-resolved MEED (t-MEED). As a first step, we have to demonstrate that MEED is sufficiently surface sensitive so we can detect signals that are related to the $1/3$ monolayer of Pb. With electron mean free paths of typically 20-40 Å at 2 keV this is by no means easy. In order to enhance the surface signal we have to go to a scattering geometry where the electrons hit the surface at a very shallow angle of less than 5° and measure the scattered electrons also along directions close to the surface. In fig. 12.4 we show a difference image of two MEED patterns, one taken with a $1/3$

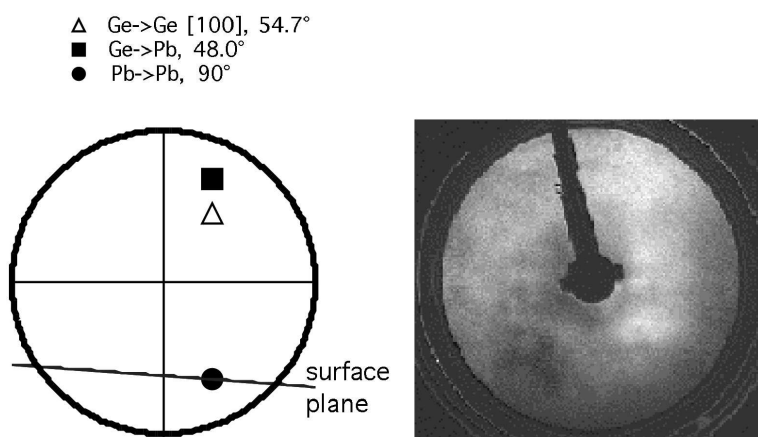


Figure 12.4: *Right: Difference image of two MEED patterns, one measured with $1/3$ monolayer of Pb on Ge(111) and one measured on clean Ge(111). The shadow of the standard LEED electron gun is visible in the center of the plot. Left: Schematic drawing of relevant forward scattering directions as they should appear on the MEED screen. Note that the sample is strongly tilted about a horizontal axis such that the Ge(111) surface plane intersects the screen.*

monolayer of Pb on the Ge(111) surface, and one for the clean Ge(111) surface where the Pb has been removed by heating the crystal. The difference image shows enhanced intensity around positions where forward scattering off Pb atoms is expected to occur (see schematic drawing). While these Pb-related scattering signals are rather weak, it appears that they can be extracted from such difference plots.

12.4 Near-node photoelectron holography

If photoelectron diffraction is measured near a node of the photoelectron source wave the true diffraction intensity is enhanced and holographic interpretation of such data should become feasible [6]. The set up of the new photoelectron diffraction experiment that will meet the requirements for near-node photoelectron holography was further completed (see

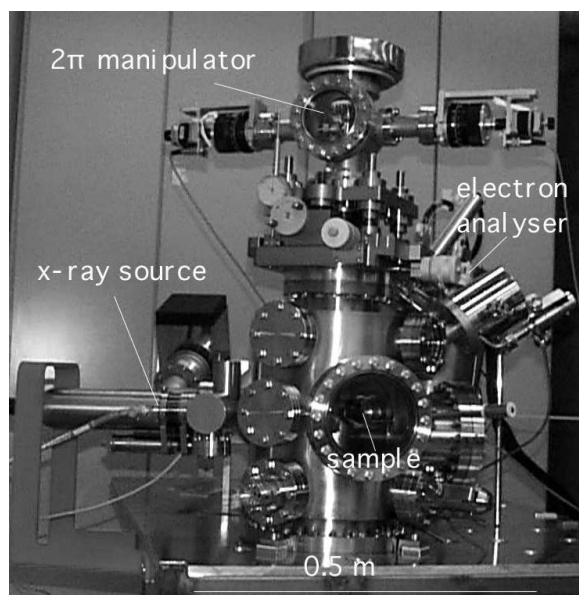


Figure 12.5: Photograph of the near-node photoelectron diffraction experiment as installed in our laboratory.

fig. 12.5). To date the chamber with the collimated (and monochromatized) Al $K\alpha$ x-ray source, the electron analyzer and the home built 2π manipulator that allows the detection of photoelectrons in all directions above the surface are implemented in the experiment. Particular attention has been paid to the cooling of the sample across a sliding contact in our manipulator. We currently reach temperatures below 60 K.

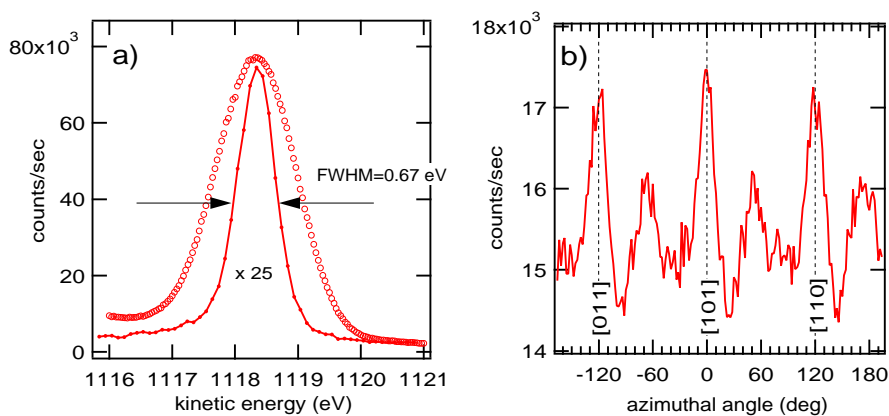


Figure 12.6: First photoemission data from the new experimental setup, recorded from Ag(111). a) Normal emission x-ray photoemission spectrum (XPS) of the Ag $3d_{5/2}$ core level for high energy resolution ($FWHM=500$ meV, dots), and for high transmission (open circles) as used for diffraction experiments. The x-ray power is 600 W, the x-ray angle-of-incidence is 45° relative to the electron detector (standard geometry). b) Ag $3d_{5/2}$ photoemission intensity at 35° polar emission angle as a function of the azimuthal angle. The three prominent peaks correspond to the well-known forward scattering features along the $\langle 110 \rangle$ atomic chains.

In fig. 12.6 first experimental photoelectron data, still recorded in the standard geometry, are shown. Fig. 12.6a depicts an Ag $3d_{5/2}$ core level spectrum from an Ag(111) single crystal surface. In fig. 12.6b an azimuthal diffraction pattern of Ag $3d_{5/2}$ emission at a polar angle of 35° away from the surface normal is shown. The three $\langle 110 \rangle$ -type forward scattering peaks are clearly resolved. After implementation of an electron transfer lens, permitting to have the electron detection direction only 15° away from the x-ray incidence direction, the near-node experiment will be performed.

Recent experiments at the ALOISA beamline at the ELETTRA synchrotron in Trieste allowed us to test the theoretical predictions for the relative enhancement of higher-order diffraction compared to zero-order diffraction, that is forward scattering.

12.5 Photoemission from oriented orbitals

Ultraviolet-excited photoemission is widely used for studying energy levels of molecules and solids. The interpretation of spectra usually takes into account proper initial state wave functions, while little attention has been given to scattering effects in the photoemission final state. Recently, we discovered that, much like in XPD, the intensities of UV-excited spectral features in valence emission from Cu surfaces are dominated by scattering effects in the photoemission final state [7]. Moreover, the angular intensity pattern is found to be very sensitive to the angular momentum of the emitted electrons.

If final state scattering is present in such ultraviolet photoelectron diffraction (UPD) data, they should contain structural information. From their angular momentum sensitivity one can, thanks to the photoemission selection rules, identify the character of the wave functions. We have tested this idea by using a well-characterized molecular adsorbate system: carbon monoxide on Ni(111) [8]. In fig. 12.7 the spectra show Ni $3d$ emission between 38.0 and

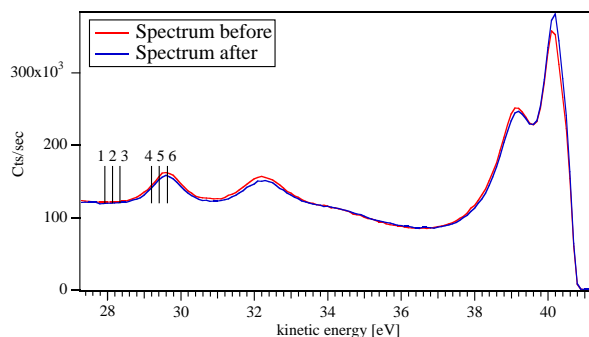


Figure 12.7: *UV photoelectron spectra excited with He II α radiation before and after a one-hour UPD measurement. The positions of the six channeltron detectors used for the data of fig. 12.8 are indicated.*

40.8 eV, while the CO 4σ and 5σ molecular levels appear at kinetic energies of 29.7 and 32.4 eV, respectively. By setting the detectors according to the positions as indicated in the figure we have measured the angular modulation of 4σ emission. After subtracting the corresponding background (detectors 1-3) the patterns as shown in fig. 12.8 are generated for excitation by He II α and He II β radiation.

We use the single scattering theory of XPD as a starting point for the description of these data. While XPD describes emission from core levels situated on a well defined atom, emission from a molecular state has to be viewed as a coherent emission process from two centers. In a linear combination of atomic orbitals (LCAO) picture, the amplitude and phase

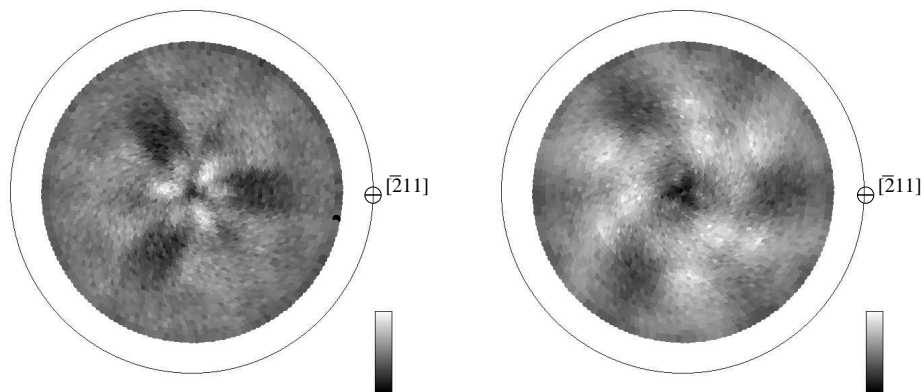


Figure 12.8: *Measured angular distributions of photoelectrons from CO 4σ orbitals on Ni(111) excited with He II α (left) and He II β (right) radiation.*

of each atomic orbital on either the carbon or the oxygen atom needs to be known. The final state scattering of each atomic orbital can be calculated using the single scattering model. From the coherent superposition of all the emission and scattering amplitudes the intensities can be calculated. The results of these calculations for the present case are rather encouraging. For the particular system of CO/Ni(111) we obtain fairly good agreement with experiment for a structure where CO molecules sit upright (carbon down) and preferentially in threefold hollow adsorption sites.

12.6 Photoemission Fermi edge as a thermometer

The temperature of a sample in thermal equilibrium manifests itself in the width of the Fermi edge in photoemission spectra. However, in ARUPS the shape and even the position of the Fermi edge can be markedly changed by Fermi level crossings of bands. The spectrum shown in fig. 12.9b is taken from a clean Ni(111) surface along a direction where the two spin-split d bands ($d\uparrow$ and $d\downarrow$) straddle the Fermi energy [9]. The presence of the $d\downarrow$ band slightly above E_F lifts the tail of the Fermi edge strongly and makes it look shifted to negative binding energies. From measurements of such spectra along many angles we can separate the contributions of the bands and of a featureless background, such as demonstrated in fig. 12.9a. If we now plot the intensity of the background as a function of energy, we recover nice Fermi-Dirac distribution functions centered at the true Fermi level (fig. 12.9b). From these functions, the sample temperature can be fitted to an accuracy of the order of 10 K. The benefit of this procedure is that we obtain a measure of the temperature of the surface under study even in the presence of spacial or temporal temperature gradients.

12.7 Underdoping of Bi-cuprates by ultraviolet radiation

in collaboration with P. Willmott, Physikalische Chemie, Universität Zürich

During our study of the Fermi surface of Bi-type high temperature superconductors at various doping levels we noted that the spectra of optimally doped $\text{Bi}_2\text{Sr}_2\text{CaCu}_2\text{O}_8$ (Bi2212) undergo marked changes when the sample is exposed to the intense ultraviolet radiation of our He discharge lamp. We have characterized these changes very carefully and were able to show that they are associated with radiation-induced oxygen desorption [10]. From measurements of characteristic Fermi surface features it is found that the oxygen desorption causes a decrease

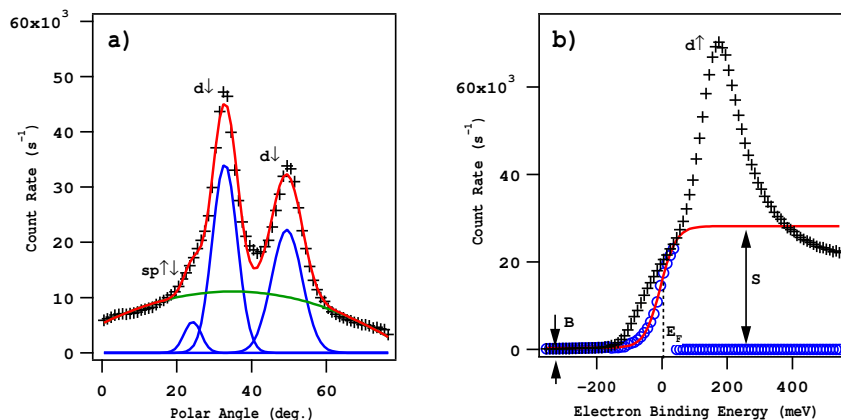


Figure 12.9: a) *He I* excited photoemission intensity at the Fermi level from *Ni(111)* measured as a function of polar emission angle. The crosses show the measured intensities, while the solid lines indicate the Gaussians of the band crossings and the parabolic background function used to fit the measured data. b) (+) photoemission spectrum measured at a polar angle of 40° . (o) intensity of the fitted background (from a)) as a function of binding energy.

of the doping level of the cuprate. The desorption cross sections are strongly dependent on the photon energy: 188 ± 53 kb for *He II* and 23 ± 6 kb for *He I* radiation ($1 \text{ barn} = 10^{-24} \text{ cm}^2$). Two different oxygen desorption channels are inferred from this difference. With *He II* radiation ($h\nu = 40.8 \text{ eV}$) the O $2s$ level can be excited. During the following Auger decay a neutral oxygen species can form which may desorb very effectively, accounting for the strong increase in the desorption cross section.

Attempts to observe the radiation-induced underdoping of thin films of $\text{YBa}_2\text{Cu}_3\text{O}_{6+x}$ in resistivity measurements failed due to the roughness of the prepared films. For these experiments, a versatile UHV-based contact system for four-point resistivity measurements has been developed and successfully tested on a thick $\text{YBa}_2\text{Cu}_3\text{O}_{6+x}$ film.

12.8 Evolution of the Fermi surface in a transition metal film

in collaboration with P. Aebi, Institut de Physique, Université de Fribourg

Magnetic multilayers, i.e. structures of alternating layers of a ferromagnetic and a non-ferromagnetic material are of great technological interest for their strong magnetoresistance effects [11]. The magnetic coupling between the ferromagnetic layers is believed to be strongly influenced by the Fermi surface of the nonmagnetic material [12]. In these models, bulk Fermi surface data are usually the starting point for these considerations. However, since the layers can be only a few atomic layers thick, it is by no means clear whether this assumption is justified.

We studied the evolution of the Fermi surface with layer thickness for the ferromagnetic layer in a film of cobalt on *Cu(111)*. This is one of the prototype magnetic multilayer systems. The growth has been characterized by several groups [13]. The formation of hexagonal close-packed (hcp) Co sets in after 1-3 monolayers (ML) of pseudomorphic growth by introducing more and more stacking faults on the face-centered cubic (fcc) structure of the substrate and the interface. In fig 12.10 a Fermi surface map of clean *Cu(111)* is shown, measured at a photon energy of 21.21 eV. A section through the bulk Fermi surface is seen, intersecting three of the necks of this textbook Fermi surface. In the center of the image, the well-known

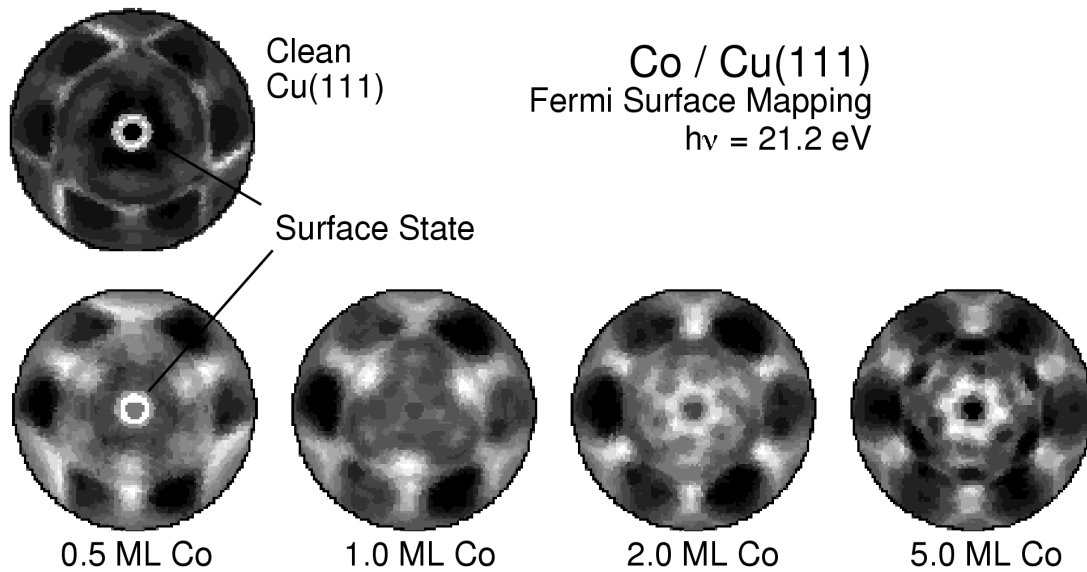


Figure 12.10: *Photoemission Fermi surface maps for clean Cu(111) and Co films of various thicknesses grown on Cu(111), excited with He I α radiation.*

Shockley surface state appears (see next section). Onto this surface, Co films of thicknesses ranging from 0.5 to 5 monolayers have been deposited and characterized by XPD. The Fermi surface maps in fig. 12.10 show that the Cu Fermi surface contours get very diffuse at 0.5 ML, due to the strong scattering of the electrons in the disordered surface layer. The surface state gets completely suppressed at a coverage of 1 ML. At 2 ML, where XPD shows a substantial fraction of stacking faults, i.e. an hcp-like structure, the Fermi surface map approaches a sixfold symmetry. At 5 ML a rather sharp Fermi surface image results. Comparison of this map to Fermi-contours obtained from bandstructure calculations indicates that the Fermi surface has essentially converged to that of bulk cobalt as seen through the (0001) surface. We also measured the energy dispersion of the cobalt bands and find that the Co band structure forms very rapidly, essentially with the first monolayer.

12.9 Surface states on vicinal Cu(111) surfaces

In fig. 12.10 we have seen the Shockley surface state of the clean Cu(111) surface [14] to exhibit a circular Fermi surface centered around normal emission (center of the plot). This state is a consequence of the broken translational symmetry in the normal direction at the crystal surface, and it is located in the band gap of the surface-projected bulk bands. The wave functions propagate parallel to the surface and fall off exponentially both towards the vacuum and towards the bulk and are thus two-dimensional. The circular shape of the Fermi surface and the parabolic dispersion (not shown) indicates that these surface state electrons are free to a good approximation.

Atomic steps on an otherwise flat surface act as scattering centers for surface state electrons. Surfaces that are cut slightly off the Cu(111) planes (vicinal surfaces) exhibit more or less uniform terraces of (111) orientation separated by equidistant steps. We selected Cu(332) and Cu(221) surfaces with terrace geometries as depicted in fig. 12.11 in order to study the influence of the terrace width on the Fermi surface and on the dispersion of the surface state. Fig. 12.12 shows blow-ups of the Fermi surface maps as measured on the three different

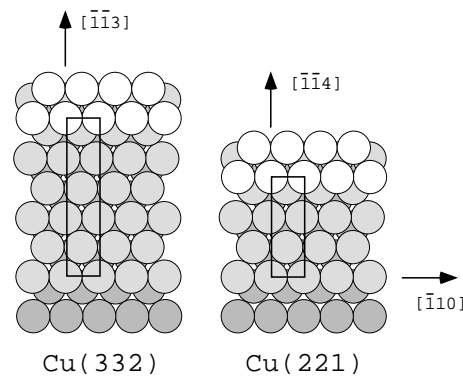


Figure 12.11: *Expected surface atomic configuration for an ideal Cu(332) and Cu(221) surface, respectively. Terrace widths L and miscut angles α are: 12 \AA and 10° for Cu(332), and 7.7 \AA and 15.8° for Cu(221). Primitive surface unit cells are indicated by rectangles. The indicated directions lie in the surface planes.*

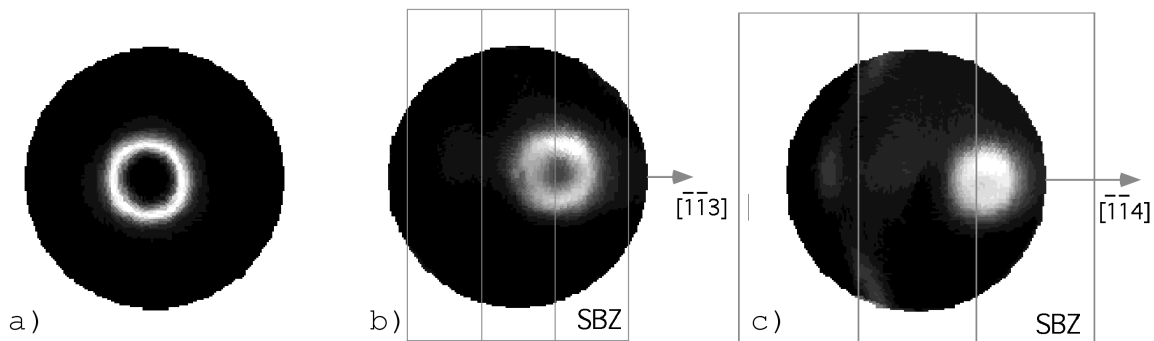


Figure 12.12: *High-resolution He I excited Fermi surface maps of a) Cu(111), b) Cu(332) and c) Cu(221). Surface Brillouin zones are indicated for the stepped samples. The centers of the plots represent emission along the macroscopic surface normal, while the given directions lie in the surface plane and point "up" the steps. The weak feature on the left side in the Cu(221) measurement is due to intersections with the bulk Fermi surface.*

surfaces. We see several things: From carefully fitting the data we find that the surface state Fermi surfaces remain circles for Cu(111) and Cu(221) while for Cu(332) there is a slight deviation. This indicates that the electrons remain nearly free and that no standing waves are formed. The dispersion remains parabolic with slight changes in the effective mass (not shown). The Fermi surfaces of the stepped surfaces move away from the surface normal and along the tilt direction of the local (111) facets. However, the angular displacement is less than the actual tilt; the Fermi surfaces appear to be tied to the boundaries of the surface Brillouin zones. With decreasing terrace length (higher miscut angle) the Fermi surfaces become smaller, i.e. the surface state gets depopulated. From fitting the areas of the Fermi surfaces we find that the population is reduced from 0.07 electrons per Cu surface atom on Cu(111) to 0.02 electrons on Cu(221). This behaviour is in qualitative agreement with a one-dimensional Kronig-Penney model where the steps are represented by a periodic sequence of delta functions. The depopulation is thus a consequence of the electron confinement on the short terraces. At the same time, the Fermi surface contours become broader, which is due to the increased coupling of the surface state wave functions to the bulk states.

12.10 Velocity-selective optical pumping due to back reflection of resonant laser light in a thin sodium vapor cell

On our way to demonstrate beamswitching [15, 16] in a thin sodium vapor cell (sandwich cell) we measured the absorption of laser light resonant to the atomic D_1 transition at 589 nm using the experimental setup shown in fig. 12.13. To our surprise we found the absorption

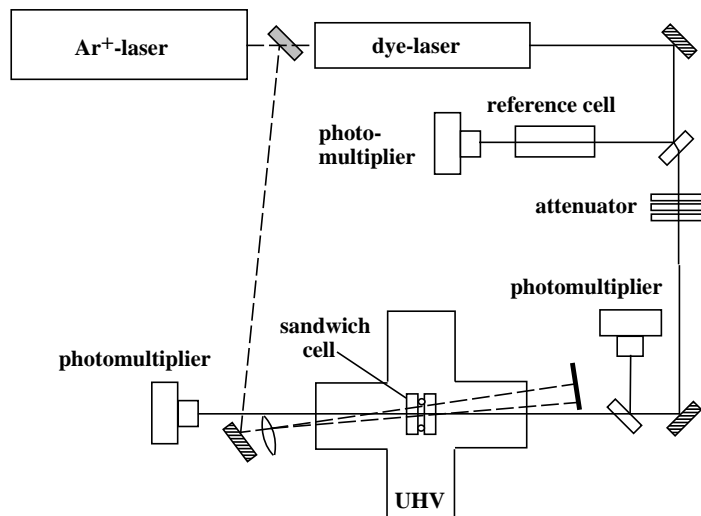


Figure 12.13: *Experimental setup: Beam from the Ar-ion laser (dashed line) evaporates Na in the sandwich cell; resonant beam from the dye laser (full line).*

profile (fig. 12.14) with a very narrow width at exact resonance and without the typical two-bump shape shown by the absorption profile of a reference vapor cell. The explanation for this

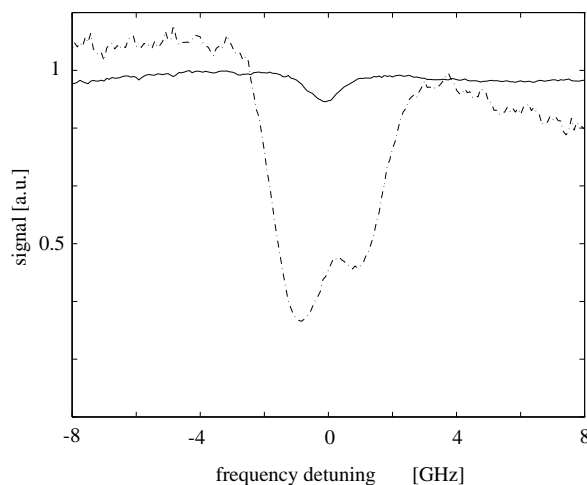


Figure 12.14: *Solid line: transmitted power through the sandwich cell near the D_1 resonance of Na; dash-dotted line: transmitted power through the reference cell.*

unexpected absorption profile is as follows: part of the transmitting beam is backreflected by the surface of the rear window of the thin cell. Therefore atoms with specific velocity components parallel to the direction of the laser beam and the backreflection can be in resonance with both beams but, due to the Doppler shift, with different resonance frequencies defined by the different atomic hyperfine levels. These atoms contribute permanently to the

absorption process and therefore enhance the absorption signal drastically. This explanation is strongly supported by theoretical considerations, previous observations [17] as well as a second experiment (fig. 12.15), where two beams counter-propagating through sodium vapor (produced by an atom dispenser outside the sandwich cell) show the same behavior.

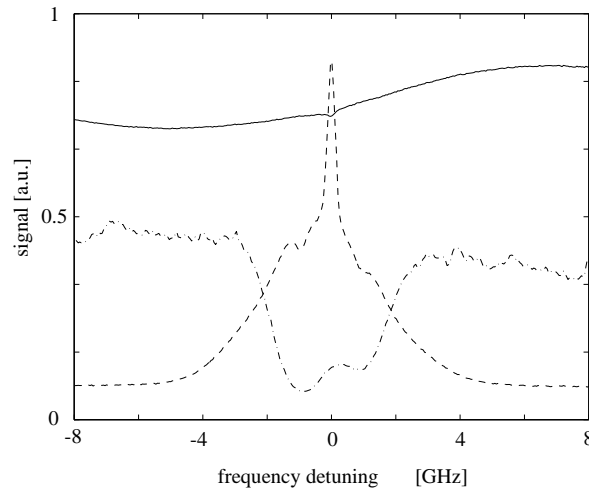


Figure 12.15: *Solid line: absorption profile of one of the two counter-propagating beams; dashed line: fluorescent spectrum perpendicular to the counter-propagating beams; dash-dotted line: transmitted power through the reference cell.*

References

- [1] T. Greber, J. Wider, E. Wetli, J. Osterwalder, *Phys. Rev. Lett.* 81 (1998) 1654.
- [2] A. Nagashima, N. Tejima, Y. Gamou, T. Kawai, C. Oshima, *Phys. Rev. Lett.* 75 (1995) 3918.
- [3] W. Auwärter, T. J. Kreutz, T. Greber, J. Osterwalder, *Surf. Sci.*, in press.
- [4] M. Aeschlimann, E. Hull, J. Cao, C. A. Schmutternmaer, L. G. Jahn, Y. Gao, H. E. Elsayed-Ali, D. A. Mantell, and M. R. Scheinfein, *Rev. Sci. Instrum.* 66 (1995) 1000.
- [5] J. Carpinelli, H. Weitering, E. W. Plummer, R. Stumpf, *Nature* 381 (1996) 498.
- [6] T. Greber, J. Osterwalder, *Chem. Phys. Lett.* 256 (1996) 653.
- [7] J. Osterwalder, T. Greber, P. Aebi, R. Fasel, L. Schlapbach, *Phys. Rev. B* 53 (1996) 10209.
- [8] G. Held, J. Schuler, W. Sklarek, H.-P. Steinrück, *Surf. Sci.* 398 (1998) 154.
- [9] T. Greber, T. J. Kreutz, J. Osterwalder, *Phys. Rev. Lett.* 79 (1997) 4465.
- [10] P. Schwaller, S. Berner, T. Greber, J. Osterwalder, H. Berger, *Appl. Phys. Lett.*, in press.
- [11] G. A. Prinz, *Science* 282 (1999) 1660.
- [12] M. D. Stiles, *Phys. Rev. B* 48 (1993) 7238.
- [13] J. de la Figuera, J. E. Prieto, G. Kostka, S. Müller, C. Ocal, R. Miranda, K. Heinz, *Surf. Sci.* 349 (1996) L139.
- [14] S. D. Kevan, R. H. Gaylord, *Phys. Rev. B* 36 (1987) 5809.

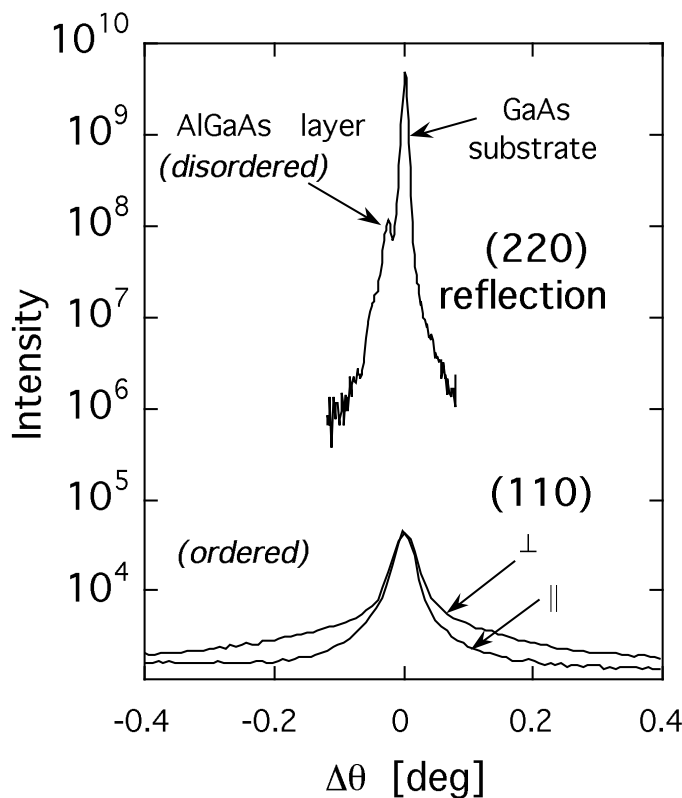
-
- [15] S. Dangel, P. Eschle, B. Röhricht, U. Rusch, H. Schmid, and R. Holzner, *J. Opt. Soc. Am. B* 12 (1995) 681.
- [16] R. Holzner, J. Simonet, L. Flepp, B. Röhricht, P. Eschle, S. Dangel, U. Rusch, H. Schmid, and E. Brun, *Optical Engineering* 34 (1995) 2315.
- [17] S. Nakayama, S. Tsutsumi, *Phys. Lett.* 110A (1985) 368.

13 Spontaneous Ordering in AlGaAs

B.D. Patterson (Univ. Zürich); H. Auderset, C. Brönnimann and U. Staub (PSI); M. Moser, A. Vonlanthen (CSEM), P. Pattison (Univ. Lausanne), K. Knudsen (ESRF) and R. Mathiessen (Univ. Trondheim)

A spontaneous ordering of Al and Ga ions on the group-III sublattice of the compound semiconductor $\text{Al}_x\text{Ga}_{1-x}\text{As}$ has been observed for the first time using X-ray diffraction. The material, with a nominal Al-concentration $x=0.75$, was grown as a 500 nm thick epitaxial layer on a [110] GaAs substrate wafer. High intensity synchrotron radiation was required to observe the very weak superlattice diffraction peaks and to demonstrate a strongly anisotropic diffuse scattering component.

The ternary III-V semiconductor $\text{Al}_x\text{Ga}_{1-x}\text{As}$, grown in the form of epitaxial layers on GaAs substrates, is an important material both from the point of view of fundamental quantum-well physics and in terms of technological applications (e.g., heterostructure transistors and laser diodes). Its usefulness derives from the fact that the aluminum concentration x can be varied continuously between 0 and 1, producing a large shift (87%) in the direct electronic bandgap but a small change (0.14%) in the lattice constant. This allows the growth of elastically-strained epitaxial barrier layers on GaAs substrates. The most common growth techniques are molecular-beam epitaxy (MBE) and organo-metallic vapor phase epitaxy (OMVPE), and the standard substrate orientation is [100].



Due to the similar covalent radii of Al and Ga, it has generally been accepted that $\text{Al}_x\text{Ga}_{1-x}\text{As}$ is a random alloy, with the Al and Ga ions occupying uncorrelated positions on the group-III sublattice of the cubic zincblende structure. In 1985, however, Kuan, et al [1] could observe, using electron diffraction, superlattice reflections in $\text{Al}_{0.75}\text{Ga}_{0.25}\text{As}$ samples grown with OMVPE on [110] substrates. The diffraction pattern implied a weakly developed spontaneous ordering of Al and Ga in the CuAu I structure, with alternating (100) Al- and

Ga-rich atomic planes. Although stimulating much theoretical work, to date no independent observation of this spontaneous ordering has been published.

We have used OMVPE to grow a 500 nm $\text{Al}_{0.75}\text{Ga}_{0.25}\text{As}$ on a [110] GaAs substrate at a growth temperature of 780°C . Upon investigation with 0.7 \AA synchrotron radiation (at the Swiss-Norwegian Beamline of the European Synchrotron Radiation Facility, Grenoble), we observed weak reflections satisfying the selection rule ($h+k=\text{even}$, $k+l=\text{odd}$) specific to the CuAu I structure. The Figure shows the observed diffracted intensity as a function of scattering angle for the zincblende-allowed (220) reflections from the GaAs substrate and the epitaxial layer and for the CuAu I (110) superlattice reflection. The extreme weakness of the superlattice diffraction peak makes the use of high-intensity synchrotron radiation a necessity. The Figure shows (110) diffraction results for both the $\theta(\parallel)$ and $\theta - 2\theta(\perp)$ scanning modes. The former samples reciprocal space parallel to the wafer surface and the latter perpendicular. In spite of the weakness of the signals, one clearly sees a broad diffuse scattering component perpendicular to the surface, indicative of finely-spaced stacking faults running perpendicular to the [110] layer growth direction.

Although this anisotropic diffuse scattering was also seen in the earlier electron diffraction experiment, the present high-resolution X-ray results permit a quantitative evaluation of the stacking fault correlation. It is believed that the long diffuse tails make a substantial contribution to the integrated scattering intensity.

References

- [1] T.S. Kuan, et al, Phys. Rev. Lett. 54, 201 (1985)

14 Computer Assisted Physics

P. F. Meier, S. Dangel, P. Hüsler, H. R. Moser, Y. Shen and J. M. Singer

14.1 Introduction

The Computer Assisted Physics group has continued its research activities in computational physics. Selected examples of progress are presented in the following subsections. They comprise (i) investigations of the electronic structure of materials exhibiting high-temperature superconductivity using large-scale cluster calculations and (ii) Quantum Monte-Carlo calculations of the susceptibilities of the anisotropic antiferromagnetic Heisenberg model. Furthermore, (iii) we report on the activities in the analysis of nonlinear dynamical systems, a project which is pursued in the frame of a collaboration with the department for Neurology of the University Hospital. Finally, (iv) investigations of molecular wave phenomena in porous media, that are performed in collaboration with a private company, are presented.

14.2 Electronic structure calculations of high-temperature superconductors

The electronic structure of high- T_c materials has been investigated with density functional calculations within the local density approximation (LDA) [1]. These calculations do provide information about the ground state charge density distribution and hybridization parameters, but they reproduce neither the semiconducting behavior of La_2CuO_4 nor the magnetic properties of the ground state.

The cluster method supplements the results of band-structure calculations. It has the advantage that correlation effects can - at least in principal - be accounted for by configuration interaction (CI) procedures. Furthermore, it is possible to go beyond LDA by generalized gradient approximations (GGA). The most serious disadvantage is the finite size of the clusters that can numerically be treated. Therefore, the influence of the surrounding ions has to be taken into account by adjusting the correct Madelung potential in the central region of the cluster.

The quality of electronic structure calculations can be tested by studying the electric field gradients (EFGs) at various nuclear sites. The EFGs depend sensitively on the charge distribution and thus provide information about the ground state. Their values have been determined experimentally by NMR and NQR for a variety of nuclei in the high- T_c materials [2].

Theoretical approaches [3, 4] give EFG values that, apart from one exception, more or less agree with the experimental data. The exceptional case is the EFG at the planar Cu(2) site in the $\text{YBa}_2\text{Cu}_3\text{O}_n$ compounds. In the past two years we have applied the cluster approach to study the electronic structure of $\text{YBa}_2\text{Cu}_3\text{O}_7$. The focus was on the evaluation of the EFG's at the Cu sites. Using a rather large cluster (comprising 12 Cu and 42 O, as well as 12 Y and 8 Ba atoms) which was furthermore embedded in a lattice of more than 2000 point charges, we calculated the electronic structure with three different methods: Hartree-Fock (HF), LDA and GGA [5, 6]. For LDA and GGA calculations, the EFGs at the Cu(2) site are much closer to the experimental values ($V_{zz} = 12.3 \times 10^{21} \text{ Vm}^{-2}$) than those obtained with other theoretical approaches [3, 4]. Furthermore, by simulating the change of lattice sites upon applying hydrostatic pressure, we were able to reproduce the measured relative change of the quadrupolar frequency ν_Q which is proportional to V_{zz} rather well as is shown in Fig. 14.1.

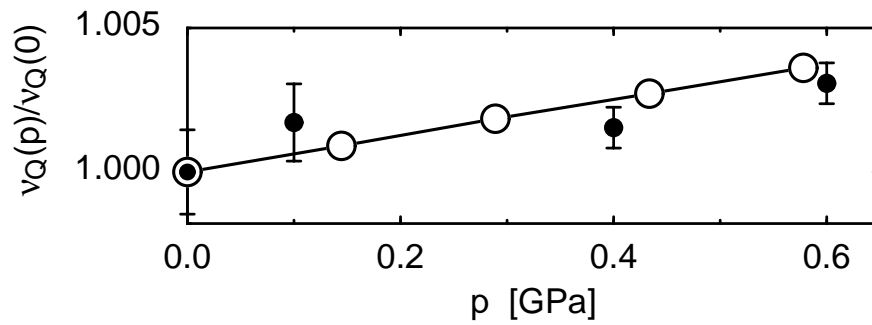


Figure 14.1: Normalized pressure dependent NQR frequencies $\nu_Q(p)/\nu_Q(0)$ for Cu(2) in $\text{YBa}_2\text{Cu}_3\text{O}_7$. ● experiments [7]. ○ our density functional calculations (GGA) [8].

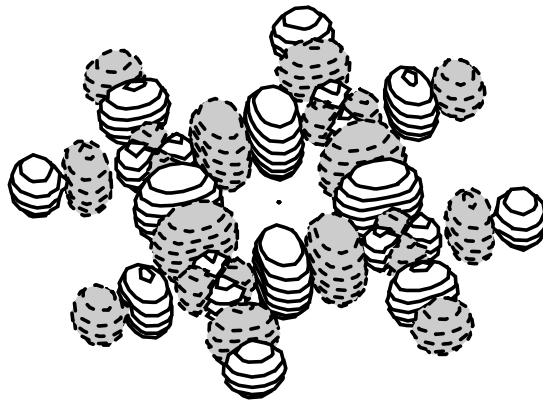


Figure 14.2: Highest occupied molecular orbital in the cluster $\text{Cu}_4\text{O}_{20}/\text{Cu}_8\text{La}_{26}$. The shaded regions indicate negative sign of the corresponding atomic wave functions.

First spin-polarized studies have also been performed for the La_2CuO_4 structure with different clusters: (i) $\text{CuO}_6/\text{Cu}_4\text{La}_{10}$ where one Cu and six O atoms were treated in an all electron basis while for additional 4 Cu and 10 La atoms pseudopotentials were used and (ii) $\text{Cu}_4\text{O}_{20}/\text{Cu}_8\text{La}_{26}$. For the latter, Fig. 14.2 depicts the highest occupied molecular orbit (HOMO) obtained with GGA calculations. There is a strong antibonding hybridization between the Cu $3d_{x^2-y^2}$ (33 %) and the O $2p_x$ and $2p_y$ (67 %) atomic orbitals. The corresponding quadrupole frequencies at the Cu site are given in Table 14.1. Again, the values obtained with the density functional method with GGA compare well with the experimental data.

method	HF	HF	HF	GGA	GGA	
Ref.	[9]	[10]	present	present	present	exp.
cluster	CuO_6	CuO_6	$\text{CuO}_6/\text{Cu}_4\text{La}_{10}$	$\text{CuO}_6/\text{Cu}_4\text{La}_{10}$	$\text{Cu}_4\text{O}_{20}/\text{Cu}_8\text{La}_{26}$	
ν_Q	47	39	48	35	34	33

Table 14.1: ^{63}Cu NQR frequencies (MHz) for La_2CuO_4 .

14.3 Quantum Monte-Carlo simulations of the antiferromagnetic Heisenberg model

Following the discovery of high-temperature superconductors the two-dimensional spin- $\frac{1}{2}$ antiferromagnetic Heisenberg model has received much attention since there are experimental indications that spin dynamics plays an important role in the new superconducting mechanisms. Copper spins in Cu-O planes of the undoped compound La_2CuO_4 exhibit strong two dimensional antiferromagnetic correlation, which is reasonably well described by the Heisenberg model. In this work we have studied one-dimensional antiferromagnetic Heisenberg models over a wide range of anisotropy via a large-scale quantum Monte-Carlo (QMC) simulation [11]. These models are described by the generalised Hamiltonian:

$$\mathcal{H} = J \sum_i \{ S_i^x S_{i+1}^x + S_i^y S_{i+1}^y + a \cdot S_i^z S_{i+1}^z \}, \quad (14.1)$$

where $\vec{S}_i = (S_i^x, S_i^y, S_i^z)$ is the spin operator at the i -th site and the parameter a represents the anisotropy in z -direction. The energy scale is set by the exchange coupling J . In this work we have implemented both the conventional worldline algorithm and the modern loop algorithm [12]. The latter can improve the performance of the QMC simulation by orders of magnitude. Using these methods, we have calculated the finite-temperature susceptibilities shown in Fig. 14.3. Our QMC-results are represented by different symbols, which are connected by dotted lines. The bold solid lines are analytical results for some special cases of the Heisenberg model. We found good agreements between the QMC simulations and the analytical results for $a = 0$ (XY model) and $a = 1$ (isotropic case). In the high-temperature region all $\chi(T)$ -curves converge to the Curie law. The deviations at low temperature indicate the quantum nature of spin- $\frac{1}{2}$ systems. In contrast to other cases, in the Ising-like region ($a > 1$) a finite susceptibility at zero temperature does not exist. This indicates an energy gap between the ground state and excited states which is due to the existence of an anisotropy. The experience gained with the solutions for the one-dimensional system may facilitate the application of the QMC-simulation to two- and three-dimensional systems.

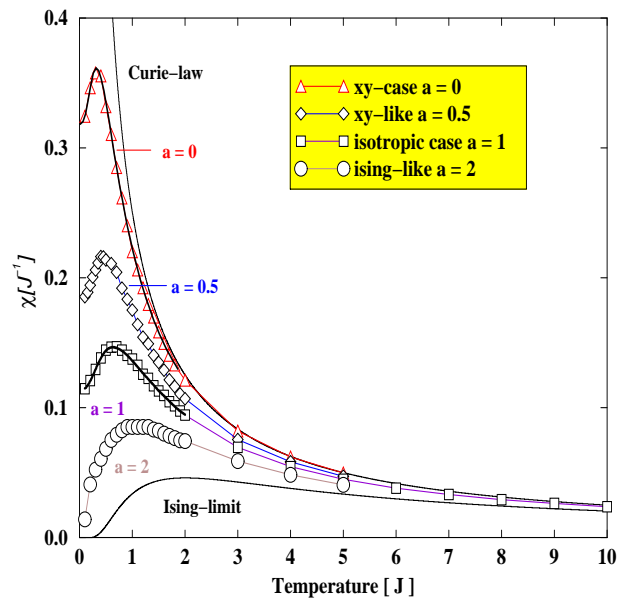


Figure 14.3: Temperature dependence of the susceptibility in the one-dimensional antiferromagnetic Heisenberg model calculated with QMC for various anisotropy values a . The solid lines for $a = 0, 1$, and ∞ (Ising model) are analytical results.

14.4 Electroencephalograms in epilepsy: analysis and seizure prediction within the framework of Lyapunov theory

Epileptic seizures are defined as the clinical manifestation of excessive and hypersynchronous activity of neurons in the cerebral cortex and represent one of the most frequent malfunctions of the human central nervous system. Therefore, the search for precursors and predictors of a seizure is of utmost clinical relevance and may even guide us to a deeper understanding of the seizure generating mechanisms.

It has been known for a long time that seizure prediction cannot be based only on the density of visible epileptiform patterns in the electroencephalogram (EEG). However, some of the analysis methods within the field of nonlinear dynamics are sensitive to "hidden" properties of a signal: There exist chaos-indicators that well have the discrimination power between the so-called preictal signals (i.e., a few minutes prior to a seizure onset) and the interictal ones.

We extracted complexity measures such as Lyapunov exponents and Kolmogorov entropies from intracranial EEGs (invasive and semi-invasive methods) that mainly originate from the group around Prof. H. G. Wieser at the University Hospital Zurich, but also from a group around Prof. C. E. Elger at the University Hospital in Bonn. Among the computational methods we tested so far, we find that the spectral density of the local expansion exponents is best suited to predict the onset of a forthcoming seizure. Our results on this matter are summarized in quite some detail in Ref. [13].

Below we concentrate on a somewhat different issue, namely we aim at a critical assessment of the question whether the deterministic share in an EEG can be quantified. This question is not an easy one, particularly since a high-dimensional noisy time series necessarily must be filtered, which then alters also the underlying "true" signal. We investigated a 64 channel EEG from a subdural 8 by 8 grid-electrode, i.e., a recording technique that generally

provides particularly "clean" and stationary signals. The patient suffers from a so-called frontal lobe epilepsy. We prefer to use multichannel reconstruction, since this type of analysis proves a significantly lower noise sensitivity compared to the delay-embedding technique. Fig. 14.4 displays two Lyapunov spectra, i.e., as many Lyapunov exponents as phase space

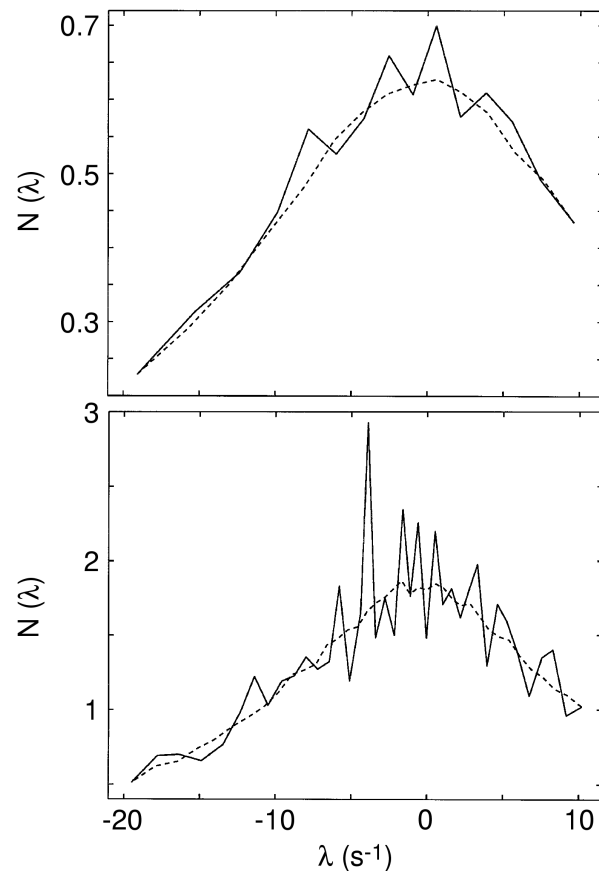


Figure 14.4: Lyapunov spectra, i.e., as many Lyapunov exponents as phase space dimensions, represented as a spectral density. The EEG data originating from an 8 by 8 subdural grid-electrode were used. Top: rows 1 and 2 in the grid, i.e., 16 phase space dimensions. Bottom: rows 1 through 5, i.e., 40 dimensions. We prefer to see $N(\lambda)$ as a dimensionless number of events, although its construction implies units of seconds. For an increasingly large number of phase space dimensions, this representation exhibits the convergence of the Lyapunov spectra.

dimensions, represented as spectral densities. The solid curves are given by the reciprocal distances between adjacent exponents. Clearly such spectra look rather toothed, since a minute variation in the small distances gets strongly amplified in their reciprocal values. The dashed curves emerge from a smoothing procedure based on a "centre of mass"-approach, i.e., the intensities are made up from several Lyapunov exponents used at a time.

A bunch of similar plots reveals that we achieve convergence in the range of, say, 10 up to 12 phase space dimensions. We cannot commit ourselves to an exact number, since this depends somewhat on the applied criteria. In particular, one might focus on the largest and smallest exponents only. The convergence of such spectra is in strict disagreement with a stochastic behavior, thus it exhibits the deterministic properties of the underlying signal.

We are aware that other EEG–recording techniques are attended with much higher noise levels. Nevertheless we think that our results provide an important step towards a quantitatively correct characterization of such signals: Most approaches are based on a given number of phase space dimensions. Therefore it appears desirable to know initially whether the chosen size of the phase space is sufficient.

14.5 Nonlinear wave phenomena in porous media

Recent advances in ultra high sensitive seismic detector technology allow for the direct measurement of even very weak nonlinear seismic signals. The company ADNR Technology Sagl, situated in Minusio, Ticino, has been able to observe such an effect which depends on the fluid saturation of a porous layer. This technology can be used as a direct indicator for oil, gas and water content. Fig. 14.5 shows the spectra of the seismic wave originating from an oil reservoir several km deep as observed at the surface. A peak at about 3 Hz occurs at locations where the oil content is still high, while the signal at depleted locations is flat. ADNR has been able to reproducibly measure this effect and the correlation with the well known oil distribution of the reservoir is very good.

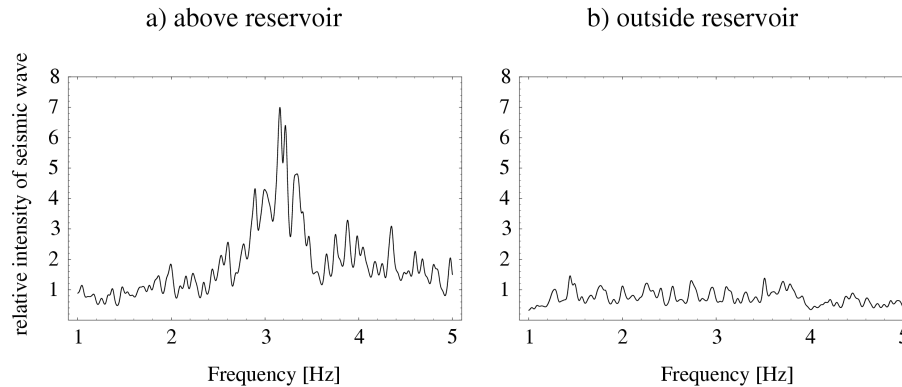


Figure 14.5: Experimental data from an oil field. a) corresponds to a point situated directly above the reservoir. b) corresponds to a point situated outside the border of the reservoir.

To this date there exists no established theory about the origins of this effect. In order to develop a theoretical explanation, we are considering

- autowaves, feedback and memory mechanisms in porous media [14],
- scattering and reflection of waves in layered media [15],
- nonlinear wave propagation mechanisms, wave modulation [16],
- nonlinear oscillations of fluids in porous media [17],
- non-Newtonian fluid flow behavior (thixotropy, Knudsen flow) [18],

Our current model consists of an autowave process based on a nonlinear pore mechanism and driven by global flux in the reservoir. It can explain the occurrence of the low frequency peak, but has not yet been developed far enough to give quantitative results.

References

- [1] for a review, see K. C. Haas, Solid State Physics, Vol. 42 ed. by H. Ehrenreich and D. Turnbull (1989).
- [2] for a review, see D. Brinkmann and M. Mali, in NMR – Basic Principles and Progress, ed. P. Diehl et al., Vol. 31, p 171 (1994).
- [3] K. Schwarz et al., Phys. Rev. B **42**, 2051 (1990).
- [4] N. Sahoo et al., Phys. Rev. B **41**, 220 (1990).
- [5] H. U. Suter, E. P. Stoll, P. Hüsser, S. Schafroth, and P. F. Meier, Physica C, **282-287**, 1639 (1997).
- [6] P. Hüsser, E. Stoll, H. U. Suter, P. F. Meier, Physica C, **294**, 217 (1998).
- [7] K. Müller, M. Mali, J. Roos, and D. Brinkmann, Physica C, **162-164**, 173 (1989).
- [8] P. Hüsser, S. Schafroth, E. Stoll, H. U. Suter, and P. F. Meier, Helv. Phys. Acta, **70**, Separanda 2, S25 (1997).
- [9] S. B. Sulaiman, N. Sahoo, T. P. Das, O. Donzelli, E. Torikai, and K. Nagamine, Phys. Rev. B **44**, 7028 (1991).
- [10] R. L. Martin, Phys. Rev. Lett., **75**, 744 (1995).
- [11] M. S. Makivic and Hong-Qiang Ding, Phys. Rev. B **43**, 3562(1991);
- [12] H.G. Evertz, The Loop Algorithmus. In Numerical Methods for Lattice Quantum Many-Body Problems, D. J. Scalapino, Addison Wesley Longman, Frontiers in Physics.
- [13] H. R. Moser, B. Weber, H. G. Wieser, and P. F. Meier, Physica D, in press.
- [14] V. A. Vasiliev, in *Autowave processes in kinetic systems*. Reidel, 1990.
- [15] L. M. Brekhovskikh and O. A. Godin, *Acoustics of layered media I and II*. Springer, 1990.
- [16] I. Ya. Edelman, Propagation of nonlinear waves in a porous medium with two-phase saturation by a liquid and a gas. *Fluid Dynamics (Moscow)*, **31**, 552, (1996).
- [17] S. Martin, A hydrodynamic curiosity: the salt oscillator. *Geophysical Fluid Dynamics (GB)*, **1**, 143, (1970).
- [18] R. Meyer and F. F. Krause, Experimental evidence for permeability minima at low-velocity gas flow through naturally formed porous media. *J. Porous Media*, **1**, 93, (1998).

15 Electronic

K.Esslinger

In order to study cells of the central nervous system of testpersons at the Neurologische Klinik of the Universitäts-Spital Zürich (NF-Exp. B.Weber), we have successfully modified a commercial stimulus machine (Made in Japan).

For test and control measurements of micro-strip-gas-chambers (MSGC's) at the PSI Villigen (HERA-B Collaboration), we have constructed and built an X-Y position readout system. It consists of two solid-state display units and two low impedance signal outputs (for ADC/PC readout). We have also been asked by the H1 group (Prof. P. Truöl) to help in the realization of the H1 CIP upgrade (new MWPC).

In the report period 1998/99 we have been involved in much modification and repairwork of electronic equipment for different groups at our institute.

15.1 Current Detection Amplifiers for Plasma Traps

We have built eight low noise preamplifiers for the Penning traps to be used in the ATHENA Experiment at CERN (Prof. C. Amsler). The spacial distribution of the positron (or antiproton) plasma will be measured by dumping the charged particle clouds into concentric ring electrodes around the trap axis and by measuring the currents. The amplifiers will be used in spring 1999 for preliminary measurements with an electron plasma. Their main properties are a high input impedance (200 MOhm), very low noise, wide bandwidth and a good linear response.

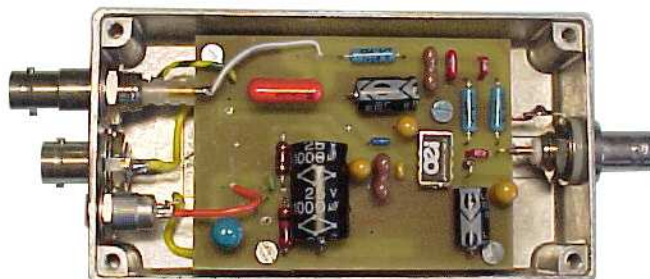


Figure 15.1: *Low Noise Amplifier for the ATHENA apparatus*

16 Publications

16.1 Research group of Prof. C. Amsler

Articles

- Proton-Antiproton Annihilation and Meson Spectroscopy with the Crystal Barrel
C. Amsler
Rev. Mod. Phys. 70 (1998) 1293
- Review of Particle Physics
C. Caso et al. (Particle Data Group)
Eur. Phys. Journal 3 (1998)
- Particle Physics Booklet
C. Caso et al. (Particle Data Group)
Springer (1998)
- Exotic $\eta\pi$ State in $\bar{p}d$ Annihilation at Rest into $\pi^-\pi^0\eta p_{spectator}$
A. Abele et al. (Crystal Barrel Collaboration)
Phys. Lett. B 423 (1998) 175
- $\bar{p}p$ annihilation at rest into $K_L K^\pm \pi^\mp$
A. Abele et al. (Crystal Barrel Collaboration)
Phys. Rev. D 57 (1998) 3860
- Evidence for a $\pi\eta$ -P-wave in $\bar{p}p$ -annihilations at rest into $\pi^0\pi^0\eta$
A. Abele et al. (Crystal Barrel Collaboration)
Phys. Lett. B 446 (1999) 349
- Evidence for $a_0(1450) \rightarrow K\bar{K}$ in $\bar{p}p$ annihilation at rest
M. Heinzlmann
Proc. of Hadron '97 Conf., AIP Conf. Proc. 432 (1998) 95
- Two-body decays of $f_0(1500)$
S. Spanier
Proc. High Energy Physics Conference, Jerusalem, 1997

Articles in press

- Observation of resonances in the reaction $\bar{p}p \rightarrow \pi^0\eta\eta$ at 1.94 GeV/c
A. Abele et al. (Crystal Barrel Collaboration)
Eur. Phys. Journal
- $\bar{p}d$ annihilation at rest into $\pi^+\pi^-\pi^-p_s$
A. Abele et al. (Crystal Barrel Collaboration)
Phys. Lett. B

Conference reports

- Recent results from Crystal Barrel in $K\bar{K}\pi$ and $\omega 4\gamma$
P. Giarritta
Proc. LEAP '98 Conf., Villasimius, Sardinia
- Strangeness Production in Pontecorvo Reactions on Deuterium
C. Regenfus
Proc. LEAP '98 Conf., Villasimius, Sardinia

- Antihydrogen production and precision experiments on trapped cold antihydrogen
C. Regenfus
Proc. Workshop on Exotic atoms, molecules and muon catalyzed fusion, Ascona, Hyperfine Interactions (1998)

Invited Lectures

- C. Amsler
Seminar, Universität Bern, 8.5.98
“Exotic mesons in \bar{p} -nucleon annihilation”
- C. Amsler
Colloque, CEA Saclay, 12.12.98
“Mésons exotiques dans l’annihilation \bar{p} -nucléon”
- C. Amsler
Invited talk, Workshop on Hadron Spectroscopy, Frascati, 12.3.99
“The 1500 - 1700 MeV mass region”
- P. Giarritta
Invited contribution, LEAP '98 Conf., Villasilvius, 9.9.98
“Recent results from Crystal Barrel in $K\bar{K}\pi$ and $\omega 4\gamma$ ”
- R. Kaufmann
Invited contribution, Schweizer-CMS-Vollversammlung, PSI, 8.2.99
“Pixel sensor development: Lorentz angle in irradiated silicon and current design studies”
- F. Ould-Saada
Séminaire, Collège de France, Paris, 23.2.99
“Est-ce que les neutrinos ont des propriétés électromagnétiques?”
- F. Ould-Saada
Seminar, University of Bergen, Norway, 1.3.99
“A story about particles and interactions”
- C. Regenfus
Invited contribution, Workshop on Exotic atoms, molecules and muon catalyzed fusion, Ascona, 24.7.98
“Hydrogen Production and Precision Experiments with ATHENA”
- C. Regenfus
Invited contribution, LEAP '98 Conf., Villasilvius, 10.9.98
“Pontecorvo Reactions with Strangeness Production on Deuterium”

16.2 Research group of Prof. Brinkmann

Articles

- Wide frequency range ^{31}P relaxation in the ionic conductor LiPO_3
S. Berger, J. Roos, A. Zavidonov, and D. Brinkmann
Solid State Nuclear Magnetic Resonance 10 (1998) 197
- Spin Gap, Electronic Crossover, and Charge Density Waves in Y-Ba-Cu-O Superconductors
D. Brinkmann
Zeit. f. Naturforschung 53a (1998) 488

- Evolution of antiferromagnetic short-range order with doping in high- T_c superconductors
A. Yu. Zavidonov and D. Brinkmann
Phys. Rev. B 58 (1998) 12486
- Low energy excitation in the infinite-layer antiferromagnet $\text{Ca}_{0.85}\text{Sr}_{0.15}\text{CuO}_2$
F. Raffa, M. Mali, J. Roos, D. Brinkmann, M. Matsumura, and K. Conder
Phys. Rev. B 58 (1998) 2724
- Mixed Magnetic and Quadrupolar Relaxation in the Presence of a Dominant Static Zeeman Hamiltonian
A. Suter, M. Mali, J. Roos, and D. Brinkmann
J. Phys.: Condensed Matter 10 (1998) 5877
- Isotope dependence of the spin gap in $\text{YBa}_2\text{Cu}_4\text{O}_8$ as determined by Cu NQR relaxation
F. Raffa, T. Ohno, M. Mali, J. Roos, D. Brinkmann, K. Conder, and M. Eremin
Phys. Rev. Lett. 81 (1998) 5912
- ^{31}P NMR relaxation in glassy $0.35\text{LiF} \cdot 0.65\text{LiPO}_3$
S. Berger, J. Roos, A. Yu. Zavidonov, D. Brinkmann
Solid State Ionics 112 (1998) 87
- The Mysterious Spin Gap in High-Temperature Superconductors: New NMR/NQR Studies
D. Brinkmann
Appl. Magn. Reson. 15/2 (1998) 197
- New aspects of NMR studies in solid electrolytes
D. Brinkmann
In: *Solid State Ionics - Science and Technology*, Proc. 6th Asian Conference on Solid State Ionics, New Delhi, India World Scientific (1998) 93
- Interplane electronic spin polarization transfer in the superconducting state of $\text{Y}_2\text{Ba}_4\text{Cu}_7\text{O}_{15}$ as revealed by NQR spin-echo double resonance
A. Suter, M. Mali, J. Roos, and D. Brinkmann
Phys. Rev. Lett. 82 (1999) 1309

Articles in press

- Experimental evidence for fast cluster formation of chain oxygen vacancies in $\text{YBa}_2\text{Cu}_3\text{O}_{7-\delta}$ being at the origin of the fishtail anomaly
Andreas Erb, Alfred A. Manuel, Marc Dhalle, Frank Marti, Jean-Yves Genoud, Bernard Revaz, Alain Junod, Dharmavaram Vasumathi, Shoji Ishibashi, Abhay Shukla, Eric Walker, Øystein Fischer, René Flükiger, Riccardo Pozzi, Mihael Mali, and Detlef Brinkmann
Phys. Rev. Lett.
- Temperature dependence of the sublattice magnetization of the antiferromagnetic state in high- T_c parent compounds
M. Matsumura, F. Raffa, and D. Brinkmann
Phys. Rev. B

- Temperature dependence of the sublattice magnetization of the antiferromagnetic state in high- T_c parent compounds
M. Matsumura, F. Raffa, and D. Brinkmann
Phys. Rev. B
- Spin and Charge Dynamics in the Cu-O Chains of $\text{YBa}_2\text{Cu}_4\text{O}_8$
F. Raffa, M. Mali, A. Suter, A. Yu. Zavidonov, J. Roos, D. Brinkmann, and K. Conder
Phys. Rev. B
- Spin dynamics in the paramagnetic phase of $\text{YBa}_2\text{Cu}_3\text{O}_{6.12}$ as seen by Cu NMR
R. Pozzi, M. Mali, and D. Brinkmann, A. Erb and R. Flükiger
Phys. Rev. B

Conference reports

- ^{31}P MAS studies of superionic $x\text{LiF}\cdot(1-x)\text{LiPO}_3$ glasses
S. Berger, M. Foglia, J. Roos, and D. Brinkmann
Joint 28th AMPERE - 13th ISMAR Conference, Berlin, August 2-7, 1998
- High-Pressure NMR in the infinite-layer antiferromagnet $\text{Ca}_{0.85}\text{Sr}_{0.15}\text{CuO}_2$
M. Igarashi, U. Lehmann, M. Mali, J. Roos, and D. Brinkmann
Joint 28th AMPERE - 13th ISMAR Conference, Berlin, August 2-7, 1998
- NMR in metals at high pressure
J. Roos
Workshop: *NMR in Electronic Conductors*, Mijoux (France), September 20 - 24, 1998
- Isotope dependence of the spin gap in $\text{YBa}_2\text{Cu}_4\text{O}_8$ as determined by ^{63}Cu NQR spin-lattice relaxation
F. Raffa, T. Ohno, M. Mali, J. Roos, D. Brinkmann, K. Conder, and M. Eremin
Colloquium on *Magnetic Resonance in High- T_c Superconductors*, Engelberg, January 17 - 21, 1999
- Luttinger liquid and magnetic properties of chains in high- T_c superconductors
A. Yu. Zavidonov
Colloquium on *Magnetic Resonance in High- T_c Superconductors*, Engelberg, January 17 - 21, 1999
- Interplane electronic spin polarization transfer in the superconducting state of $\text{Y}_2\text{Ba}_4\text{Cu}_7\text{O}_{15}$ as revealed by NQR spin-echo double resonance
A. Suter, M. Mali, J. Roos, and D. Brinkmann
Colloquium on *Magnetic Resonance in High- T_c Superconductors*, Engelberg, January 17 - 21, 1999
- Some features of coexistence superconductivity and CDW in bilayered cuprates
I.A. Larionov and M.V. Eremin
Colloquium on *Magnetic Resonance in High- T_c Superconductors*, Engelberg, January 17 - 21, 1999
- Magnetic properties of the bilayered antiferromagnet $\text{YBa}_2\text{Cu}_3\text{O}_{6.12}$ in the paramagnetic phase observed by Cu NMR
R. Pozzi, M. Mali, and D. Brinkmann

Colloquium on *Magnetic Resonance in High- T_c Superconductors*, Engelberg, January 17 - 21, 1999

Invited Lectures

- D. Brinkmann
The mysterious spin-gap in high-temperature superconductors
Congress AMPERE, Berlin, 2 - 7 August, 1998
- D. Brinkmann
Eight lectures on “NMR studies in superionic conductors, metals, antiferromagnets, and high-temperature superconductors”
delivered as Pandit Jawaharlal Nehru Chair Professor,
Dept. of Physics, University of Hyderabad, India, August 1998
- D. Brinkmann
Nine lectures on “NMR in solids”
delivered as Visiting Professor
Dept. of Physics, Indian Institute of Sciences, Bangalore, India, September 1998
- D. Brinkmann
Antiferromagnetic parent compounds of high- T_c superconductors
Dept. of Physics, Indian Institute of Technology, Madras, 14 September 1998
- D. Brinkmann
From antiferromagnets to high- T_c superconductors
Symposium “Correlated Electron Systems and Quantum Magnetism”
Indian Institute of Sciences, Bangalore, 14 - 16 September 1998
- D. Brinkmann
New aspects of NMR studies in solid electrolytes
6th Asian Conference on Solid State Ionics, New Delhi, India 29 Nov. - 4 Dec. 1998
- D. Brinkmann
The various energy gaps and the problem of interplanar coupling in high-temperature superconductors
Colloquium, Institute of Physics, Bhubaneswar (India), 7 Dec. 1998
- D. Brinkmann
The various energy gaps and the problem of interplanar coupling in high-temperature superconductors
Colloquium, Saha Institute of Nuclear Physics, Calcutta, 9 Dec. 1998
- D. Brinkmann
Knight shift and self-diffusion in alkali metals at high pressure
Seminar, Saha Institute of Nuclear Physics, Calcutta, 10 Dec. 1998
- D. Brinkmann
How to study problems in solid state physics by NMR
10. Edgar Lüscher Seminar 1999
Klosters-Serneus, 6-11 February 1999

- D. Brinkmann
Controversial topics in high-temperature superconductors: opinions of an NMR/NQR fan
Colloquium, City University of New York, 9 March 1999
- D. Brinkmann
The origin of the spin-gap and the interplane coupling in cuprate superconductors: new insights by NMR
Colloquium, State University of New York at Albany, 12 March 1999

16.3 Research group of Prof. R. Engfer

Articles

- Improved limit on the branching ratio of $\mu^- \rightarrow e^+$ conversion on titanium
J. Kaulard, C. Dohmen, H. Haan, W. Honecker, D. Junker, G. Otter, S. Starlinger, P. Wintz, J. Hofmann, W. Bertl, J. Egger, B. Krause, S. Eggli, R. Engfer, Ch. Findeisen, E.A. Hermes, T. Kozlowski, C.B. Niebuhr, M. Rutsche, H.S. Pruys, A. van der Schaaf
Physics Letters B 422 (1998)334-338
- The large, low mass Al-CFC-Aramid compound vacuum chamber for the Sindrum II $\mu - e$ -experiment at PSI (design, testing and operation)
Ermin A. Hermes, Felix Rosenbaum, Heinz Peter Wintz
Nucl. Instr. and Methods in Phys. Research A 413(1998)185-190
- New Bounds from a Search for Muonium to Antimuonium Conversion
L. Willmann, P.V. Schmidt, H.P. Wirtz, R. Abela, V. Baranov, J. Bagaturia, W. Bertl, R. Engfer, A. Großmann, V.W. Hughes, K. Jungmann, V. Karpuchin, I. Kisel, A. Korenchenko, S. Korenchenko, N. Kravchuk, N. Kuchinsky, A. Leuschner, V. Meyer, J. Merkel, A. Moiseenko, D. Mzavia, G. zu Putlitz, W. Reichart, I. Reinhard, D. Renker, T.Sakhelashvilli, K. Träger, and H.K. Walter
Phys. Rev. Letters 82(1999)49-52

Articles in press

- Search for $\mu^- \rightarrow e^-$ Conversion on Titanium
S. Eggli, R. Engfer, Ch. Findeisen, E.A. Hermes, T. Kozlowski, F. Muheim, C.B. Niebuhr, H.S. Pruys, M. Rutsche, A. van der Schaaf, W. Bertl, J. Egger, B. Krause, J. Hofmann, S. Playfer, V. Djordjadze, C. Dohmen, W. Honecker, J. Kaulard, G. Otter, A. Schüngel, S. Starlinger, and P. Wintz
Phys. Rev. C 1999 to be published

Conference reports

- Georg Kurz
Search for muon-electron conversion with SINDRUM II
WEIN 98, Santa Fe NM, June 1998.

Invited Lectures

- A. van der Schaaf
Low-energy Signals from Supersymmetry
Summer School on Hidden Symmetries and Higgs Phenomena, Zuoz, August 16 -22,

1998, PSI-Proceedings 98-0

- E.A. Hermes
Regulation mechanisms of environment, culture, civilisation, economy and politics in context with a balanced-education-system
Univ. Tbilisi 2.Sept. 1998, to be publ. Bulletin Georgian Acad. of Sciences

16.4 Research group of Prof. H. Keller

Articles

- Ratio of small polarons to free carriers in $\text{La}_{2-x}\text{Sr}_x\text{CuO}_4$ from susceptibility measurements
K.A. Müller, Guo-meng Zhao, K. Conder, and H. Keller
J. Phys.: Condens. Matter **10**, 291-296 (1998).
- Large, small and especially Jahn-Teller polarons
K.A. Müller
J. Supercond. **12**, 3-7 (1999).
- Observation of vortex-lattice melting in twinned $\text{YBa}_2\text{Cu}_3\text{O}_{7-x}$ using neutron small angle scattering
C.M. Aegerter, S.T. Johnson, W.J. Nuttall, S.H. Lloyd, M.T. Wylie, M.P. Nutley, E.M. Forgan, R. Cubitt, S.L. Lee, D. McK. Paul, M. Yethiraj, and H. A. Mook
Phys. Rev. B **57**, 14511-14516 (1998).
- Evidence for self-organised criticality in the Bean critical state
C.M. Aegerter
Phys. Rev. E **58**, 1438-1441 (1998).
- Evidence for a square vortex lattice in Sr_2RuO_4 by muon-spin rotation measurements
C.M. Aegerter, S.H. Lloyd, C. Ager, S.L. Lee, S. Romer, H. Keller, and E.M. Forgan
J. Phys. Cond. Mat. **10**, 7445-7451 (1998).
- Observation of a square flux line lattice in the unconventional superconductor Sr_2RuO_4
T.M. Riseman, P.G. Kealey, E.M. Forgan, A.P. Mackenzie, L. Galvin, A.W. Tyler, S.L. Lee, C. Ager, D. McK. Paul, C.M. Aegerter, R. Cubitt, Y. Maeno, Z. Mao, and Y. Mori
Nature **396**, 242-244 (1998).
- Observations of suppression of static and dynamic disorder in $\text{Bi}_2\text{Sr}_2\text{CaCu}_2\text{O}_{8+\delta}$ crystals by columnar defects
S.L. Lee, C.M. Aegerter, S.H. Lloyd, E.M. Forgan, M.B. Hunt, H. Keller, I.M. Savić, R. Cubitt, G. Wirth, K. Kadowaki, and N. Koshizuka
Phys. Rev. Lett. **81**, 5209-5212 (1998).
- Torsion cantilever as magnetic torque sensor
C. Rossel, M. Willemin, A. Gasser, H. Rothuizen, G.I. Meijer, and H. Keller
Rev. Sci. Instrum. **69**, 3199-3203 (1998).
- Transition from dimerization to antiferromagnetic order in quasi-one-dimensional $\text{Ca}_{0.83}\text{CuO}_2$
G.I. Meijer, C. Rossel, E.M. Kopnin, M. Willemin, J. Karpinski, H. Schwer, K. Conder,

and P. Wachter

Europhys. Lett. **42**, 339-344 (1998).

- Strong shift of the irreversibility line in high- T_c superconductors upon vortex shaking with an oscillating magnetic field
M. Willemin, C. Rossel, J. Hofer, H. Keller, A. Erb, and E. Walker
Phys. Rev. B **58**, R5940-R5943 (1998).
- First-order vortex-lattice melting transition in $\text{YBa}_2\text{Cu}_3\text{O}_{7-\delta}$ near the critical temperature detected by magnetic torque
M. Willemin, A. Schilling, H. Keller, C. Rossel, J. Hofer, U. Welp, W.K. Kwok, R.J. Olson, and G.W. Crabtree
Phys. Rev. Lett. **81**, 4236-4239 (1998).
- Anisotropy scaling close to the ab -plane in $\text{La}_{1.9}\text{Sr}_{0.1}\text{CuO}_4$ by torque magnetometry
M. Willemin, C. Rossel, J. Hofer, H. Keller, and A. Revcolevschi
Phys. Rev. B **59**, R717-R720 (1999).
- Angular dependence of the latent heat of vortex-lattice melting in untwinned $\text{YBa}_2\text{Cu}_3\text{O}_{7-\delta}$
A. Schilling, R.A. Fisher, N.E. Phillips, U. Welp, W.K. Kwok, and G.W. Crabtree
Phys. Rev. B **58**, 11157-11160 (1998).
- Doping dependence of superconducting parameters in $\text{HgBa}_2\text{CuO}_{4+\delta}$ single crystals
J. Hofer, J. Karpinski, Guo-meng Zhao, M. Willemin, G.I. Meijer, E.M. Kopnin, R. Molinski, H. Schwer, C. Rossel, and H. Keller
J. Supercond. **12**, 45-47 (1999).
- Universal scaling properties of extreme type-II superconductors in magnetic fields
T. Schneider, J. Hofer, M. Willemin, J.M. Singer, and H. Keller
Eur. Phys. J. B **3**, 413-416 (1998).
- Single crystals of $\text{HgBa}_2\text{Ca}_{n-1}\text{Cu}_n\text{O}_{2n+2+\delta}$ ($n=1-5$) and layers of $\text{HgBa}_2\text{Cu}_n\text{O}_4$ grown at gas pressure 10 kbar
J. Karpinski, H. Schwer, E. Kopnin, R. Molinski, G.I. Meijer, K. Conder, J. Hofer, and D. Zech
J. Supercond. **11**, 119-122 (1998).
- High pressure crystal growth and properties of Hg-superconductors and quasi-one-dimensional cuprates
J. Karpinski, H. Schwer, R. Molinski, G.I. Meijer, E. Kopnin, M. Angst, S. Büchi, J. Hofer, V. Alyoshin, R. Puzniak, and A. Wisniewski
in: *High-Temperature Superconductors and Novel Inorganic Materials*, ed. J. Van Tendeloo *et al.*, Vol. **62** (Kluwer Academic Publishers, 1999) (pp. 21-26).
- Spontaneous magnetization and antiferromagnetic correlations of the CuO_2 chains in $\text{Sr}_{0.73}\text{CuO}_2$
A. Shengelaya, G.I. Meijer, J. Karpinski, Guo-meng Zhao, H. Schwer, E.M. Kopnin, C. Rossel, and H. Keller
Phys. Rev. Lett. **80**, 3626-3629 (1998).
- Muon-spin-rotation measurements of the penetration depth in $\text{YBa}_2\text{Cu}_4\text{O}_8$ family superconductors
A. Shengelaya, C.M. Aegerter, S. Romer, H. Keller, P.W. Klamut, R. Dybzinski,

- B. Dabrowski, J. Klamut, and D. Kaczorowski, and I. M. Savić
Phys. Rev. B **58**, 3457-3461 (1998).
- Electron spin-lattice relaxation of Er^{3+} ions in $\text{Y}_{0.99}\text{Er}_{0.01}\text{Ba}_2\text{Cu}_3\text{O}_x$
V.A. Ivanshin, M.R. Gafurov, I.N. Kurkin, S.P. Kurzin, A. Shengelaya, H. Keller, and M. Gutmann
Physica C **307**, 61-66 (1998).
 - Oxygen isotope effects in $(\text{La}_{0.5}\text{Nd}_{0.5})_{0.67}\text{Ca}_{0.33}\text{MnO}_3$: Relevance of the electron-phonon interaction to the phase segregation
M. R. Ibarra, G.M. Zhao, J.M. De Teresa, B. García-Landa, Z. Arnold, C. Marquina, P.A. Algarabel, H. Keller, and C. Ritter
Phys. Rev. B **57**, 7446-7449 (1998).
 - Colossal oxygen isotope shift of the charge-ordering transition in $\text{Nd}_{0.5}\text{Sr}_{0.5}\text{MnO}_3$
G.M. Zhao, K. Ghosh, and R.L. Greene
J. Phys.: Condens. Matter **10** L737-742 (1998).
 - Oxygen isotope effects in $\text{La}_{2-x}\text{Sr}_x\text{CuO}_4$: Evidence for polaronic charge carriers and their condensation
G.M. Zhao, K. Conder, H. Keller, and K.A. Müller
J. Phys.: Condens. Matter **10** 9055-9066 (1998).
 - Very strong magnetic field dependence of the oxygen isotope shift of the charge-ordering transition in $\text{La}_{0.5}\text{Ca}_{0.5}\text{MnO}_3$
G.M. Zhao, K. Ghosh, H. Keller, and R.L. Greene
Phys. Rev. B **59**, 81-84 (1999).
 - Normal-state gap, supercarrier mass anisotropy and isotope effects in $\text{La}_{2-x}\text{Sr}_x\text{CuO}_4$
G.M. Zhao, K. Conder, H. Keller, and K.A. Müller
J. Supercond. **12**, 41-44 (1999).

Articles in press

- Fluxoids and neutron polarisation effects
E.M. Forgan, P.G. Kealey, T.M. Riseman, S.L. Lee, D. McK. Paul, C.M. Aegerter, R. Cubitt, P. Schleger, S.T. Johnson, A. Pautrat, and Ch. Simon
accepted for publication in Physica B (1998).
- Temperature dependence of muon spin relaxation in $\text{Pr}_{1/2}\text{Sr}_{1/2}\text{MnO}_3$
R.I. Grynspan, I.M. Savić, S. Romer, X. Wan, J. Fenichel, C.M. Aegerter, H. Keller, D.R. Noakes, C.E. Stronach, A. Maignan, C. Martin, and B. Raveau
accepted for publication in Physica B (1998).
- Stability of the vortex lattice in ET superconductors studied by μSR
S.J. Blundell, S.L. Lee, F.L. Pratt, C.M. Aegerter, Th. Jestädt, B.W. Lovett, C. Ager, T. Sasaki, V.N. Laukhin, E.M. Forgan, and W. Hayes
accepted for publication in Synth. Met. (1998).
- Flux-line lattice structure in untwinned $\text{YBa}_2\text{Cu}_3\text{O}_{7-x}$
S.T. Johnson, E.M. Forgan, S.H. Lloyd, C.M. Aegerter, S.L. Lee, R. Cubitt, P.G. Kealey, C. Ager, S. Tajima, A. Rykov, and D. McK. Paul
accepted for publication in Phys. Rev. Lett.

- Microfabricated ultrasensitive piezoresistive cantilevers for torque magnetometry
J. Brugger, M. Despont, C. Rossel, H. Rothuizen, P. Vettiger, and M. Willemin
Invited paper, to appear in the *Transducers'97 special volumes of Sensors and Actuators*, Elsevier Science.
- Specific heat of $\text{YBa}_2\text{Cu}_3\text{O}_{7-\delta}$ and $(\text{La}_{2-x}\text{Sr}_x)\text{CuO}_4$: Evidence for d-wave pairing
N.E. Phillips, B. Buffetau, R. Calemczuk, K.W. Dennis, J.P. Emerson, R.A. Fisher, J.E. Gordon, T.E. Hargreaves, C. Marcenat, R.W. McCallum, A.S. O'Connor, A. Schilling, B.F. Woodfield, and D.A. Wright
to appear in *J. Superconductivity*.
- Calorimetric study of the transitions between the different vortex states in $\text{YBa}_2\text{Cu}_3\text{O}_7$
F. Bouquet, C. Marcenat, R. Calemczuk, A. Erb, A. Junod, M. Roulin, U. Welp, W.K. Kwok, G.W. Crabtree, N.E. Phillips, R.A. Fisher, and A. Schilling
to appear in *Physica C*.
- High pressure crystal growth and properties of Hg-based superconductors and one-dimensional $\text{A}_{1-x}\text{CuO}_2$ (A=Sr,Ca,Ba) cuprates
J. Karpinski, G.I. Meijer, H. Schwer, R. Molinski, E. Kopnin, M. Angst, A. Wisniewski, R. Puzniak, J. Hofer, and C. Rossel
in: *Proceedings of the 2nd Polish-US Conference "Recent Developments in High Temperature Superconductivity"*, Karpacz, Poland, 1998, to be published in *Lecture Notes in Physics*, ed. J. Klamut *et al.*, Springer Verlag.
- ESR study on high oxygen pressure synthesized compound $\text{Pr}_{2-x}\text{Gd}_x\text{CuO}_4$
V. A. Ivashin, G.V. Mamin, A. Shengelaya, H. Keller, P.W. Klamut, and A. Sikora
to appear in *Solid State Commun.*
- Oxygen isotope effects in manganites: Evidence for (bi)polaronic charge carriers
G.M. Zhao, H. Keller, R.L. Greene, and K.A. Müller
in *Physics of Manganites*, eds. A. Kaplan and S.D. Mahanti (Plenum Publishing Corporation, 1999).

Conference reports

- What can superconductors teach us about (models of) biology?
C.M. Aegerter
ISTAS Summer School on Biophysics: 'Self-Assembly and Evolution', Lisbon, Portugal, 9-21 March, 1998.
- Fractal structures of flux distributions in superconductors?
C.M. Aegerter
Gordon Research Conference on Fractals, Il Ciocco, Italy, 10-15 May, 1998.
- Investigating low κ superconductors with μSR and SANS
C.M. Aegerter, S.H. Lloyd, E.M. Forgan, P.G. Kealey, S.L. Lee, C. Ager, F.Y. Ogrin, R. Cubitt, W.J. Nuttall, T.M. Riseman, and H. Keller
NATO Advanced Study Institute on Muon Science, St. Andrews, Scotland, 14-29 August, 1998.
- Large modification of the irreversibility line by vortex shaking
M. Willemin, C. Rossel, A. Schilling, J. Hofer, H. Keller, A. Erb, E. Walker, U. Welp,

W.K. Kwok, and G.W. Crabtree

17th General Conference of the Condensed Matter Division, European Physical Society, Grenoble, France, 25-29 August, 1998.

- Separation of the irreversibility line from the first-order melting line in $\text{YBa}_2\text{Cu}_3\text{O}_7$ by an oscillating magnetic field
M. Willemin, C. Rossel, A. Schilling, J. Hofer, and H. Keller
Swiss Physical Society Meeting, Bern, 25-26 February, 1999.
- Anisotropic latent heat of vortex-lattice melting in untwinned $\text{YBa}_2\text{Cu}_3\text{O}_{7-x}$
A. Schilling, R.A. Fisher, N.E. Phillips, U. Welp, W.K. Kwok, and G.W. Crabtree
1998 March Meeting of The American Physical Society, Los Angeles, CA, USA, 19 March, 1998.
- Doping dependence of superconducting parameters in $\text{HgBa}_2\text{CuO}_{4+\delta}$ single crystals
J. Hofer, J. Karpinski, Guo-meng Zhao, M. Willemin, G.I. Meijer, E.M. Kopnin, R. Molinski, H. Schwer, C. Rossel, and H. Keller
Euroconference on Polarons: Condensation, Pairing, Magnetism, Erice, Sicily, 9-17 June, 1998.
- Angular-dependent torque magnetometry on single-crystal $\text{HgBa}_2\text{CuO}_{4+\delta}$ near the critical temperature
J. Hofer, T. Schneider, J.M. Singer, M. Willemin, H. Keller, C. Rossel, J. Karpinski, and T. Sasagawa
Swiss Physical Society Meeting, Bern, 25-26 February, 1999.
- Oxygen isotope effects in manganates and cuprates studied by EPR
A. Shengelaya, Guo-meng Zhao, K. Conder, H. Keller, and K. A. Müller
Colloquium on Magnetic Resonance in High- T_c Superconductors, Engelberg, Switzerland, January 17-21, 1999.
- Spontaneous magnetization and antiferromagnetic correlations of the CuO_2 chains in $\text{Sr}_{0.73}\text{CuO}_2$
A. Shengelaya, G.I. Meijer, J. Karpinski, Guo-meng Zhao, H. Schwer, E.M. Kopnin, C. Rossel, and H. Keller
Swiss Physical Society Meeting, Bern, 25-26 February, 1999.

Invited Lectures

- H. Keller
Seminar
University of Geneva, Switzerland, 5 May, 1998
“Probing high-temperature superconductivity with positive muons”
- H. Keller
Seminar
University of Belgrade, Belgrade, Serbia, 3 September, 1998
“Probing vortex matter in cuprate superconductors with positive muons”
- H. Keller
Seminar

Colloquium on Magnetic Resonance in High- T_c Superconductors, Engelberg, Switzerland, 20 January, 1998

“Probing vortex matter in cuprate superconductors with positive muons”

- C.M. Aegerter
Invited oral poster presentation
NATO Advanced Study Institute on Muon Science, St. Andrews, Scotland, 29 August, 1998
“Investigating low κ superconductors with μ SR and SANS”
- C.M. Aegerter
Invited talk
Complex systems seminar, University of California San Diego, USA, 1 October, 1998
“Magnetic flux structures in superconductors with low Ginzburg-Landau parameter κ ”
- C.M. Aegerter
Promotionsvortrag, Universität Zürich, Switzerland, 21 October, 1998
“Myonen und Neutronen in Supraleitern”
- A. Schilling
Seminar
Physikalisches Kolloquium, ETH Zürich and Universität Zürich, Zürich, Switzerland, 27 May, 1998
“Phasenübergänge in Vortexmaterie: Ein unerforschtes Feld für experimentelle Thermodynamik”
- A. Schilling
Invited talk
17th General Conference of the Condensed Matter Division, European Physical Society, Grenoble, France, 25 August, 1998
“The melting transition of the vortex lattice in cuprates”
- A. Shengelaya
Invited talk
The Second Polish-US Conference on High Temperature Superconductivity, Wroclaw, Poland, 17-21 August, 1998
“Oxygen isotope effects in manganates and cuprates studied by EPR”
- A. Shengelaya
Invited talk
Department of Physics, University of Augsburg, Augsburg, Germany, December 1998
“Spontaneous magnetization and antiferromagnetic correlations of the CuO_2 chains in $\text{Sr}_{0.73}\text{CuO}_2$ ”
- A. Shengelaya
Invited talk
High Magnetic Field Laboratory, Grenoble, France, December 1998
“EPR study of oxygen isotope effect in CMR manganates”
- M. Willemin
Invited talk
Commissariat à l’Energie Atomique (CEA), Grenoble, France, 19-20 November, 1998
“Ultrasensitive torque magnetometry on high- T_c superconductors”

- M. Willemin
Promotionsvortrag, Universität Zürich, Switzerland, 28 January, 1999
“Hochempfindliche Drehmoment-Magnetometrie an Hochtemperatur-Supraleitern”
- Guo-meng Zhao
Invited talk
Polarons: Condensation, Pairing, Magnetism, Erice, Sicily, Italy, 9-17 June, 1998
“Polaronic charge carriers and their condensation in the cuprate superconductors”
- Guo-meng Zhao
Invited talk
Physics of Manganites Workshop, Michigan State University, USA, 26-29 July, 1998
“Oxygen isotope effects in manganites: Evidence for (bi)polaronic charge carriers”

16.5 Research group of Prof. W. Kündig

Articles

- Gravitational constant measured by means of a beam balance
J. Schurr, F. Nolting, and W. Kündig
Phys. Rev. Lett. **80**, 1142, (1998)
- A β -spectrometer for searching effects of finite neutrino masses
E. Holzschuh, W. Kündig, L. Palermo, H. Stüssi, and P. Wenk
Nucl. Inst. Meth. A **423**, 52 (1999).
- Measurement of the gravitational constant G by means of a beam balance
J. Schurr, F. Nolting, and W. Kündig
Phys. Lett. A **248**, 295 (1998)
- Preparation of a ^{35}S -source for β -spectroscopy
L. Palermo, E. Holzschuh, W. Kündig, P. Wenk, and R. Alberto
Nucl. Inst. Meth. A **423**, 337 (1999)

Articles in press

- Search for heavy neutrinos in the β -spectrum of ^{63}Ni
E. Holzschuh, W. Kündig, L. Palermo, H. Stüssi, and P. Wenk
Phys. Lett. B.
- Direct Measurements of the Neutrino Masses
E. Holzschuh
In Neutrino physics, 2nd edition, ed. K. Winter, Cambridge University Press.
- Determination of the gravitational constant by means of a beam balance
F. Nolting, St. Schlamming, J. Schurr, and W. Kündig
Europhysics News.
- Die Gravitationskonstante – Eine Herausforderung für die Messtechnik
F. Nolting, St. Schlamming, J. Schurr und W. Kündig
Physikalische Blätter.

Conference reports

- Determination of G by means of a beam balance
F. Nolting, J. Schurr, and W. Kündig
Proceedings of the CPEM98, July 1998, Washington DC, IEEE Trans. Instrum. Meas.
- Value for G from beam-balance experiments
F. Nolting, J. Schurr, St. Schlamminger, and W. Kündig
Proceedings of the Cavendish meeting, Nov. 1998, London, Measurement science and technology.

Invited Lectures

- Value for G from beam-balance experiments
Presented by F. Nolting
The gravitational constant: Theory and experiment 200 years after Cavendish, London, Nov. 1998.

16.6 Research group of Prof. P. F. Meier

Articles

- J. M. Singer, T. Schneider, M. H. Pedersen,
On the Phase Diagram of the Attractive Hubbard Model:
Crossover and Quantum Critical Phenomena
Eur. Phys. J. B **2**, 17 (1998).
- J. M. Singer and P. F. Meier,
Knight shift in the attractive Hubbard model: crossover regime.
Physica C **302**, 183 (1998).
- P. Hüsler, E. P. Stoll, H. U. Suter, and P. F. Meier,
First-Principles Calculation of Electric-Field Gradients at the Cu Sites in $\text{YBa}_2\text{Cu}_3\text{O}_7$,
Physica C, **294**, 217 – 224 (1998).
- T. Schneider, J. Hofer, M. Willemin, J. M. Singer and H. Keller,
Universal scaling properties of extreme type-II superconductors in magnetic fields.
Eur. Phys. J. B **3**, 413 (1998).
- J. Schneider, I. Morgenstern and J. M. Singer,
Bouncing towards the optimum: Improving results of Monte Carlo optimization algorithms.
Phys. Rev. E **58**, 5085 (1998).
- P. Hüsler, S. Schafroth, E. Stoll, H.U. Suter, and P.F. Meier,
A User Project: First-Principles Calculation of Electric-Field Gradients at the Cu Sites
in the High Temperature Superconductor $\text{YBa}_2\text{Cu}_3\text{O}_7$,
CrossCutS, **7**(2), 15 (1998).
- J. M. Singer, T. Schneider and P. F. Meier,
Spectral properties of the attractive Hubbard model.
Eur. Phys. J. B **7**, 37 (1999).

- J. M. Singer, T. Schneider and P. F. Meier,
Quantum Monte Carlo Simulations of the Two-Dimensional Attractive Hubbard Model:
Phase Diagram and Spectral Properties.
IN: M. Ausloos et al., Symmetry and Pairing in Superconductors,
Kluwer Academic Publ., Netherlands (1999).
- T. Schneider and J. M. Singer,
Fundamental constraints for the mechanism of superconductivity in cuprates.
Eur. Phys. J. B **7**, 517 (1999).

Articles in press

- H. U. Suter, P. Hüsler, E. P. Stoll, S. Schafroth and P. F. Meier,
Cluster Calculations of the Hyperfine Properties of Copper Compounds,
Hyperfine Interactions.
- J. Schneider, M. Schmid, I. Morgenstern and J. M. Singer,
Ensemble Based Search Space Smoothing.
Comp. Optimization and Appl. 1999.
- T. Schneider and J. M. Singer,
Magnetic Field induced Dimensional Crossover Phenomena in Cuprate Superconductors
and their Implications.
Physica C 1999.
- J. Hofer, T. Schneider, J. M. Singer, M. Willemin, C. Rossel, H. Keller and J. Karpinski,
Angular-dependent torque magnetometry on single-crystal $\text{HgBa}_2\text{CuO}_{4+y}$ near the critical
temperature.
Phys. Rev. B 1999.
- T. Schneider and J. M. Singer,
Magnetic field induced phase transitions in $\text{YBa}_2\text{Cu}_4\text{O}_8$.
Eur. Phys. J. B 1999.
- H. R. Moser, B. Weber, H. G. Wieser, and P. F. Meier,
Electroencephalograms in epilepsy: analysis and seizure prediction within the frame of
Lyapunov theory.
Physica D.

Invited Lectures

- J. M. Singer
Theoretical Physics Colloquium, University of Geneva.
- J. M. Singer
Colloquium at the Institut Romand de Recherche Numérique en Physique des Matériaux
(IRRMA), Ecole Polytechnique Fédérale Lausanne.
- J. M. Singer
Nato ASI Conference on 'Symmetry and Pairing in High- T_c Superconductors', Yalta,
Crimea (Ukraine).

- J. M. Singer
Seminar in Festkörperphysik, Universität Zürich.
- P. F. Meier
Calculations of the hyperfine properties of copper compounds
Internat. Conference on Hyperfine Interactions, Durban, ZA, 27. 8. 1998
- P. F. Meier
Cluster calculations of the electronic structure of the La_2CuO_4 system
Colloquium on Magnetic Resonance in High- T_c Superconductors, Engelberg, 19. 1. 1999
- P. F. Meier
Examples of collaborations between computational physics, computer science and medicine
Tagung der Schweiz. Physik. Ges., Bern, 25. 2. 1999
- P. F. Meier
Electroencephalograms in epilepsy: analysis and seizure prediction within the frame of nonlinear dynamics
Internat. Workshop on 'Chaos in Brain ?', Bonn, 11. 3. 1999

16.7 Research group of Prof. J. Osterwalder

Articles

- High-resolution photoemission study of hcp-Co(0001)
E. Wetli, T. J. Kreutz, H. Schmid, T. Greber, J. Osterwalder, M. Hochstrasser
Surf. Sci. 402-404 (1998) 551
- Angle-scanned photoemission: Fermi surface mapping and structural determination
P. Aebi, R. Fasel, D. Naumovic, J. Hayoz, Th. Pillo, M. Bovet, R. G. Agostino, L. Patthey, L. Schlapbach, F. P. Gil, H. Berger, T. J. Kreutz, J. Osterwalder
Surf. Sci. 402-404 (1998) 614
- Crystalline structure of surface layers for Ag/Cu(001) studied by incident beam electron diffraction
M. Nowicki, J. Osterwalder
Surf. Sci. 408 (1998) 165
- Semiconductor-metal transition of the single-domain K/Si(001)-(2x1) interface
J. A. Martin-Gago, M. C. Asensio, P. Aebi, R. Fasel, D. Naumovic, J. Osterwalder
M. C. Refolio, J. M. Lopez-Sancho, J. Rubio
Phys. Rev. B 57 (1998) 9201
- Complete k-space mappings of cuprates at different doping levels
P. Schwaller, T. Greber, H. Berger, J. Osterwalder
J. Phys. Chem. Solids 59 (1998) 1929
- Temperature-dependent electronic structure of nickel metal
T. J. Kreutz, T. Greber, P. Aebi, J. Osterwalder
Phys. Rev. B 58 (1998) 1300
- Direct observation of subsurface oxygen on Rh(111)
J. Wider, T. Greber, E. Wetli, T. J. Kreutz, P. Schwaller, J. Osterwalder
Surf. Sci. 417 (1998) 301

- X-ray photoelectron diffraction in the backscattering geometry: a key to adsorption sites and bond lengths at surfaces
T. Greber, J. Wider, E. Wetli, J. Osterwalder
Phys. Rev. Lett. 81 (1998) 1654
- The role of molecular state and orientation in harpooning reactions: N_2O on Cs/Pt(111)
M. Brandt, T. Greber, N. Böwering, U. Heinzmann
Phys. Rev. Lett. 81 (1998) 2376
- State and orientation dependent N_2 emission in the N_2O +Cs reaction
M. Brandt, T. Greber, F. Kuhlmann, N. Böwering, U. Heinzmann
Surf. Sci. 402-404 (1998) 160
- Probing harpooning and dissociation in gas surface reactions by exoemission
T. Greber Appl. Phys. A 67 (1998) 701
- Copper electrodeposition onto alkanethiolate layers
O. Cavalleri, A. M. Bittner, H. Kind, K. Kern, T. Greber
Z. Phys. Chem. 59 (1998) 1929
- Electroless deposition of metal nanoislands on aminothioliolate-functionalized Au(111) electrodes
H. Kind, A. M. Bittner, O. Cavalleri, K. Kern, T. Greber
J. Phys. Chem. B 102 (1998) 7582
- Nonadiabatic gas surface reactions
T. Greber
Current Opinion in Solid State and Materials Science 3 (1998) 446

Articles in press

- Controlled underdoping of cuprates using ultraviolet radiation
P. Schwaller, S. Berner, T. Greber, J. Osterwalder
Appl. Phys. Lett. (1999)
- Correlation effects in the low-energy region of nickel photoemission spectra
F. Manghi, V. Bellini, J. Osterwalder, T. J. Kreutz, P. Aebi, C. Arcangeli
Phys. Rev. B (Rapid Communication) (1999)
- XPD and STM investigation of hexagonal boron nitride on Ni(111)
W. Auwärter, T. J. Kreutz, T. Greber, J. Osterwalder
Surf. Sci. (1999)

Diploma and PhD Theses

- Auswirkungen der Schichtstruktur von a-C:H Multilagen auf ihr tribologisches Verhalten
Lukas J. C. Knoblauch-Meyer
Dissertation, Physik-Institut, Universität Zürich, 1999
- Untersuchung optischer und thermischer Eigenschaften einer dünnen Natriumdampfzelle
Arno Schneider
Diploma Thesis, Physik-Institut, Universität Zürich, 1998
- Photoemission from oriented orbitals
Moritz Hoesch
Diploma Thesis, Physik-Institut, Universität Zürich, 1998

- Surface states on vicinal Cu(111)
Felix Baumberger
Diploma Thesis, Physik-Institut, Universität Zürich, 1998
- Unterdotieren von Kuprat-Supraleitern mittels ultraviolettem Licht
Simon Berner
Diploma Thesis, Physik-Institut, Universität Zürich, 1998
- Untersuchungen an hexagonalem Bornitrid-Filmen auf Nickel
mittels Rastertunnelmikroskopie und Photoemission
Willi Auwärter
Diploma Thesis, Physik-Institut, Universität Zürich, 1998

Conference reports

- Near node photoelectron holography
J. Wider
Summer school, Luso, Portugal, 13.5.98
- Spatio-temporal modifications to shape, intensity, polarization
and propagation of single pass laser beams in sodium vapor
due to optical pumping
R. Holzner, S. Dangel
Conference on Patterns in Nonlinear Optical Systems, Pueblo Acanitlido,
Alicante, Spain, May 21-23, 1998
- Nonlinear effects due to optical pumping of sodium vapor
by single-pass laser beams
R. Holzner, S. Dangel
Conference "Nonlinear Optics '98",
Princeville, Kauai, Hawaii, August 10-14, 1998
- Optical pumping induced spatio-temporal modifications
to single pass laser beams in sodium vapor
R. Holzner, S. Dangel
European Conference on Lasers and Electro-Optics / European Quantum
Electronics Conference "CLEO / EUROPE-EQEC 98",
Glasgow, Scotland, September 13-18, 1998
- XPD characterization of hexagonal boron nitride on Ni(111)
T. Greber, W. Auwärter, T. J. Kreuz, J. Osterwalder
International Vacuum Congress 14, Birmingham, U.K., 3.9.98
- Localization of Shockley surface states on vicinal Cu(111)
F. Baumberger, T. Greber, J. Osterwalder
Jahrestagung der Schweiz. Physik. Gesellschaft, Bern, 25.-26. Februar 1999
- Temperature information from Fermi-edges
J. Kröger, T. Greber, T. J. Kreuz, J. Osterwalder
Jahrestagung der Schweiz. Physik. Gesellschaft, Bern, 25.-26. Februar 1999

Invited Lectures

- T. Greber
Exoemission: Sonde für die Aufklärung heisser Gas-Oberflächenreaktionen
Hauptvortrag, DPG-Tagung Regensburg, 24.3.98

- J. Osterwalder
A new surface science beamline at ELETTRA
Workshop on New Directions at the Advanced Light Source, Berkeley, CA, 24.3.98
- T. Greber
Photoelectron diffraction and Fermi surface mapping
International School on the Application of Surface Science Techniques,
Erice, Italy, 6.4.98
- R. Holzner
Natriumatome im Licht
Laser-Seminar, Institut für angewandte Physik, Universität Bern, 30.4.98
- R. Holzner
Laserstrahlen im Natriumdampf
Seminar, Physikalisch-Chemisches Institut, Universität Zürich, 7.5.98
- J. Osterwalder
Winkelaufgelöste Photoemission in Bildern: Was lernt man Neues?
Kolloquium, Fachbereich Physik, Universität Dortmund, 19.5.98
- T. Greber
Exoemission als Sonde für die Aufklärung heisser Gas-Oberflächenreaktionen
Antrittsvorlesung, Universität Zürich, 8.6.98
- J. Osterwalder
Fermi surface mapping by angular resolved photoemission
World Ceramics Congress / CIMTEC 98, Florence, Italy, 15.6.98
- T. Greber
Probing hot adatoms by exoemission
Gruppenseminar K. Kern, EPF Lausanne, 19.6.98
- J. Osterwalder
Photoemission from magnetic materials
1st International SLS Workshop on Synchrotron Radiation
Monte Verita, Ascona, 2.8.98
- J. Osterwalder
High-resolution k-space imaging near the Fermi surface of 3d ferromagnets
12th International Conference on Vacuum Ultraviolet Radiation Physics
San Francisco, CA, 6.8.98
- T. Greber
Nonadiabatic gas-surface reactions - What can we learn from exoemission?
The reaction of O_2 and N_2O with alkali metals
Seminar, LCAM, Orsay, France, 14.10.98
- M. Hoesch
Photoemission from oriented orbitals: angular distribution of
photoelectrons from CO on Ni(111)
Gruppenseminar, SLS Gruppe, PSI Villigen, 1.2.98

16.8 Research group of Prof. P. Truöl

Articles

1. A Measurement of the Gluon Density in the Proton Based on Charm Production at HERA

- David Müller
Thesis Universität Zürich (1998)
2. Photoproduction of open charm in ep-collisions at HERA
Martin zur Nedden
Thesis Universität Zürich (1998)
 3. Photoproduction of $\Psi(2s)$ Mesons at HERA
H1-Collaboration**, C. Adloff et al.
DESY 97 – 228
Physics Letters **B421** (1998), 385 - 395
 4. Hadron Production in Diffractive Deep-Inelastic Scattering
H1-Collaboration**, C. Adloff et al.
DESY 98 – 029
Physics Letters **B428** (1998), 206 - 220
 5. Multiplicity Structure of the Hadronic Final State in Diffractive Deep-Inelastic Scattering at HERA
H1-Collaboration**, C. Adloff et al.
DESY 98 – 044
The European Physical Journal **C5** (1998), 439 - 452
 6. Observation of Events with an Isolated High Energy Lepton and Missing Transverse Momentum at HERA
H1-Collaboration**, C. Adloff et al.
DESY 98 – 063
The European Physical Journal **C5** (1998), 575 - 584
 7. Differential (2+1) Jet Rates and Determination of α_s in Deep-Inelastic Scattering at HERA
H1-Collaboration**, C. Adloff et al.
DESY 98 – 075
The European Physical Journal **C5** (1998), 625 - 639
 8. Diffractive Dijet Photoproduction at HERA
H1-Collaboration**, C. Adloff et al.
DESY 98 – 092
The European Physical Journal **C6** (1999), 421 - 436
 9. Forward Jet and Particle Production at HERA
H1-Collaboration**, C. Adloff et al.
DESY 98 – 143
Nuclear Physics **B538** (1999), 2 - 22.
 10. Multi-Jet Event Rates in Deep-Inelastic Scattering and Determination of the Strong Coupling Constant
H1-Collaboration**, C. Adloff et al.
DESY 98 – 087
The European Physical Journal **C6** (1999), 575 - 585
 11. Measurement of Leading Proton and Neutron Production in Deep Inelastic Scattering at HERA

H1-Collaboration**, C. Adloff et al.
DESY 98 – 169
The European Physical Journal **C6** (1999), 587 - 602

Articles in Print

1. Di-jet Rates in Deep-Inelastic Scattering at HERA
H1-Collaboration**, C. Adloff et al.
DESY 98 – 076
submitted to The European Physical Journal **C** (1998)
2. Charged Particle Cross Sections in Photoproduction and Extraction of the Gluon Density in the Photon
H1-Collaboration**, C. Adloff et al.
DESY 98 – 148
submitted to The European Physical Journal **C** (1998)
3. Measurement of D^* Meson Cross Sections at HERA and Determination of the Gluon Density in the Proton
H1-Collaboration**, C. Adloff et al.
DESY 98 – 204
submitted to Nuclear Physics **B** (1998)
4. Measurement of Dijet Cross Sections in Low Q^2 and the Extraction of an Effective Parton Density for the Virtual Photon
H1-Collaboration**, C. Adloff et al.
DESY 98 – 205
submitted to The European Physical Journal **C** (1998)
5. Measurement of Internal Jet Structure in Di-jet Production in Deep Inelastic Scattering at HERA
H1-Collaboration**, C. Adloff et al.
DESY 98 – 210
submitted to Nuclear Physics **B** (1998)
6. Elastic Electroproduction of ρ Mesons at HERA
H1-Collaboration**, C. Adloff et al.
DESY 99 – 10
submitted to The European Physical Journal **C** (1999)
7. Charmonium Production in Deep Inelastic Scattering at HERA
H1-Collaboration**, C. Adloff et al.
DESY 99 – 026
submitted to The European Physical Journal **C**
8. Extraction of the Gluon Density from Open Charm at H1
D. Müller
Proc. 6th Int. Workshop on Deep-Inelastic Scattering and QCD (DIS98), IHE, Brussels, Belgium (April 1998)
9. Study of $K^+ \rightarrow \pi^+ e^+ e^-$ and $K^+ \rightarrow \pi^+ \mu^+ \mu^-$ Decays in E865 at the AGS
E-865-collaboration[†], H. Ma et al.

presented by H. Ma

Proc. 29th Int. Conf. on High-Energy Physics, Vancouver, Canada (July 98)

10. Recent Results from BNL E865

E865-collaboration [†], A. Sher et al.

presented by A. Sher

Proc. Workshop on Heavy Quarks at Fixed Targets, Chicago, USA (October 98)

Talks

1. Extraction of the Gluon Density from Open Charm at H1

D. Müller

5. 4. 1998

DIS98, 6th Int. Workshop on Deep-Inelastic Scattering and QCD, April 1998, IHE, Brussels, Belgium

2. F_{2C} and $xG(x)$ from Charm Production

M. zur Nedden

4. 6. 1998

5th Workshop on Low x Physics at HERA, Juni 1998, DESY-Zeuthen, Berlin-Zeuthen, Germany

3. Status of H1

F. Sefkow

8. 7. 1998

Physics Research Committee, DESY, Hamburg, Germany

4. Zerfälle von K-Mesonen: Ein altes Thema und eine bleibende Herausforderung für die experimentelle Teilchenphysik

P. Truöl

30. 1. 1999

Zürcher Physikalische Gesellschaft, Zürich

5. Diffraktive Charm-Produktion bei HERA

S. Hengstmann

19. 3. 1999

DPG Frühjahrstagung 1999 - Teilchenphysik, Heidelberg, Germany

[†] E865-collaboration:

R. Appel^{8,6}, G.S. Atoyan^{2,8}, B. Bassaleck⁵, D.N. Brown⁶, D.R. Bergman⁸, N. Cheung⁶, S. Dhawan⁸, H. Do⁸, J. Egger³, S. Eilerts⁵, C. Felder^{1,6}, H. Fischer⁵, M. Gach⁶, W.D. Herold³, V.V. Isakov^{2,8}, H. Kaspar³, D. Kraus⁶, D. Lazarus¹, L. Leipuner¹, J. Lowe⁵, J. Lozano⁸, H. Ma¹, W. Majid⁸, W. Menzel⁴, S. Pislak^{7,8}, A.A. Poblaguev^{2,8}, A.L. Proskurjakow², P. Rehak¹, P. Robmann⁷, A. Sher⁶, R. Stotzer⁵, J.A. Thompson⁶, P. Truöl^{7,8}, H. Weyer^{4,3}, M.E. Zeller⁸

³ Paul Scherrer Institut, Villigen

⁷ Physik-Institut der Universität Zürich, Zürich

** H1-collaboration (status of March 1999, the actual author list may differ from paper to paper somewhat):

C. Adloff³³, V. Andreev²⁴, B. Andrieu²⁷, V. Arkadov³⁴, A. Astvatsatourov³⁴, I. Ayyaz²⁸, A. Babaev²³, J. Bähr³⁴, P. Baranov²⁴, E. Barrelet²⁸, W. Bartel¹⁰, U. Bassler²⁸, P. Bate²¹, A. Beglarian^{10,39}, O. Behnke¹⁰, H.-J. Behrend¹⁰, C. Beier¹⁴, A. Belousov²⁴, T. Benisch¹⁰, Ch. Berger¹, G. Bernardi²⁸, T. Berndt¹⁴, G. Bertrand-Coremans⁴, P. Biddulph²¹, J.C. Bizot²⁶, V. Boudry²⁷, W. Braunschweig¹, V. Brisson²⁶, H.-B. Bröker², D.P. Brown²¹, W. Brückner¹², P. Bruel²⁷, D. Bruncko¹⁶, J. Bürger¹⁰, F.W. Büsser¹¹, A. Bunyatyan^{12,39}, S. Burke¹⁷, A. Burrage¹⁸, G. Buschhorn²⁵, D. Calvet²², A.J. Campbell¹⁰, T. Carli²⁵, E. Chabert²², M. Charlet⁴, D. Clarke⁵, B. Clerbaux⁴, C. Collard⁴, J.A. Coughlan⁵, M.-C. Cousinou²², B.E. Cox²¹, G. Cozzika⁹, J. Cvach²⁹, J.B. Dainton¹⁸, W.D. Dau¹⁵, K. Daum^{33,38}, M. David^{9,†}, M. Davidsson²⁰, A. De Roeck¹⁰, E.A. De Wolf⁴, B. Delcourt²⁶, R. Demirchyan^{10,39}, C. Diaconu²², M. Dirkmann⁷, P. Dixon¹⁹, V. Dodonov¹², K.T. Donovan¹⁹, J.D. Dowell³, A. Droutskoi²³, J. Ebert³³, G. Eckerlin¹⁰, D. Eckstein³⁴, V. Efremenko²³, S. Egli³⁶, R. Eichler³⁵, F. Eisele¹³, E. Eisenhandler¹⁹, E. Elsen¹⁰, M. Enzenberger²⁵, M. Erdmann^{13,40,f}, A.B. Fahr¹¹, P.J.W. Faulkner³, L. Favart⁴, A. Fedotov²³, R. Felst¹⁰, J. Feltesse⁹, J. Ferencei¹⁰, F. Ferrarotto³¹, S. Ferron²⁷, M. Fleischer¹⁰, G. Flügge², A. Fomenko²⁴, J. Formánek³⁰, J.M. Foster²¹, G. Franke¹⁰, E. Gabathuler¹⁸, K. Gabathuler³², F. Gaede²⁵, J. Garvey³, J. Gassner³², J. Gayler¹⁰, R. Gerhards¹⁰, S. Ghazaryan^{10,39}, A. Glazov³⁴, L. Goerlich⁶, N. Gogitidze²⁴, M. Goldberg²⁸, I. Gorelov²³, C. Grab³⁵, H. Grässler², T. Greenshaw¹⁸, R.K. Griffiths¹⁹, G. Grindhammer²⁵, T. Hadig¹, D. Haidt¹⁰, L. Hajduk⁶, M. Hampel¹, V. Hausteina³³, W.J. Haynes⁵, B. Heinemann¹⁰, G. Heinzelmanna¹¹, R.C.W. Henderson¹⁷, S. Hengstmann³⁶, H. Henschel³⁴, R. Heremans⁴, G. Herrera^{7,41,l}, I. Herynek²⁹, M. Hilgers³⁵, K.H. Hiller³⁴, C.D. Hilton²¹, J. Hladký²⁹, P. Höting², D. Hoffmann¹⁰, R. Horisberger³², S. Hurling¹⁰, M. Ibbotson²¹, Ç. İşsever⁷, M. Jacquet²⁶, M. Jaffre²⁶, L. Janauschek²⁵, D.M. Jansen¹², X. Janssens⁴, L. Jönsson²⁰, D.P. Johnson⁴, M. Jones¹⁸, H. Jung²⁰, H.K. Kästli³⁵, M. Kander¹⁰, D. Kant¹⁹, M. Kapichine⁸, M. Karlsson²⁰, O. Karschnick¹¹, O. Kaufmann¹³, M. Kausch¹⁰, F. Keil¹⁴, N. Keller¹³, I.R. Kenyon³, S. Kermiche²², C. Kiesling²⁵, M. Klein³⁴, C. Kleinwort¹⁰, G. Knies¹⁰, H. Kolanoski³⁷, S.D. Kolya²¹, V. Korbel¹⁰, P. Kostka³⁴, S.K. Kotelnikov²⁴, T. Krämerkämper⁷, M.W. Krasny²⁸, H. Krehbiel¹⁰, J. Kroseberg³⁶, D. Krücker³⁷, K. Krüger¹⁰, A. Küpper³³, H. Küster², T. Kurča³⁴, W. Lachnit¹⁰, R. Lahmann¹⁰, D. Lamb³, M.P.J. Landon¹⁹, W. Lange³⁴, U. Langenegger³⁵, A. Lebedev²⁴, F. Lehner¹⁰, V. Lemaître¹⁰, R. Lemrani¹⁰, V. Lendermann⁷, S. Levonian¹⁰, M. Lindstroem²⁰, G. Lobo²⁶, V. Lubimov²³, S. Lüders³⁵, D. Lüke^{7,10}, L. Lytkin¹², N. Magnussen³³, H. Mahlke-Krüger¹⁰, N. Malden²¹, E. Malinovski²⁴, I. Malinovski²⁴, R. Maraček²⁵, P. Marage⁴, J. Marks¹³, R. Marshall²¹, H.-U. Martyn¹, J. Martyniak⁶, S.J. Maxfield¹⁸, T.R. McMahon¹⁸, A. Mehta⁵, K. Meier¹⁴, P. Merkel¹⁰, F. Metlica¹², A. Meyer¹⁰, H. Meyer³³, J. Meyer¹⁰, P.-O. Meyer², S. Mikocki⁶, D. Milstead¹⁰, R. Mohr²⁵, S. Mohrdieck¹¹, M.N. Mondragon⁷, F. Moreau²⁷, A. Morozov⁸, J.V. Morris⁵, D. Müller³⁶, K. Müller¹³, P. Murín^{16,42}, V. Nagovizin²³, B. Naroska¹¹, J. Naumann⁷, Th. Naumann³⁴, I. Négri²², P.R. Newman³, H.K. Nguyen²⁸, T.C. Nicholls¹⁰, F. Niebergall¹¹, C. Niebuhr¹⁰, Ch. Niedzballa¹, H. Niggli³⁵, O. Nix¹⁴, G. Nowak⁶, T. Nunnemann¹², J.E. Olsson¹⁰, D. Ozerov²³, P. Palmen², V. Panassik⁸, C. Pascaud²⁶, S. Passaggio³⁵, G.D. Patel¹⁸, H. Pawletta², E. Perez⁹, J.P. Phillips¹⁸, A. Pieuchot¹⁰, D. Pitzl³⁵, R. Pöschl⁷, I. Potashnikova¹², B. Povh¹², K. Rabbertz¹, G. Rädela⁹, J. Rauschenberger¹¹, P. Reimer²⁹, B. Reiser²⁵, D. Reyna¹⁰, S. Riess¹¹, E. Rizvi³, P. Robmann³⁶, R. Roosen⁴, A. Rostovtsev^{23,10}, C. Royon⁹, S. Rusakov²⁴, K. Rybicki⁶, D.P.C. Sankey⁵, J. Scheins¹, F.-P. Schilling¹³, S. Schleich¹⁴, P. Schleper¹³, D. Schmidt³³, D. Schmidt¹⁰, L. Schoeffel⁹, T. Schörner²⁵, V. Schröder¹⁰, H.-C. Schultz-Coulon¹⁰, F. Sefkow³⁶, V. Shekelyan²⁵, I. Sheviakov²⁴, L.N. Shtarkov²⁴, G. Siegmon¹⁵, Y. Sirois²⁷, T. Sloan¹⁷, P. Smirnov²⁴, M. Smith¹⁸, V. Solochenko²³,

Y. Soloviev²⁴, V. Spaskov⁸, A. Specka²⁷, H. Spitzer¹¹, F. Squinabol²⁶, R. Stamen⁷,
J. Steinhart¹¹, B. Stella³¹, A. Stellberger¹⁴, J. Stiewe¹⁴, U. Straumann¹³, W. Struczinski²,
J.P. Sutton³, M. Swart¹⁴, M. Taševský²⁹, V. Tchernyshov²³, S. Tchetchelnitski²³,
G. Thompson¹⁹, P.D. Thompson³, N. Tobien¹⁰, R. Todenhagen¹², D. Traynor¹⁹, P. Truöl³⁶,
G. Tsipolitis³⁵, J. Turnau⁶, E. Tzamariudaki²⁵, S. Udluft²⁵, A. Usik²⁴, S. Valkár³⁰,
A. Valkárová³⁰, C. Vallée²², A. Van Haecke⁹, P. Van Mechelen⁴, Y. Vazdik²⁴, G. Villet⁹,
K. Wacker⁷, R. Wallny¹³, T. Walter³⁶, B. Waugh²¹, G. Weber¹¹, M. Weber¹⁴, D. Wegener⁷,
A. Wegner¹¹, T. Wengler¹³, M. Werner¹³, L.R. West³, G. White¹⁷, S. Wiesand³³,
T. Wilksen¹⁰, M. Winde³⁴, G.-G. Winter¹⁰, Ch. Wissing⁷, C. Wittek¹¹, M. Wobisch²,
H. Wollatz¹⁰, E. Wünsch¹⁰, J. Žáček³⁰, J. Zálešák³⁰, Z. Zhang²⁶, A. Zhokin²³, P. Zini²⁸,
F. Zomer²⁶, J. Zsembery⁹ and M. zur Nedden¹⁰

³² Paul Scherrer Institut, Villigen

³⁵ Institut für Teilchenphysik, ETH, Zürich

³⁶ Physik-Institut der Universität Zürich, Zürich